Realia et naturalia

DISSERTATIONES
CHIMICAE
UNIVERSITATIS
TARTUENSIS
133

VITALI GROZOVSKI

Adsorption of organic molecules at single crystal electrodes studied by *in situ* STM method

DISSERTATIONES CHIMICAE UNIVERSITATIS TARTUENSIS

133

DISSERTATIONES CHIMICAE UNIVERSITATIS TARTUENSIS
133

VITALI GROZOVSKI

Adsorption of organic molecules at single crystal electrodes studied by *in situ* STM method

UNIVERSITY OF TARTU
PRESS
1632

Institute of Chemistry, Faculty of Science and Technology, University of Tartu, Estonia

Dissertation is accepted for the commencement of the degree of Doctor of Philosophy in Chemistry on December 19, 2013 by the Council of Institute of Chemistry, University of Tartu.

Supervisors: Prof. Enn Lust
University of Tartu, Estonia

PhD Silvar Kallip
University of Tartu, Estonia

Opponent: Prof. Antonio Rodes
University of Alicante, Spain

Commencement: 30.01.2014, at 10:00. Auditorium 1021, Ravila 14a, Tartu

Publication of this dissertation is granted by University of Tartu, Estonia.

ISSN 1406–0299
ISBN 978–9949–32–477–4 (print)
ISBN 978–9949–32–478–1 (pdf)

University of Tartu Press
www.tyk.ee

CONTENTS

1. LIST OF ORIGINAL PUBLICATIONS

I **V. Grozovski**, S. Kallip E. Lust, *In situ* STM studies of Sb(111) electrodes in aqueous electrolyte solutions, Surf. Sci 613, 108–113 (2013).

II **V. Grozovski**, H. Kasuk, S. Kallip, E. Lust, Adsorption of thiourea on Bi(111) electrode surface, J. Electroanal. Chem. 712, 103–112 (2014)

III **V. Grozovski**, V. Ivaništšev, H. Kasuk, T. Romann, E. Lust, Balance of the interfacial interactions of 4,4'-bipyridine at Bi(111) surface, Electrochim. Acta *accepted* (2013)

Author's contribution:

Paper I: Performed all electrochemical and surface measurements, analysis of data and participated in manuscript preparation.

Paper II: Performed all experimental surface measurements and data analysis. Collaborated in theoretical data interpretation and participated in manuscript preparation.

Paper III: Performed all experimental surface measurements and data analysis. Participated in all electrochemical measurements and data analysis. Collaborated in manuscript preparation.

2. ABBREVIATIONS AND SYMBOLS

2D	two dimensional
3D	three dimensional
2,2'-BP	2,2'-bipyridine
4,4'-BP	4,4'-bipyridine
4,4'-BPH_2^+	protonated 4,4'-bipyridine radical-cations
(Par)	adsorbed 4,4'-BP molecule in parallel orientation at Bi(111) surface
(Per)	adsorbed 4,4'-BP molecule in perpendicular orientation at Bi(111) surface
A	absorbance
ac	alternative current
AFM	atomic force microscopy
ASE	atomistic simulation environment
ATR	attenuated total reflection
ATR-SEIRAS	attenuated total reflection surface enhanced infrared absorption spectroscopy
B3LYP	hybrid generalized gradient approximation functional
$Bi(111)^C$	Bi(111) single crystal electrode cleaved at the temperature of liquid nitrogen
$Bi(111)^{EP}$	electrochemically polished Bi(111) single crystal electrode
C(N)	adsorbed 4,4'-BP molecule oriented with its N-atom pointed towards Bi(111) surface
CAM-B3LYP	hybrid exchange-correlation functional
C	differential capacitance
C_0	differential capacitance as $f \rightarrow 0$
C_{ad}	adsorption capacitance
C_{dl}	double layer capacitance
C_p	parallel interfacial capacitance
C_S	series differential capacitance
C_{true}	interfacial capacitance as ac frequency $f \rightarrow \infty$
$c_{4,4'\text{-BP}}$	concentration of 4,4'-bipyridine
c_{TU}	concentration of thiourea
CE	counter electrode
CV	cyclic voltammetry
D	effective diffusion coefficient
d	tip-substrate separation
DDEC	density derived electrostatic and chemical charge
d_{dl}	effective thickness of the double layer
DFT	density functional theory
E	electrode potential
e	elementary charge
E(t)	electrode potential at time t

E_0	reference potential
E_A	potential amplitude
E_{bias}	STM tip bias voltage
EC	equivalent circuit
E_N	limiting adsorption potential shift
$E_{q=0}$	potential of zero charge
E_S	substrate potential
E_T	STM tip potential
f	frequency in Hz
FFT	fast Fourier transform
FT	Fourier transform
G	tunneling conductance
G_0	tunneling conductance, associated with quantum-point contact at which the barrier has collapsed
GGA	generalized gradient approximation
GPAW	grid-based projector-augmented wave method
h	Planck constant
$\hbar$	reduced Planck constant
HOMO	highest occupied molecular orbital
HOPG	highly oriented pyrolytic graphite
I	electrode current
i(t)	current at time t
i_A	current amplitude
$I_{faradic}$	faradic current at the STM tip
IFG	interferogram
IR	infrared
I_S	substrate current
I_T	tip current
I_{tunnel}	tunneling current at the STM tip
j	current density
j_i	imaginary unit ($\sqrt{-1}$)
k_1, k_2, k_3	constants characterizing the process of two-dimensional association of organic molecules
LanL2DZ	Los Alamos National Laboratory double zeta basis set
LDOS	local density of states
LSDA	local spin density approximation
LYP	Lee-Yang-Parr correlation functional
M06-L	meta-hybrid generalized gradient approximation functional
m_e	electron rest mass
PBE	functional of Perdew, Burke, and Ernzerhof
q	charge
R_0	contact resistance
R_{ct}	charge transfer resistance
RE	reference electrode

R_{el}	base electrolyte resistance
RMS	root mean square roughness
R_p	parallel resistance
R_S	series resistance
S	electrode substrate
$Sb(111)^C$	Sb(111) single crystal electrode cleaved at the temperature of liquid nitrogen
$Sb(111)^{EP}$	electrochemically polished Sb(111) single crystal electrode
SCF	self-consistent field
SECM	scanning electrochemical microscopy
SEIRAS	surface enhanced infrared reflection absorption spectroscopy
SERS	surface enhanced Raman spectroscopy
SNIFTIRS	subtractively normalized interfacial Fourier transform infrared spectroscopy
SNR	signal to noise ratio
SPM	scanning probe microscopy
STM	scanning tunneling microscopy
t	time
T	tunneling tip
T_n	the kinetic energy of a system of noninteracting electrons with the same spin densities as the real system
TRS-MCT	time-resolved mercury cadmium telluride detector
TU	thiourea
UEG	uniform electron gas
UHV	ultra high vacuum
V	bias voltage between tip and substrate
v	net rate of adsorption step due to the departure from equilibrium conditions
vdW	van der Waals
vdW-DF2	van der Waals density functional, second version
V_{ee}	interaction of real electrons with themselves
WFT	wave function theory
Z	summary impedance
Z’	real part of impedance
Z’’	imaginary part of impedance
Z_{GFW}	generalized finite length Warburg diffusion impedance
α	fractional exponent
Γ	Gibbs adsorption
Γ_m	influence of the maximal Gibbs adsorption
δ	phase angle
ΔE_{int}	interaction energy
ε^*	complex dielectric constant
$\varepsilon’$	real part of the complex dielectric constant
$\varepsilon’’$	imaginary part of the complex dielectric constant

ε_0	vacuum dielectric constant
ε_{ee}	the classical Coulomb energy of the spin densities interacting with each other and with themselves
ε_{eff}	macroscopic dielectric constant of the electrolyte and/or adsorption layer
ε_{ne}	the interaction of the electron distribution with the nuclear framework
ε_{xc}	exchange-correlation energy
θ	surface coverage
μ	chemical potential
π	Pi number
$\rho_s(z, E)$	local density of states
τ_D	diffusion controlled relaxation time constant
τ_K	relaxation time constant of the heterogeneous charge transfer process
ω_0	exchange rate of molecules in the condition of two dimensional associations
$\Delta\Gamma^0{}_A$	Gibbs adsorption energy value
Φ	phase shift
$\Psi_{j\sigma}$	Kohn-Sham spin-orbitals
φ	effective barrier height
κ	decay constant, related to the magnitude and the shape of potential barrier
ν	scanning rate
ρ	electron spin density
ω	radial frequency

3. INTRODUCTION

Adsorption process of organic compounds at the metal electrode surfaces from electrolyte solutions is very interesting with a respect to theoretical and applied electrochemistry viewpoint. Adsorption processes can be applied for the regulation of the metal deposition processes and corrosion inhibition. Many molecular systems and self-assembled monolayers adsorbed on the metal surfaces are applied for the construction of some organic functional devices such as field-effect transistors or high-density memory circuits [1]. Therefore, the detailed understanding of the binding characteristics of organic molecules on the metal surfaces and dependence of surface coverage (Gibbs adsorption) on the electrode potential is crucial for developing the modern technological molecular devices at the molecular scale [2]. Application of scanning probe microscopy along with classical electrochemical methods reveals a lot of interfacial phenomena at the submolecular and atomic level, such as adsorption/ desorption and the potential-dependent phase transitions of the organic molecules adlayers at the metal electrodes [3–6].

Scanning tunneling microscopy (STM) is an extremely useful interactive method for detailed analysis of the solid material surface structure. STM method allows obtaining the high-resolution pictures of different conductive surfaces and the adsorbed adlayers. It is possible to image the electrode surface structure *in situ* at the atomic resolution level, visualize the structure of the deposited adlayers under electrode potential dependence on the substrate chemical composition and to establish also the atomic structure of many single crystal metal electrodes [7–9]. Obviously, the structure and stability of an adsorbed monolayer strongly depends on the crystallographic structure of the single crystal plane studied, determining the adsorbate-adsorbent interaction, as well as the adsorbate-adsorbate, adsorbate-electrolyte ions, adsorbate-solvent and solvent-solvent lateral Gibbs interaction energies [3–5,10–21].

In addition to the experimental approach, the modern density functional theory (DFT) calculation methods [22–25] can provide more detailed information on strength of the interactions inside the system that governs the adsorption/self-assembly process [13,26,27].

The purpose of this work was to study the adsorption of organic molecules such as thiourea and 4,4'-bipyridine at the single crystal electrode surfaces. The atomic resolution data on bismuth [28,29] and antimony [30] single crystal electrodes has already been achieved under ultra-high vacuum conditions. During the experimental part of the present work, it became obvious, that in addition to the atomic resolution, on both Sb [I] and Bi [29] electrodes, achieved *in situ* in aqueous electrolytes, it is possible to visualize the adsorbed organic molecules [3] on the electrode surface under different polarization conditions [II,III]. Similar experiments have been mostly conducted only on the gold single crystal electrodes and adsorption of various thiols, 2,2'-bipyridine, 4,4'-bipyridine [4–6,15,31–37] and camphor [18,21] have been demonstrated.

Only adsorption of camphor and 2,2'-bipyridine on Bi(111) electrode [3] had been shown via electrochemical *in situ* STM.

In this work in addition to the *in situ* STM method, electrochemical impedance spectroscopy, infrared adsorption studies and DFT modeling approach were also used for analysis of the 4,4'-bipyridine layer at the Bi(111) single crystal electrode. Electrochemical impedance spectroscopy data provided more insight into the kinetics of the adsorption of thiourea at Bi(111).

4. LITERATURE OVERVIEW

4.1. Scanning tunneling microscopy (STM) in electrochemistry

The investigation of the electrode surfaces and local processes by structure-sensitive probing techniques has become an important topic in electrochemistry, since most practically relevant electrochemical systems are characterized by some structural and chemical inhomogeneities at the electrode | electrolyte interface. Such inhomogeneities can influence the local mechanisms of the electrochemical reactions in a wide resolution interval extending from the sub-nm scale of surface dislocations and adsorbate layers to some specific structural features in the micrometer range, encountered for example in electrochemical phase formation and dissolution, corrosion, as well as biological membranes and corrosion inhibitor layers.

The advent of high-resolution scanning probe microscopy (SPM) occurred in the early 1980's with the invention of the scanning tunneling microscope (STM) by Binnig and Rohrer. The first real-time imaging within a widely variable resolution range has been achieved at Pt and Au electrode surfaces by Arvia et. al. [38–40], to image morphology of the electrode surfaces with an instrument operated in the air at ambient pressure. The first high-resolution images in an electrolyte solution were obtained by Sonnenfeld and Hansma in 1986 [7]. This aspect is very important, because it is possible to image the surface during electrochemical experiment under the various polarization conditions.

While the first electrolytic STM applications were performed with conventional STM instrumentation adapted for the operation in solution, an important step was the introduction of the *potentiostatic STM method* in 1988 [41–44], allowing the diminution of the unwanted electrochemical reactions at the tip, and the control of the electrochemical processes at the electrode surface during and between STM imaging. The majority of the recent electrochemical STM applications are now based on this concept.

The most of electrochemical systems involving STM research technique use conductive electrodes, but the formation of domains with distinctly different bulk and interfacial electron transfer behavior should also be considered. The examples of this phenomenon are corrosion, formation of the insulating passive layers or adsorbate mono- or multilayers at the electrode surface. Mentioned formations at the electrode-electrolyte interface can influence the local mechanisms of electrochemical reactions in a wide resolution interval extending from the sub-nm scale of surface dislocations and adsorbate layers to structural features in the micrometer range.

Also *in situ* STM imaging of adsorbed organic macromolecules and biological membranes, electrochemical phase formation and dissolution, corrosion and corrosion inhibitor layers deal with the same phenomenon [7,45–56]. In such systems, especially in electrolytic imaging of the biological systems, it is

clear that additional scanning probe techniques, that are suitable for insulating surfaces, are an important supplement to STM.

4.2. Main aspects of STM

The STM setup uses an atomically sharp probe tip to map contours of the local density of electronic states on the surface. This is accomplished by monitoring quantum transmission of electrons between the tip and substrate while piezo-electric devices raster the tip relative to the substrate. The remarkable vertical resolution of the device arises from the roughly exponential dependence of the electron tunneling process on the tip-substrate separation, d. In the simplest approximation, the tunneling current, I_{tunnel}, can be simply written in terms of the local density of states (LDOS; $\rho_s(z, E)$) at the Fermi level (E=E_F) of the sample in which V is the bias voltage between the tip and substrate [7,45–56].

$$I_{\text{tunnel}} = V\,\rho_s(0,E_F)\exp(-2\kappa d) \tag{4.2.1}$$

and κ is the decay constant, which is related to the magnitude and the shape of the potential barrier. The decay constant may be described by an effective barrier height, φ, measured in eV according to equation

$$\kappa = \frac{\pi\sqrt{8m_e\varphi}}{h} \approx 0.51\varphi^{1/2} \tag{4.2.2}$$

where m_e is a mass of electron.

A value of $\kappa \sim 1\text{Å}^{-1}$ results in an order of magnitude decrease of the tunneling current per angstrom of electrode separation.

The effective barrier height in an electrolyte solution 0.75 Å^{-1} at 2.15 eV for instance, is found to be less than that for related vacuum junctions (being typically ~ 1.0 Å^{-1} at 4 eV) [54,55]. The diminished barrier has been associated with tunneling via the "V_0" level, or loosely speaking, the "conduction band" of the solvent [57]. Tunneling junctions may also be described in terms of the tunneling conductance, G,

$$G \approx G_0\exp(-2\kappa d) \tag{4.2.3}$$

where G_0 is associated with quantum-point contact at which the barrier has collapsed (d = 0, which corresponds to 2–3 Å internuclear separation) ($G_0 = 1/R_0$, where $R_0 = h/2e^2$ = 12.9 kΩ) [48,55].

The role of solvated ions in the tunneling process has received little attention since these species are unlikely to exist in the junction during atomically resolved imaging. In contrast, ions that are specifically adsorbed either on the tip or on the substrate will change the LDOS and the surface dipole, thereby

altering the distribution of the electrostatic potential within the gap in a manner analogous to the vacuum junctions [49,50]. In cases in which the atomic resonance of an adsorbate lies far above the Fermi level [49], the adsorbate still contributes to the LDOS due to the significant broadening of the resonance upon adsorption. If the size of the orbital is such that it extends considerably further out from the surface than the bare substrate wave functions, it will significantly contribute to the image formation [49,51,52]. For simple anions adsorbed on the metal surfaces, it is generally found that the extension of orbitals in space is more important to formation of the image than the energy of the adsorbate orbitals [51,52]. However, the recent studies show that image formation in such systems can be highly sensitive to the tunneling conductance.

Well-defined *in situ* STM experiments require the use of a bipotentiostat (Fig. 4.1a) in order to control independently the electrochemical potential of the tip and of the substrate potential relative to some reference electrode. This configuration is distinct from an UHV (ultra-high vacuum) experiments in which only the bias between the electrodes needs to be specified. In the electrochemical environment, the tip electrode is simultaneously a tunneling probe and an ultramicroelectrode. Consequently, considerable attention must be given to possible occurring of the faradic reactions at the tip demonstrated in Fig. 4.1b.

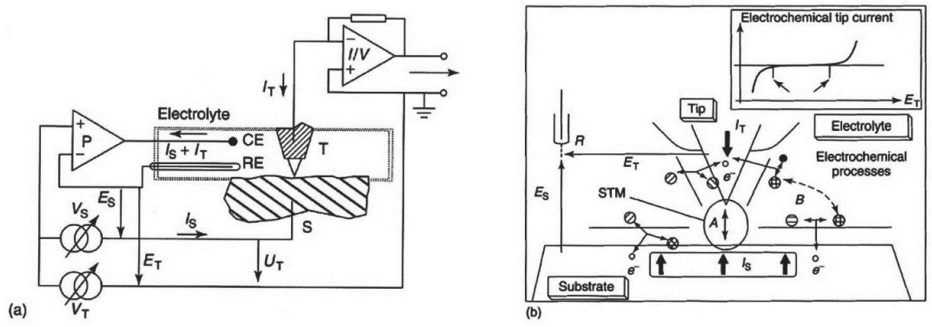

Figure 4.1. (a) Schematics of *in situ* STM bipotentiostat. (b) Schematic presentation of an immersed tunnel junction, at which in addition to direct tunneling between the tip and substrate, there is also the possibility for occurring of the electrochemical reactions at the tip and substrate. Notations: S – electrode substrate; T – tunneling tip; RE – currentless reference electrode; CE – counter electrode; E_S, E_T – potential difference of substrate and tip, respectively, versus reference electrode; I_S, I_T – current at substrate and tip, respectively. Inset: the dependency of electrochemical current on the potential E_T applied for a tip/electrode combination within ideal polarizability potential region, which is marked by arrows in the figure [54].

Mentioned faradic reactions may include redox as well as deposition and dissolution processes. Under constant current imaging conditions, the set point current is maintained by a combination of electron tunneling and the faradic

process occurring at the tip. Typically, an attempt is made to minimize the faradic contribution at the tip by coating the probe with an insulating substance leaving only the apex of the tip directly exposed to the electrolyte as indicated in Fig. 4.1b. In this way the direct electron tunneling across an electrolytic barrier is assumed to be the dominating charge transfer mechanism in the region of smallest tip-substrate separation (domain A, in Fig. 4.1b) in a similar range as in ultra-high vacuum or gas phase STM measurements. Beyond the direct tunneling domain A, both substrate surface and the tip are susceptible to electrochemical charge transfer reactions involving electrolytic compounds. Unless properly controlled, these processes can cause arbitrary changes in the surface morphology and in the chemical composition of both tip and substrate by adsorption and phase formation/dissolution processes. Furthermore, at the tip, the superposed electrochemical current components will normally disturb the STM control system by enhanced noise and fluctuations in the overall tip current. All these phenomena may deteriorate electrolytic STM imaging data by loss of resolution, insufficient reproducibility and enhanced drift. A special situation is encountered in cases, where the electrochemical processes at substrate and tip are coupled by electrolytic transport of reactants participating in both mentioned processes, since this opens an additional current pathway between these electrodes (pathway B in Fig. 4.1b). To a first approximation, it increases the "true" tunneling current, but follows a different dependence on tip substrate separation, which is governed by the overall geometry of the combined system as well as by the reactant concentration and the kinetics of electrochemical transport. In electrolyte solutions with ionic concentrations above ca. 10^{-3} M electrochemical transport beyond ca. 10 nm from the tip or substrate interface can be quantified in a good approximation by various diffusion models [7]. Typical reactants included into variable reactions are H^+, dissolved O_2, metal ions and soluble redox compounds. Especially pronounced effects are expected in the presence of redox compounds involved in the fast electrochemical charge transfer processes at both electrodes. Under redox reaction conditions, already small potential differences between substrate and tip (i.e. at small tunneling voltages) can result in considerable diffusion-controlled electrochemical steady-state currents.

The above mentioned system properties, combined with the aim to image defined electrochemical changes at the substrate imply the necessity to reduce or eliminate the superposed electrochemical reactions at the scanning tip, while keeping the electrochemical processes at the substrate under full extrinsic control.

Under the idealized condition that the direct electron tunneling between the tip and substrate, and the electrochemical charge transfer reactions are assigned to be locally separated parts of the electrolytic STM configuration, and assuming that the mechanism of the electrochemical reactions is not affected by the electron tunneling process, the electrochemical processes at both electrodes can be controlled separately by a bipotentiostatic STM setup, illustrated

schematically in Fig 4.1. It is done by the independent adjustment of the potential differences E_T and E_S between the tip and substrate, respectively, and a practically currentless reference electrode RE serving as an electrolytic potential probe. To achieve optimum reduction of the electrochemical tip currents, the tip materials should be chosen so that the electrochemical behavior in the given electrolyte solution over a reasonably wide potential range is purely capacitive. During STM operation, the tip potential E_T versus the reference electrode is kept within the region of ideal polarizability, whereas the electrochemical reactions at the substrate can be controlled by adjusting E_S. As shown in Fig. 4.1, the bipotentiostatic control is completed by a current-carrying counter electrode CE maintaining the sum of the substrate and tip currents I_S and I_T, respectively.

An additional disturbance of STM imaging can be caused by high capacitance of the electrolytic interfaces, ranging from 20 to 100 $\mu F \cdot cm^{-2}$. In electrolytic tunneling gaps, this can lead to the considerable capacitive noise pickup and to the capacitive tip current components during the distance variation and voltage modulation experiments. Thus, for the control of the electrochemical processes it is necessary to reduce the exposed surface area of the tip by applying appropriate coating techniques.

The tunneling tip should be isolated and the uncovered part is usually 5–10 μm from the tip end. The selection range of the covering materials is quite large, and the materials like fingernail lacquer, glass, epoxy, polyethylene, Apiezon^{TM} wax and other polymers are commonly in use.

A typical set point current for atomically resolved STM imaging is in the order of ~1 to 20 nA. This corresponds to an extremely large current flux $\sim 10^6$ $A \cdot cm^{-2}$ between the apex of the tip and substrate area ($<10^{-14}$ cm^2) being probed. In contrast, any faradic process would be distributed over the exposed area of the tip, which is often in the range of $\sim 10^{-8}$ to 10^{-10} cm^2 such that a 10 nA faradic current would correspond to a very high current density of 1 to 100 $A \cdot cm^{-2}$. Thus, provided that the tip electrode is suitably coated, a large faradic perturbation is required to destabilize the tunneling-based imaging process. In contrast, the exponential decrease in the tunneling current with increasing tip-substrate separation eventually leads to the limiting case in which $I_{faradic} >> I_{tunnel}$. Under appropriated conditions, the faradic current may be used to form images of the electrochemical reactivity of a surface. This is known as scanning electrochemical microscopy (SECM) in which the mass transport and heterogeneous redox activity of species within the junction mediate the tip-substrate interaction [53].

In typical STM application there is a very sharp conducting tip, placed in the scanner and made of platinum-iridium (rhodium) alloy or tungsten, over a conducting surface (conductor or semiconductor) and holding just a few atomic diameters apart, so that the electric current can flow between the two objects by means of quantum mechanical tunneling. The rapid decay of tunneling current gives to the STM remarkable sensitivity to small features present on the surface;

usually the atomic resolution is easily attained by moving the tip over the surface in a raster scan mode and measuring the height changes needed to maintain a constant tunneling current during scanning. Many modifications of the original STM and AFM (atomic force microscopy) have been developed, and they all work in a similar basic manner. A sharp probe is moved back and forth in the plane of the sample (the x and y direction) while its height (the z range) is controlled using a sensor signal sensitive to an interaction between the probe and the surface. A map of this control signal as a function of position (x–y) forms an image of the surface properties [58], approximated at the simplest case as the mechanical profile.

There are two different modes of the operations: *the constant current mode* and *the constant height mode*. In the constant current mode regime the tip is moved up and down according to the electronic (mechanical) profile of the surface. The movement across x, y and z axes is achieved by piezoelectric elements, which are controlled by a controller unit connected to the computer. In constant height mode regime, the vertical position of the tip is held constant and the current is monitored. This method has its own risk, when surface is quite rough, has high points and surface defect areas and thus, the tip can be easily broken. The advantage of this method is that high scanning speed can be achieved. The microscope is very sensitive and permits atom scale resolution, which allows screening even of absorbed molecules on the smooth surface (usually single crystal), when there is no problem with the regime of operation. The problem persists, when there is low conductance or non-conductive objects in the scanning area, which is caused by the adsorption of the dielectric molecules, or by contamination of the surface by nonconducting particles or formations (deposits) [58].

Atomically resolved STM studies require the preparation of a very flat surface with well-defined structure [55]. In order to carry out electrochemical studies at solid electrodes, the surface has to be routinely restorable to its original conditions. Flame annealing in a hydrogen-oxygen flame has proven to be particularly convenient for rapid refurbishing of the Au(*hkl*) and Pt(*hkl*) single crystal surfaces [56,59–71]. However, it was demonstrated that the crystal quality and surface structure of Au(*hkl*) and Pt(*hkl*) electrodes is very sensitive to the cooling procedure applied and the slow cooling rate in an inert gas was preferred over rapid quenching in H_2O for Au(*hkl*) [59–61,63,65,67–69]. Electrochemical or chemical polishing (Au, Ag, Cu) [54,63] and electrochemical capillary growth techniques for deposition of the Ag and Cd single crystals [72,73] may be used as an alternative or additional steps to thermal annealing. The so-called atomic layer deposition from the gas phase, as well as electron-beam evaporation and sputtering, provide another avenue for producing flat, highly oriented surface films with reasonable surface roughness [72–74].

However, during the systematic analysis of data it was found that the different preparation methods led to the different mesoscopic structures like step

bunching (depending heavily on the specific preparation procedures used) [13,14,55,56,59–64,66–69,72–78]. The influence of the electrode potential on the surface structure of Au(*hkl*), Pt(*hkl*) and Ag(*hkl*) and other face centered cubic metals has been discussed in many papers [13,14,59–64,66–69,76,77]. It was found that the surface structure of Au(*hkl*) electrodes depends noticeably on the surface charge density and thus, on the difference of electrode potential applied with respect of the zero charge potential and electrochemical work function values crucially depending on the prehistory of the electrode preparation (reconstructed, unreconstructed etc.) methods used, as well as on the other experimental details [61,63].

4.3. The crystallographic properties of Sb and Bi

Sb and Bi crystallize in a rhombohedral Bravais lattice system with an axial angle $\alpha = 57°14'$. Corresponding crystallographic structure can be seen in the Fig. 4.2. The distance between atoms inside the same layer is 2.88 Å for Sb and 3.10 Å for Bi, the distance between atoms in the neighboring layers is 3.38 Å (Sb) and 3.47 Å (Bi), correspondingly [78,79].

Both antimony and bismuth have five valence electrons and in its normal crystal modification they are crystallizing in a double layered structure, where each atom has three close neighbors from the same layer (s^2p^3-electronic configuration) and three farther neighbors from the second neighbor layer bonds with the aim of hybrid sp^3d^1 orbital.

Thus, metallic properties of the fifth group elements depend on the bonding between neighboring layers and bismuth has the stronger metallic nature than Sb [78,79]. The presence of the covalent semiconductor bonds between the atoms in the Sb and Bi lattice probably fixes the position of the surface atoms more rigidly than in the case of typical *sd*-metals (Au, Cu, Pt, Pd) [55,59–61,63,80].

According to the previous cyclic voltammetry, impedance, chrono-coulonometry and STM studies [3,29,30,63,81–93], there is no quick surface reconstruction of Sb(*hkl*) and Bi(*hkl*) within the region of ideal polarizability of these electrodes.

It is supposed that the layered structure of Sb and Bi allows to prepare a very smooth atomically flat surface areas as a result of electrochemical polishing and cleaving procedures [3,13,29,81] used in this work.

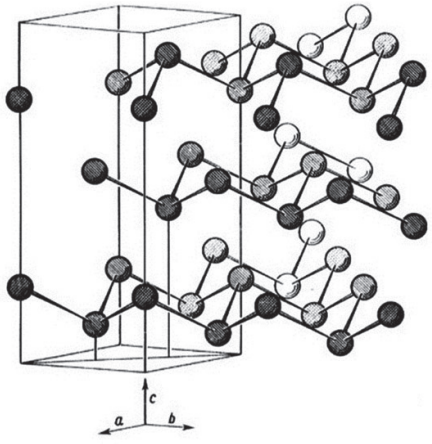

Figure 4.2. Layered structure of Sb and Bi crystals [78].

4.4. *In situ* study of the adsorbed 2D monolayers on single crystal electrodes

Two-dimensional (2D) phase transitions at solid surfaces or in the adsorption adlayers have received much attention in recent years as this phenomenon is related to the very important aspects of surface and materials science connected with the nano- and molecular technology [3–6,13–15,19,21,33–37,94,95]. The important characteristics in 2D phase transition are related to the important phenomena, like the ordered adsorption, island nucleation and growth, oscillating of chemical and electrochemical reactions, surface reconstruction, selective corrosion and corrosion inhibition, chirality of the formed surfaces and electrodeposition mechanism of the metals/catalysts. It is a very well established fact that the kinetics of 2D condensation is noticeably influenced by the base electrolyte activity and chemical composition [4,5,15,20,37] as well as by the adsorption energy of solvent molecules at the surfaces studied (i.e., 2D condensation characteristics depend on the lyophilicity of surfaces investigated). On the other hand, the structure and stability of the adsorbed monolayers are strongly affected by the symmetry of the surface structure of the adsorbate as well as by the adsorbate-adsorbent interaction Gibbs energy and adsorbate-adsorbate, adsorbate-electrolyte, adsorbate-solvent and solvent-solvent lateral interaction energies [4,5,13–15,18–21].

The exploitation of the classical electrochemical methods (impedance, cyclic voltammetry, chronoamperometry [4–6,15,18–21,33–37,94,95]) in comparison with the surface sensitive *in situ* techniques such as STM, AFM [4,6,15,31,33–37,94], and so-called vibrational spectroscopy (SNIFTIRS (subtractively normalized interfacial Fourier transform infrared spectroscopy), SEIRAS (surface enhanced infrared reflection absorption spectroscopy) [31], Raman [96,97]) complemented by DFT (density functional theory) calculation methods [22–25] will provide a complex approximation and strategy to investigate the solid | liquid interfaces in macroscopic and microscopic (molecular or atomic) levels and to develop in future the general molecular theory taking into account the influence of the crystallographic structure, electronic and chemical nature of the surface as well as the surfactant properties (molecular structure, dielectric properties and polarizability, charge density localization) on the 2D condensation phenomenon.

The influence of the surface structure of Bi(*hkl*) and Sb(111) electrodes on the thermodynamic characteristics of the adsorption of organic molecules is comparatively big [3,29,30,63,81–93]. The UHV STM studies at the cleaved Sb(111) surface (cut at the temperature of liquid nitrogen) [30,83] demonstrated the nearly ideal crystallographically flat structure of the Sb(111) surface which makes further investigation quite interesting under electrochemical conditions using *in situ* STM techniques. Electrochemically polished and cleaved Bi(111) electrode [3,29,81] is also very promising object for studies of adsorption of organic molecules. The adsorption kinetics of organic compounds on Bi

electrode is important because the thin-layer Bi electrodes can be used instead of the toxic Hg electrode for sonoelectroanalysis (stripping voltammetric detection) of heavy metal cations from the various natural environments (including whole human blood) [98,99] in the negative potential region, where the simultaneous adsorption/desorption of organic compounds is possible and probably influencing the electroanalysis data.

4.5. Cyclic voltammetry

The cyclic voltammetry is the simplest and the most widely used electrochemical technique for the characterization of the electrochemical materials and process that take place at the electrochemical interfaces. In addition to the information that can be obtained in such experiments, this technique shows two very important aspects, such as the condition the electrode surface structure (single crystal characterization) and the presence/absence of impurities in the system studied.

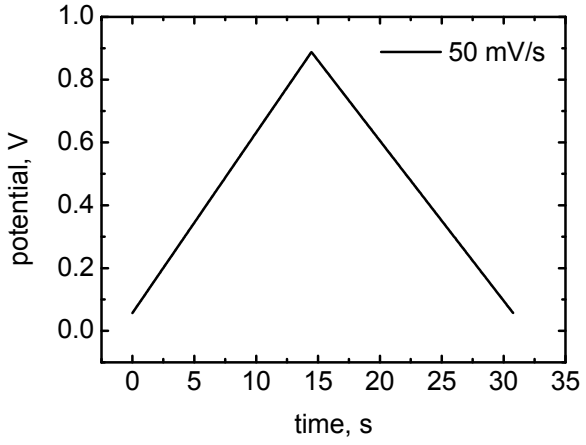

Figure 4.3. Triangular signal applied in cyclic voltammetry.

This technique consists of recording the current that circulates through the working and counter electrodes, when a constant rate potential sweep is applied. The potential sweep is linear in the time scale, which is achieved by introducing a triangular signal, whose slope (in absolute value) represents the scanning rate, ν, (Fig. 4.3).

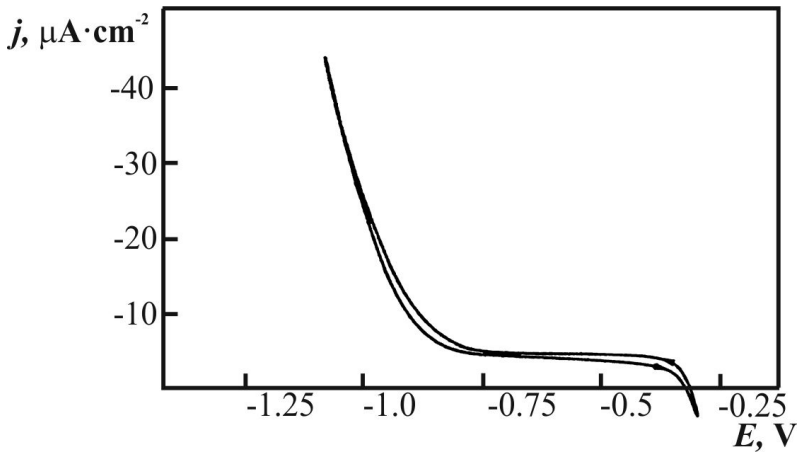

Figure 4.4. Cyclic voltammogram for Sb(111) electrode measured in 0.5 M Na_2SO_4 + 3.0×10^{-4} M H_2SO_4 aqueous electrolyte at $\nu = 50$ mV·s^{-1}.

The current density, j, represented with respect to the potential, E, is called voltammogram (Fig. 4.4). In general, different processes that can take place at the electrode can be characterized by the appearance of the oxidation or reduction peaks (or waves for irreversible processes with complicated electrochemical reaction mechanism) in the plot current vs. potential. The current peak is usually responsible for the process that takes place on the electrode, and the voltammetric waveform (or peak) provides information on the nature and kinetics of the process initiated by potential scan [100–102].

One can distinguish two major groups of electrode processes; adsorption controlled processes and diffusion controlled processes. In case of the adsorption step limited process the current peak is proportional to the sweep rate applied. Furthermore the charge circulated during the sweeps provides information on the surface coverage of the adsorbed species [100,102].

However, for diffusion step rate controlled process, the peak current is directly proportional to the square root of the potential sweep rate. That allows distinguishing this process from the other processes described above. Furthermore, the waveform depends on the kinetics of the redox reaction taking place [100,102].

4.6. Impedance spectroscopy

Impedance spectroscopy is an informative technique for analysis of different electrochemical systems and processes. Cyclic voltammetry usually takes electrodes to a condition usually far from equilibrium. In contrast, impedance methods are based on perturbation of the electrochemical cell with an alternating signal of small magnitude (~5mV), allowing measurements at nearly equilibrium or steady state conditions [102].

Sinusoidal potential perturbation is applied to the electrode:

$$E(t)=E_A \sin \omega t \tag{4.6.1}$$

where E(t) is the potential at time t, E_A is the potential amplitude, $\omega = 2\pi f$ is the radial frequency, and f is the frequency in Hz units. The current response will be a sinusoid at the same frequency, but shifted in phase:

$$i(t) = i_A \sin(\omega t + \Phi) \tag{4.6.2}$$

where $i(t)$ is the current at time t, i_A is the current amplitude and Φ is the phase shift by which the potential lags the current [102]. The impedance (total resistance of the system for ac) is defined analogously to the Ohm's law as the ratio of ac voltage and ac current gives the impedance:

$$Z = \frac{E(t)}{i(t)} \tag{4.6.3}$$

Impedance has magnitude ($Z_A = E_A/I_A$) and phase angle and thus, is a vector quantity:

$$Z = Z_A (\cos \Phi + j_i \sin \Phi) = Z' + j_i Z'' \tag{4.6.4}$$

where $j_i = \sqrt{-1}$, Z' is the real part (actual resistance) of impedance and Z'' is the imaginary part (capacitive resistance) of the impedance [102].

If sinusoidal ac voltage is applied across the pure capacitor, the impedance can be calculated according the relationship:

$$Z = \frac{1}{j\omega C} = -\frac{j}{\omega C} \tag{4.6.5}$$

where C is the capacitance of the system tested and the phase angle $\Phi = -90^o$. So the impedance depends on the ac frequency applied and Z is entirely imaginary parameter.

In the present work the impedance spectroscopy has been used for the determination of quality of electrodes and for the study of the adsorption behavior (kinetics) of thiourea and 4,4'-BP at B(111) electrode.

4.7. Adsorption kinetics of organic compounds

Frumkin and Melik-Gaikazyan first observed the frequency-dependence of the impedance of the Hg electrode adsorbing neutral organic molecules [103–113]. Later this conception has been enlarged to other metal electrodes by various

authors [63,114–117]. For the case of adsorption kinetics controlled entirely by the rate of diffusion, they deduced the following expressions for the frequency-related admittance of the electrode [103–113]

$$C_p = C_{true} + \frac{C_{ad}\left[\left(\frac{\partial\Gamma}{\partial c}\right)_E\left(\frac{\omega}{2D}\right)^{1/2}+1\right]}{\left[\left(\frac{\partial\Gamma}{\partial c}\right)_E\left(\frac{\omega}{2D}\right)^{1/2}+1\right]^2+1} \tag{4.7.1}$$

$$\frac{1}{\omega R_p} = \frac{C_{ad}\left[\left(\frac{\partial\Gamma}{\partial c}\right)_E\left(\frac{\omega}{2D}\right)^{1/2}\right]}{\left[\left(\frac{\partial\Gamma}{\partial c}\right)_E\left(\frac{\omega}{2D}\right)^{1/2}+1\right]^2+1} \tag{4.7.2}$$

where Γ is the Gibbs adsorption (surface concentration); μ is the chemical potential; and ω is the angular frequency equal to $2\pi f$; C_p is the parallel interfacial capacitance; $C_{true} = (\partial q/\partial E)_{\Gamma,\mu}$ is the interfacial capacitance as ac frequency $f \rightarrow \infty$, $C_0 = (\partial q/\partial E)_{\Gamma,\mu} + (\partial q/\partial\Gamma)_E\,(\partial\Gamma/\partial E)_\mu$, C_0 is the differential capacitance as $f \rightarrow 0$; $C_{ad} = C_0 - C_{true} = (\partial q/\partial\Gamma)_E\,(\partial\Gamma/\partial E)_\mu$, C_{ad} is the adsorption capacitance, caused by the dependence of Gibbs adsorption (Γ) (or surface coverage θ) on E applied and R_p is the parallel resistance [104,105].

As shown by Armstrong et al. [106], if the diffusion controlled relaxation time ($\tau_D = 1/2\pi f_D$) is defined as

$$\tau_D = (\partial\Gamma/\partial c)^2_E / D \tag{4.7.3}$$

and a Cole-Cole distribution [107] of relaxation times about τ_D is assumed (with the particular value α=0.5 in their Eq. (4.7.13) [107], which for the case of relaxation of dielectric polarization leads to the frequency dependence of the real ε' and imaginary ε'' parts of the complex dielectric constant ε*) then Eqs. (4.7.1) and (4.7.2) can be rewritten as (known as a frequency related admittance plots)

$$C_p = C_{true} + \frac{C_{ad}\left[\left(\frac{\partial\Gamma}{\partial c}\right)_E\left(\frac{\omega}{2D}\right)^{1/2}+1\right]}{1+(2\omega\tau_D)^{1/2}+\omega\tau_D} \tag{4.7.4}$$

$$\frac{1}{\omega R_p} = \frac{C_{ad}(0.5\omega\tau_D)^{1/2}}{1+(2\omega\tau_D)^{1/2}+\omega\tau_D} \tag{4.7.5}$$

Eqs. (4.7.4) and (4.7.5) require that $1/\omega R_p$ versus C_p (so called Cole-Cole plot) should take the form of a quarter-circle, intersecting the C_p-axis at the values C_{true} and ($C_{true} + C_{ad}$) [106–109], if the diffusion step is a rate limiting stage for total adsorption process.

For the case of adsorption kinetics controlled entirely by the rate of a heterogeneous charge transfer process, Frumkin and Melik-Gaikazyan [103,104]

deduced the following equations for the frequency-related admittance of the electrode:

$$C_p = C_{true} + \frac{C_{ad}(\partial\nu/\partial\Gamma)^2_{E,c}}{\omega^2+(\partial\nu/\partial\Gamma)^2_{E,c}} \tag{4.7.6}$$

$$\frac{1}{\omega R_p} = \frac{C_{ad}(\partial\nu/\partial\Gamma)_{E,c}\omega}{\omega^2+(\partial\nu/\partial\Gamma)^2_{E,c}}, \tag{4.7.7}$$

where ν [mol·cm^{-2}·s^{-1}] is the net rate of adsorption step due to the departure from equilibrium conditions.

If τ_D is defined as:

$$\tau_D = \left(\frac{\partial\Gamma}{\partial\nu}\right)_{E,c} \tag{4.7.8}$$

and as the relaxation time of the heterogeneous charge transfer (adsorption) process is defined as $\tau_K = 1/2\pi f_K$, then from Eqs. (4.7.6) and (4.7.7) we have

$$C_p = C_{true} + \frac{C_{ad}}{1+\omega^2\tau_K^2} \tag{4.7.9}$$

$$\frac{1}{\omega R_p} = \frac{C_{ad}\omega\tau_K}{1+\omega^2\tau_K^2}. \tag{4.7.10}$$

Thus, according to [106,109], the $1/\omega R_p$ versus C_p plot should take the form of a semi-circle with coordinates of center $C_p=C_{ad}/2+C_{true}$; $1/\omega R_p=0$. Eqs. (4.7.9) and (4.7.10) have the same form as the Debye-Pellet equations for the relaxation in a dielectric with a single relaxation time [106,107]. It should be noted that on the basis of the Frumkin adsorption isotherm, the following equation for the diffusion relaxation time has been derived

$$\tau_D = \frac{\Gamma_m^2\theta^2(1-\theta)^2}{c^2D[1-2a\theta(1-\theta)^2]}, \tag{4.7.11}$$

and for the adsorption relaxation time,

$$\tau_K = \frac{\Gamma_m\theta(1-\theta)}{\nu_0[1-2a\theta(1-\theta)]}, \tag{4.7.12}$$

by Retter and Jehring [94], where a is the Frumkin interaction coefficient, adsorption exchange rate is ν_0 and Γ_m characterizes the influence of the maximal Gibbs adsorption and the surface coverage θ on the corresponding relaxation times. Therefore, the intermolecular interaction energy plays a very big role in determining crucially the τ_D and τ_K values.

The situation of mixed diffusion and heterogeneous charge transfer step control was studied in the most general case by Lorenz and Möckel [63,111–113,116–121]. The frequency-related admittance has been expressed by the relations

$$C_p = C_{true} + \frac{C_{ad}\left[1+(0.5\omega\tau_D)^{1/2}\right]}{\left[(0.5\omega\tau_D)^{1/2}+\omega\tau_K\right]^2+\left[(0.5\omega\tau_D)^{1/2}+1\right]^2} \qquad (4.7.13)$$

$$\frac{1}{\omega R_p} = \frac{C_{ad}\left[(0.5\omega\tau_D)^{1/2}+\omega\tau_K\right]}{\left[(0.5\omega\tau_D)^{1/2}+\omega\tau_K\right]^2+\left[(0.5\omega\tau_D)^{1/2}+1\right]^2}\,. \qquad (4.7.14)$$

If τ_K and τ_D are of the same order, the $1/\omega R_p$ versus C_p plot gives a gradual transition from a quarter-circle (at low frequencies *f*, when there is effectively complete diffusion control) to a semi-circle (at high frequencies *f,* when the control is effectively heterogeneous) [111,112].

According to the Lorenz model the impedance values for so-called adsorption branch in parallel to C_{true} can be calculated as [105,111,119]

$$Z_l' = (0.5\tau_D)^{1/2}\,\omega^{-1/2}\,C_{ad}^{-1} + \tau_K C_{ad}^{-1} \qquad (4.7.15)$$

$$Z_l'' = (0.5\tau_D)^{1/2}\,\omega^{-1/2}\,C_{ad}^{-1}\,(\omega C_{ad})^{-1} \qquad (4.7.16)$$

Thus, if the diffusion is the limiting stage of an adsorption process, then the equilibrium values of differential capacitance at $\omega \to 0$ can be obtained by the linear extrapolation of the C_{ad}, $\omega^{1/2}$ dependence to $\omega^{1/2}=0$, as well as can be calculated by Eq. (4.7.17)

$$C_{ad}(\omega=0) = C_{ad}^2(\omega)R_p^2(\omega)\,\omega^2+\{(C_{ad}(\omega)R_p(\omega)\,\omega-1)R_p(\omega)\,\omega\}^{-1}\,, \qquad (4.7.17)$$

where $C_{ad}(\omega)$ and $R_p(\omega)$ are the values of the differential (additional) capacitance and parallel resistance at ω=const, respectively [113,118]. Thus, by linear extrapolation of the $R_S(\omega)$-values to $\omega \to\infty$, the solution resistance $R_S(\omega) = R_{el}$ can be determined. Since the amount of organic compound added is small and usually it does not affect the solution resistance, one can assume R_{el} to be equal to the ohmic component R_S of the impedance in the pure base electrolyte solution [103,104]. However, if the added amount of organic compound is very high, there are some deviations toward higher series resistance values.

It was shown [111,119], that if, at a given frequency, the adsorption process is characterized by the additional capacitance $C_{ad}(\omega)$ and by the parallel resistance $R_p(\omega)$, which are assumed to be parallel in the equivalent circuit (i.e., adsorption model), then for a slow diffusion step

$$\cot\delta = R_p(\omega)C_{ad}(\omega) = 1 + \frac{\sqrt{2D}}{\left(\frac{\partial\Gamma}{\partial c}\right)_E}\frac{1}{\sqrt{\omega}} = 1 + \frac{M}{\sqrt{\omega}}, \qquad (4.7.18)$$

where M is the slope of the cot δ vs. $\omega^{-1/2}$ plots. However, for some compounds at very low frequencies noticeable deviations have been observed, explained according to Lorenz [111,119] and Damaskin et al. [108,109,114] by the two-dimensional association of the adsorbed molecules at the metal | solution interfacial region. In this case the value of cot δ can be calculated as

$$\cot\delta = \frac{k_1\left(k_2+k_1\frac{\sqrt{\omega}}{M}\right)+\left(\frac{\omega}{\omega_0}\right)^2\left(k_3+\frac{\sqrt{\omega}}{M}\right)}{\left[k_1^2+\left(\frac{\omega}{\omega_0}\right)^2\right]\left(\frac{\omega}{\omega_0}+\frac{\sqrt{\omega}}{M}\right)+\frac{\omega}{\omega_0}(k_1k_3-k_2)}, \qquad (4.7.19)$$

where ω_0 is the exchange rate of the two-dimensional association, and k_1, k_2 and k_3 are the certain constants characterizing the process of two-dimensional association [108,109,113,114,120].

Usually, the components of the adsorption impedance are calculated from the impedance data of the cell used for the measurements (series circuit), i.e., from $C_S(\omega)$ and $R_S(\omega)$ following the procedure described in Refs. [108,109, 113,114,118,119].

4.8. Infrared (IR) spectroscopy

Electrochemical techniques provide only macroscopic information and do not allow the identification of the species that give rise to the detected current. To solve these problems, electrochemical system is usually coupled to a spectroscopic equipment (IR, SERS, SNIFTIRS) or microscopic (STM, AFM) so that structure and/or chemical composition of the interface can be obtained under controlled electrochemical conditions.

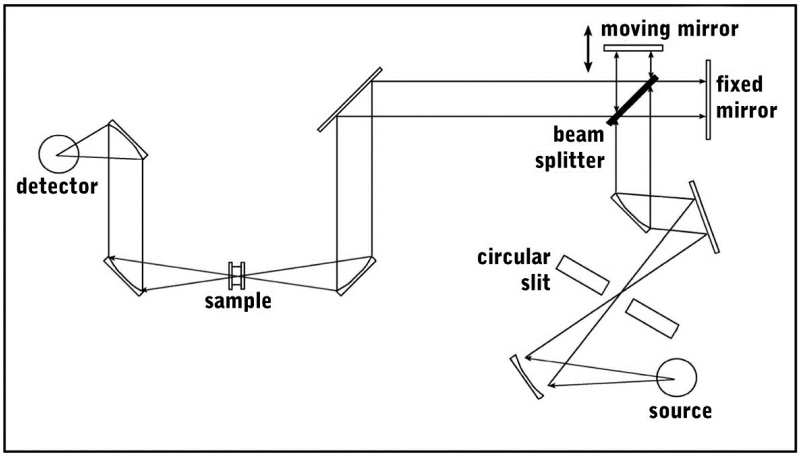

Figure 4.5. Optical diagram of a Fourier transform spectrometer equipped with a Michelson interferometer [122].

The device used to obtain infrared spectra is known as spectrometer. This system may be dispersive (which uses prism or diffraction grating to select the IR radiation wavelength reaching the sample) or Fourier transform (FT) type [123,124]. Fig. 4.5 shows a diagram of a Fourier transform type spectrometer equipped with a Michelson interferometer consisting of two mirrors (one fixed and one mobile). There is a beam splitter between them which transmits half the radiation to the fixed mirror and reflects the other half to the moving mirror. At the time when fixed and moving mirrors are not at the same distance from the splitter, radiation travels different distances before returning to the splitter. This difference in distances travelled by the radiation is known as optical difference (or optical delay, δ). The graphical representation of the intensity of radiation reaching to the detector versus optical delay is known as interferogram (IFG). Applying mathematical operation known as Fourier transform (FT), the interferogram becomes spectrum (plot of radiation intensity versus the number of waves).

Better signal to noise ratio (SNR) can be achieved with Fourier transform spectrometers because the radiation passes through the sample and reaches to the detector directly without going through a slit and a monochromator for select a particular wavelength, which reduces the intensity of radiation as it is common in the dispersive systems. Furthermore, with FT spectrometer radiation can be measured simultaneously over a wide range of wave number (limited by the response of the detector and the beam splitter used), so that these systems are much faster than the dispersive, where only a small range of wavelengths can be measured in the same experience [123,124].

There are two basic modes for acquisition of IR spectra depending on whether the interferometer (moving mirror) is sweeping all positions to acquire interferogram (linear mode) or, conversely, this acquisition takes place in steps (step-scan). The variation of optical delay versus time and program of applied potential in the spectroelectrochemistry experiments in each acquisition modes is depicted in Fig. 4.6, where A and B parts are showing the linear mode, C shows the "step-scan" mode. In respect to the variation of electrode potential in spectroelectrochemistry experience, the acquisition in linear mode can be made in static or dynamic mode. In the first case (Fig. 4.6 A) electrode potential is fixed as the reference potential (E_0) and the interferogram is recorded, which is processed by Fourier transformation and the reference spectrum is obtained. Each spectrum arises from an average derived of a certain number of interferograms (Fig 4.6 shows 10 interferograms) that makes possible to improve signal to noise ratio of the final spectrum. Then, the same process is repeated, but setting the potential of the electrode to the sample potential (E_1).

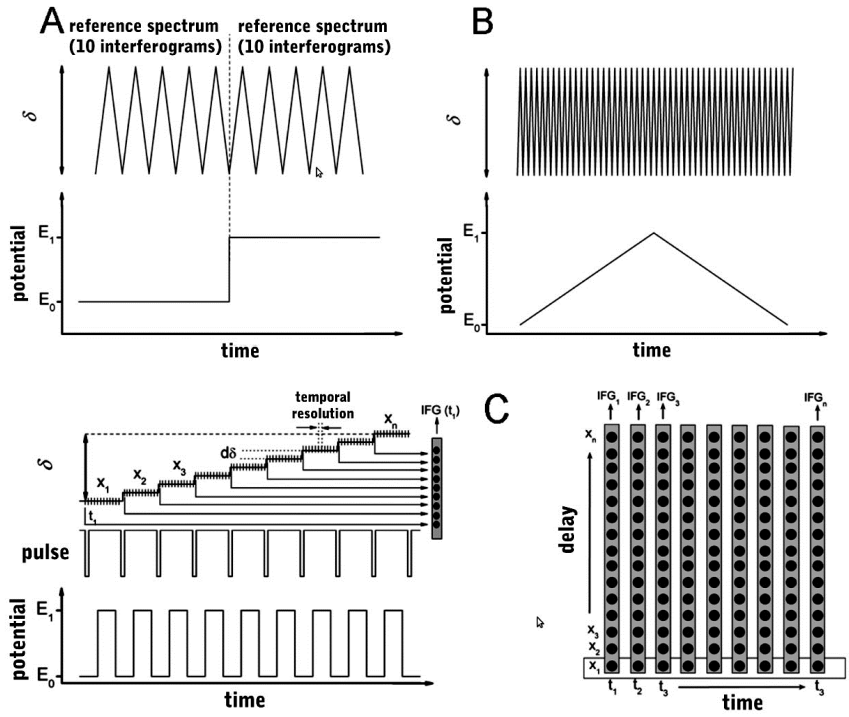

Figure 4.6. Different modes of acquisition of IR spectra; linear mode: (A) static, (B) dynamic. (C) "step-scan" mode.

On the other hand, the acquisition of interferograms in dynamic mode (Fig. 4.6 B) takes place while the potential is swept between the limits E_0 and E_1. The scanning speed in this case should be low (about 2 mVs^{-1}) for the variation of potential (ΔE) in each series of interferograms (whose average will be a spectrum) to be as small as possible. After the acquisition, the series of spectra as a function of electrode potential is obtained, allowing to study the change in the absorption bands with a change of the potential of the electrode. In both cases it is necessary to acquire and summarize a sufficient number of interferograms to achieve adequate SNR.

The acquisition time on a linear mode interferogram is limited by mechanical movement of the interferometer, but could be in the order of 10 ms at the expense of lower quality of the interferogram. This temporal resolution can be improved in the "step-scan" mode (Fig. 4.6 C), in which the moving mirror varies its position step by step, keeping the fixed position for a certain time. In each position, reversible process to study (in our case changes at the interface caused by a potential jump) is activated by an external signal (pulse). Then the mirror changes to the other position, repeating the same process described above until the moving mirror travels all the necessary positions to create the interferogram. Fig. 4.6 C (right) shows schematically the data acquisition at the

conditions of the "step-scan" mode. Each row $\boldsymbol{x}$ corresponds to the different position of the mirror. At the end of the acquisition, there are series of interferograms collected at different times.

Currently with the commercial FT-IR equipment equipped with the proper digitizer cards and using the adequate FT-IR detectors, like Mercury-Cadmium-Telluride detector TRS-MCT (Time-Resolved Mercury Cadmium Telluride), temporal resolution up to 5–10 μs can be achieved, which are sufficient for electrochemical systems implied in ATR-SEIRAS (attenuated total reflection surface enhanced infra-red absorption spectroscopy) regime, where the response of the system is limited by the time required for charging/discharging of the double layer (known as double layer time constant) [125]. Time constant of the electrochemical system with the working electrode with an area of 0.5 cm^2, (determined by applying impedance method) is about 0.29 ms [126]. It should be noted that using the external digitizer card and TRS-MCT photovoltaic detector, the temporal resolution can be achieved of the order of nanoseconds [127].

4.9. Density Functional Theory (DFT) calculations

DFT method has found its first implementations in solid-state physics for electronic structure calculations in 1960's. Over time it became popular in computation chemistry due a good balance between accuracy and computational cost. New functionals developed in the 1990's allowed to investigate systems much larger than those suitable for *ab initio* methods. Nowadays, high level *ab initio* methods, either variational or perturbative, are usually applied to find highly accurate results on smaller systems, providing benchmarks for developing density functionals, which then can be applied to much larger systems. Nevertheless, DFT is not just another way of solving the Schrödinger equation, nor is it simply a method of parameterizing empirical results. DFT is a completely different, formally rigorous way of approaching any interacting problem by mapping it exactly to a much easier to solve non-interacting problem. Nowadays, its methodology is applied in a large variety of fields to analyze many different problems, with the ground-state electronic structure problem simply being the most common [128]. In the formulation given by Kohn, Hohenberg and Sham in the 1970's the real system is described by an effective one-body system. To achieve that goal, the complex many-body wave function, which is the solution of the Schrödinger equation, is abandoned in favor of the density which only depends on the three spatial coordinates. The energy is just a function dependent on this function, i.e., an energy density functional [129].

DFT describes the electronic states of atoms, molecules and materials in terms of the three-dimensional electronic density of the system, which is a great simplification over wave function theory (WFT), involving a 3N-dimensional antisymmetric wave function for a system with N electrons [130].

In practical work, DFT is almost always applied in the form introduced by Kohn and Sham, including its spin-polarized extension [130]. The basic quantity in DFT is the many-electron spin density, ρ. The spin-polarized Kohn-Sham formalism involves a determinant formed from a set of N fictitious single-particle spin-orbitals corresponding to a non-interacting system of electrons with the same spin densities, ρ_a and ρ_b, as the real system, where ρ is the sum of ρ_a and ρ_b. The spin density ρ_a is the 3-dimensional electron density of all spin-up electrons, and ρ_b is the same for spin-down electrons [130]. In the original Kohn-Sham formalism (applicable to closed shell molecules and nonmagnetic solids), ρ_a is equals to ρ_b. The original Kohn-Sham formalism may also be labeled spin-restricted Kohn-Sham or restricted Kohn-Sham approximations, and the spin-polarized version may be called spin-unrestricted or unrestricted. "Spin density" is a generic term for the density associated with the subset of electrons characterized by the same definite value of S_z, i.e., either α or β (thus one might say "spin-up density and spin-down density" rather than "spin densities"). In a many-electron system comprised of both spin-up and spin-down electrons, the term spin-density is also sometimes used to refer to the position-dependent difference between the up and down spin densities, or to the vector analog of this quantity [130].

Now it is well appreciated that quantitatively accurate electronic structure calculations must include electron correlation parameter. Two types of electron correlation should be recognized, the first called dynamical electron correlation and the second called static correlation parameter, near-degeneracy correlation, or non-dynamical correlation. Dynamical correlation is a short-range effect by which electrons avoid one another to reduce electron repulsion. It is a very general effect for all finite systems containing two or more electrons. Accounting for dynamical correlation by a configuration interaction wave function is very slowly convergent and requires a very large number of configurations. Other correlation effects, which are very system specific and can be either medium ranged or long ranged, can be accounted for a large extent by mixing a small number (sometimes two, sometimes more) of configurations that are "nearly" degenerate [130]. Such correlation effects are called static or near-degeneracy correlation and systems exhibiting significant static correlation effects are often called multireference systems; likewise, WFT methods based on multi-configurational zero-order states are often called multireference methods. Due to partially filled *d* subshells, and nearly degenerate $(n + 1)s$ and *nd* subshells, systems containing transition metals often have an overabundance of low-lying nearly degenerate states, and near-degeneracy correlation effects on the ground-state structure, electron distribution, and energy of transition metal systems can be very large. Even though static correlation can often be accounted for a zero-order approximation by a small number of configurations, it is often very difficult to include correlation effects in a well-balanced way in WFT calculations on multi-reference systems [130]. DFT, however, remains simple for such systems and is often surprisingly accurate. This empirical fact

adds to the advantage of computational efficiency in making DFT a preferred method for transition metal chemistry.

Kohn-Sham spin-orbitals, $\Psi_{j\sigma}$ where σ is α or β and j denotes the other quantum numbers, are obtained by a self-consistent field (SCF) calculation and are formally functions of the exact density of the system. Then

$$\rho_\sigma = \sum_{j}^{occ} \left|\psi_{j\sigma}\right|^2 \tag{4.9.1}$$

where σ is the spin component (α or β), the spin-orbitals are normalized, and the sum is over occupied orbitals of a given spin component. The electronic energy of the system is approximated as a sum of four terms: T_n, the kinetic energy of a system of noninteracting electrons with the same spin densities as the real system, ε_{ne}, the interaction of the electron distribution with the nuclear framework, ε_{ee}, the classical Coulomb energy of the spin densities interacting with each other and with themselves, and ε_{xc}, called the exchange-correlation energy, which is everything else (everything except T_n, ε_{ne}, and ε_{ee}). Therefore ε_{xc} includes the interaction correction to T_n, the correction to V_{ee} for the fact that real electrons do not interact with themselves, the exchange energy (due to the indistinguishability of electrons exchanging their space and spin variables), and the correlation energy (due to the fact that the many-electron spin densities are not uncorrelated products of spin-orbital densities). ε_{xc} is written as a functional, called the spin-density functional, of the spin densities. Since the Kohn-Sham spin-orbitals are functions of the spin-densities, ε_{xc} can depend explicitly on the spin densities and also implicitly on them by depending on the spin-orbitals [130].

The effective potential corresponding to ε_{xc} is generated from a functional of the spin densities. The spin-polarized Kohn-Sham formalism and the spin-density functional are usually just called Kohn-Sham theory and the density functional, and approximations to the latter are also called density functionals. The density functional is usually written as the sum of an "exchange" part and a "correlation" part. One should be careful though because the meaning of these terms is different in DFT and in WFT. In particular, DFT correlation includes only dynamic correlation, and DFT exchange includes not only exchange, but also some static correlation, although the latter is present in an unspecified and uncontrolled way [130].

Hybrid DFT is a type of generalized Kohn-Sham theory. It involves combining Hartree-Fock exchange, which is orbital-dependent, with explicit functions of local spin densities and their gradients. Further generalizing hybrid functionals to include dependencies on the local Laplacians of the spin densities or on the local spin kinetic energies, computed from the spin-orbitals, yield hybrid meta functionals, and these are the most powerful functionals available [130].

The Kohn-Sham orbitals correspond to a fictitious non interacting system with the same electron density as the correct many-body function. They are introduced primarily to get an approximation for the kinetic energy, which equals:

$$T = \frac{1}{2}\tau_\alpha + \frac{1}{2}\tau_\beta \,, \tag{4.9.2}$$

where

$$\tau_\sigma = \frac{\hbar^2}{m_e}\sum_j^{occ} \left|\nabla\psi_{j\sigma}\right|^2 \tag{4.9.3}$$

where $\hbar$ is the Planck constant divided by 2π, and m_e is the mass of an electron. Since the density computed from the Kohn-Sham orbitals is an approximation to the exact density, one-electron properties like dipole moments are meaningful. Nevertheless, most properties that depend on the individual orbitals should be interpreted with care. One important exception is the orbital energy of the highest occupied molecular orbital (HOMO). This is correctly interpreted as the negative of the lowest ionization potential [130] (for solids that would be the work function). With the same precaution, many studies do employ DFT molecular orbitals to interpret the electronic origins of chemical bonding and reactivity [130] have been published.

The Dirac-Slater approximation is the oldest approximation to a density functional conception. For using with Kohn-Sham theory it must be re-normalized [130], and is now usually called the local spin density approximation (LSDA) since it depends only on spin densities. It can be derived from the exact exchange energy of a uniform electron gas (UEG), which is a somewhat unphysical system in which a constant electron density is neutralized by a constant background positive charge (rather than by discrete nuclear charges). The UEG correlation energy can be calculated numerically and it fits in various ways and therefore leads to the LSDA for correlation.

The next level of complexity in density functionals is to add dependence on the gradients of the spin densities; in particular the functional depends on the unitless reduced spin-density gradients, s_σ, which are proportional to $\|\nabla\rho_\sigma|/\rho_\sigma^{4/3}$. Such functionals are called generalized gradient approximations (GGAs). Popular GGAs include: BP86, where B denotes Becke's exchange functional published in 1988 [131] and P86 denotes Perdew's correlation functional published in 1986 [132]; BLYP, where LYP denotes the Lee-Yang-Parr correlation functional [133]; PW91, from Perdew and Wang published in 1991 [134] and PBE – a functional of Perdew, Burke, and Ernzerhof [135]. The modified Perdew-Wang functional of Adamo and Barone [136], called mPWPW, is very similar to PBE. It should be noted, that GGAs may combine an exchange

functional from one source with a correlation functional from another, or they may both be from the same source. Thus, BP86 and BLYP combine B88 exchange with P86 or LYP correlation, respectively; PW91 combines PW91 exchange with PW91 correlation; PBE combines PBE exchange with PBE correlation; mPWPW combines mPW exchange with PW91 correlation; SLYP combines the Slater LSDA exchange with LYP correlation; and PBELYP combines PBE exchange with LYP correlation [130]. It is important to note, that in the nomenclature frequently used any functional that depends only on local properties, e.g., LSDA or GGA, is called local and other functionals, such as hybrid GGAs, are called nonlocal. In the older literature, GGAs are sometimes called nonlocal or gradient-corrected, but this usage is now becoming uncommon [130].

The density functionals that perform best for main-group element chemistry are not the same as those that perform best for transition metals. In solid-state chemistry local functionals are often chosen, partly because they are easier to apply to the extended systems. In organic chemistry, the hybrid functionals are the most typical choice, because of their demonstrated superior predictions of energetics; by far the most popular such hybrid functional is B3LYP [130], which is a hybrid GGA put together by Stephens et al. [137] on the basis of earlier work by Becke and others [131,133,138]. The correlation functionals of B3PW91 and B3LYP are based on PW91 and LYP, respectively, but are optimized specifically for use in a hybrid functional, whereas the most straightforward hybrid functionals result from simply replacing a percentage (here called X) of local density functional exchange by Hartree-Fock exchange, i.e., B3LYP and B3PW91 both have X = 20 and each one has two other new parameters as well [130].

Despite the great progress that has been made in modeling implementing DFT methods, comparison to experimental processes is still limited, not only by the quality of the density functionals (and sometimes by inadequate basis sets or noninclusion of scalar and/or vector relativistic effects), but also by the inability to include simultaneously all aspects of finite temperature, surface coverage, partial pressures of all species presented in the system, dopants, co-adsorbents, surface reconstruction and local morphology, crystallographic defects, and consideration of all possible reaction (adsorption) steps and pathways. Nevertheless, a lot has been learned and some progress is accelerating, however, a considerable space for improvement still remains, but the future of the calculation methods is likely to be exciting [130].

5. EXPERIMENTAL

5.1. Materials and methods

The surfaces of $Sb(111)^{C}$ and $Bi(111)^{C}$ planes have been prepared by cleaving of the Sb or Bi single crystals at the temperature of liquid nitrogen inside of the glove box in Ar (92%) + H_2 (8%) atmosphere. For comparison the surface of the basal $Sb(111)^{EP}$ and $Bi(111)^{EP}$ planes have been prepared by electrochemical polishing in the KI + HCl aqueous solution at a current density $j < 1.5$ A·cm^{-2} as well. After either cleaving or electrochemical polishing the surfaces were submerged under cathodic polarization (E = –0.8 V vs. Ag|AgCl in saturated KCl aqueous solution) into the slightly acidified sodium sulfate (concentration varies slightly depending on the metal studied) aqueous solution, previously saturated with Ar (92%) + H_2 (8%) mixture. The self-made hermetic three-electrode cell with large Pt counter electrode and Ag|AgCl, KCl sat. in H_2O reference electrode, connected to the *in situ* STM cell through Luggin capillary, has been used. The region of ideal polarizability has been obtained using cyclic voltammetry and a good agreement with the results discussed [3,29,30,63,81–93] and obtained using impedance method (AUTOLAB PGSTAT 30 with FRA2 system) and discussed later was established. For impedance analysis, 5mV ac modulation was fixed and the frequency, f, was varied from 1×10^{-1} to 1×10^{5} Hz. The impedance measurement system was calibrated using various standard equivalent circuits. The differential capacitance (C) values were measured at a fixed constant frequencies (usually f=210 Hz). The quality of the surfaces investigated within the potential range where the adsorption of 4,4'-BP and TU takes place, was checked using cyclic voltammetry method (CV) at scan rates from 5 to 500 mVs^{-1}.

The Molecular Imaging PicoSPM^{TM} measurement system applying the Apiezon^{TM} coated tungsten STM tips, prepared in our laboratory, were used. The STM-tips and measurement system were tested and calibrated using HOPG basal plane $C(0001)^{C}$ (SPI^{TM}). All STM images were recorded in constant current mode with tunneling currents from 0.5 to 10.0 nA. For image processing and surface roughness analysis the Nanotec Electronica WSxM^{TM} [139] and Gwyddion [140] free software products were used.

The *in situ* infrared spectra were measured using Perkin-Elmer Spectrum GX FTIR system equipped with a liquid nitrogen-cooled midrange MCT detector [141–143]. Infrared beam was directed through a ZnSe wire grid polarizer and a ZnSe lens to the Si hemisphere at 65 degrees of incidence (mainly p-polarization mode was used). SEIRAS spectra were collected during 3 minutes at a resolution of 4 cm^{-1} at fixed potential, and the measurement cycle was repeated at least 3 times. The resulting spectra were calculated by dividing the sample spectrum at fixed potential with the reference spectrum measured at reference potential and presented as absorbance $\boldsymbol{A}$. Therefore, the positive-going bands represent a gain of a particular species at the sample potential relative to

that of the background reference potential. Bi film was deposited on a flat side of a 10 mm diameter Si hemisphere, using a chemical deposition procedure [142].

Water for preparation of electrolyte solutions was treated with the Milli Q+ purification system. Solutions were prepared volumetrically using H_2SO_4 (double distilled, Aldrich), 4,4'-bipyridine (Fluka *purum*, purity > 99%), thiourea (Sigma-Aldrich, *puriss. p.a.,* purity > 99.0%) and Na_2SO_4, purified by triple recrystallization from water, and treated in vacuum to dryness. Na_2SO_4 was also calcined at 700 °C immediately prior to the measurements. The temperature during the experiment was kept at 298±0.1 K.

5.2. Calculations

The complementary computational study was conducted in order to establish the underlying molecular model for the experimentally observed adsorption patterns of 4,4'-BP. At a preliminary stage, the interaction energy (ΔE_{int}) versus distance from the surface dependencies, i.e., potential energy curves, were calculated for three possible orientations and for six possible positions of the 4,4'-BP molecule relatively to a Bi_{24} cluster [22,25]. These calculations were conducted using the Gaussian 09 program [144], hybrid exchange-correlation functional CAM-B3LYP [145], LanL2DZ (Los Alamos National Laboratory double zeta) basis set with additional polarization functions for Bi atoms, and 6–311+G** basis set for H, C and N atoms, constraining geometry of the Bi cluster and optimizing internal geometry of 4,4'-BP molecule. The mentioned methods were tested and the applicability of Bi_{24} cluster model have been verified in our previous works [22,25].

At the second stage, a periodic model of the Bi(111) surface was developed and used. The vdW-DF2 (van der Waals density functional, second version [146]) and M06-L (meta-hybrid generalized gradient approximation functional) functionals were applied as implemented in GPAW 0.9 (grid-based projector-augmented wave method) code [147], using the grid-spacing of 0.16 Å for surface structure, and completed with default pseudopotentials. These calculations were performed partially at Amazon Elastic Compute Cloud with an in-home developed desktop-to-cloud migration tool [148], fixing bismuth atom positions in the slab and using partially restricted geometry for the 4,4'-BP molecule. Two-layer thick bismuth slab in a 1.362 nm×1.573 nm×3.0 nm supercell with Periodic Boundary Conditions in *x*,*y*-directions on a 2×2×1 Monkhorst-Pack *k*-point sampling grid, including the dipole correction in *z*-direction, have been used for analysis of the interfacial structure.

At the third stage, the structure of several molecular patterns of 4,4'-BP molecules was optimized on Bi slab using the vdW-DF2 functional until the forces between the atoms were smaller than 0.10 eV/nm. Two-layer thick bismuth slab in a 0.908 nm×2.359 nm×3.0 nm supercell with the Periodic

Boundary Conditions in *x*,*y*-directions on a 2×4×1 Monkhorst-Pack *k*-point sampling grid, and including the dipole correction in *z*-direction, was used. The optimized structures of the adsorption models were recalculated to obtain PBE (functional of Perdew, Burke and Ernzerhof), vdW-DF2 and M06-L interaction energies according to the equation:

$$\Delta E_{int} = E(\text{adsorption model}, \Delta z) - E(\text{surface model}) - E(\text{4,4'-BP model}) \quad (5.1)$$

where Δz is the distance between the surface plane and N atom in the 4,4'-BP molecule. Finally, for the selected models the theoretical Tersoff-Hamann STM images using the Atomistic Simulation Environment (ASE) approximation [149] were generated. The electrostatic charges were obtained using Density Derived Electrostatic and Chemical Charge (DDEC) method [150]. Avogadro tool was used for visualization of the results calculated [151].

6. RESULTS AND DISCUSSION

6.1. (I) Surface structure of Sb(111) single crystals

Fig. 6.1.1 represents cyclic voltammetry data for Sb(111) electrode in 0.5 M Na_2SO_4 + 3.0×10^{-4} M H_2SO_4 aqueous solution. Current density does not exceed $-10\mu A\cdot cm^{-2}$ within the region of E from –1.0 to –0.45 V. At –0.42 V, the current passes through zero and the dissolution of antimony starts according to the equation (6.1)

$$Sb + 3H_2O = Sb_2O_3 + 6H^+ + 6e^- \qquad (6.1)$$

Potential of zero charge for Sb(111) is $E_{q=0}$ = –0.46 V [93], which almost coincides with the potential, where antimony surface starts dissolving according to the voltammetry data, given in Fig. 6.1.1 It is obvious that slightly acidified electrolyte solution shifts the point, where the dissolution of Sb(111) starts, toward less negative potentials, as discussed in Ref. [93].

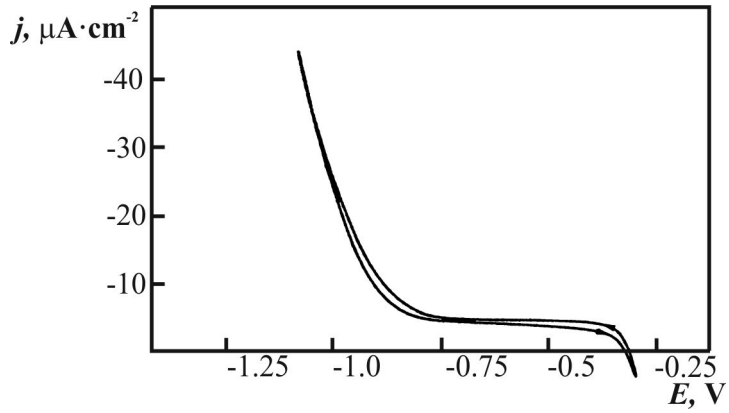

Figure 6.1.1. Cyclic voltammogram for Sb(111) in 0.5 M Na_2SO_4 + 3.0×10^{-4} M H_2SO_4 aqueous electrolyte at ν = 50mVs^{-1}.

The surface of Sb(111)^C cleaved at the temperature of liquid nitrogen consists of large and atomically smooth terraces and monoatomic steps with height 3.6 $\pm$ 0.2 Å (Fig. 6.1.2 and 6.1.3) and/or of multiple monoatomic heights [I]. Thus, in a good agreement with data for Sb crystallographic structure (d = 3.37 Å), such structure is always formed by cleavage occurring between two planes separated by somewhat large distance.

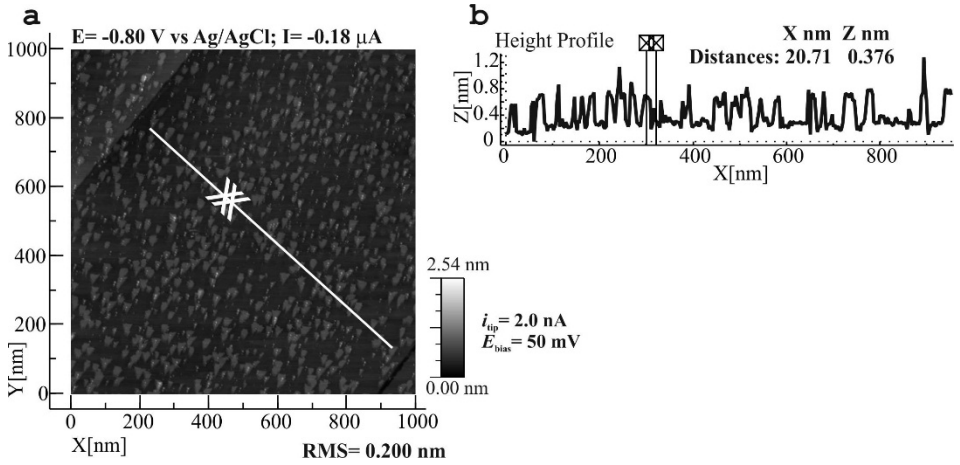

Figure 6.1.2. *in situ* STM image (1000 × 1000 nm) (a) and selected surface profile (b) for cleaved at the temperature of liquid nitrogen Sb(111)^C electrode in 0.5 M Na_2SO_4 + 3.0×10^{-4} M H_2SO_4 aqueous electrolyte, at E = –0.8 V vs. Ag|AgCl, KCl sat. in H_2O.

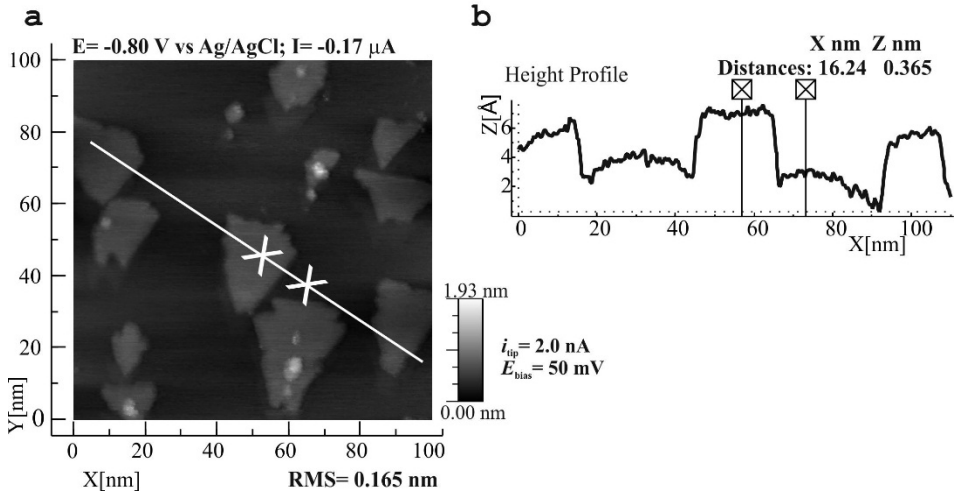

Figure 6.1.3. *in situ* STM image (100 × 100 nm) (a) and selected surface profile (b) for cleaved at the temperature of liquid nitrogen Sb(111)^C electrode in 0.5 M Na_2SO_4 + 3.0×10^{-4} M H_2SO_4 aqueous electrolyte, at E = –0.8 V vs. Ag|AgCl, KCl sat. in H_2O.

Therefore, mainly the van der Waals bonds have been broken and the steps have mainly monoatomic height rather than diatomic, thus, similarly as previously observed for Bi(111) single crystal electrode (Fig. 6.1.4) [29].

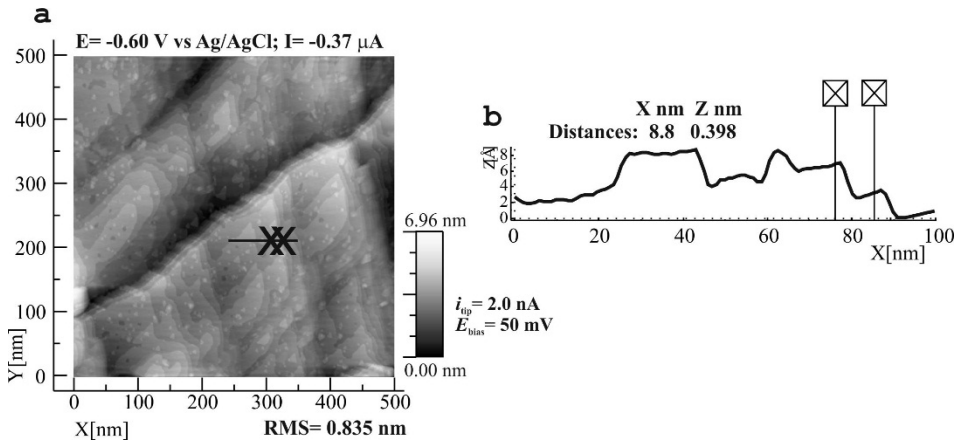

Figure 6.1.4. *in situ* STM image (500 × 500 nm) (a) and selected surface profile (b) for cleaved at the temperature of liquid nitrogen $Bi(111)^C$ electrode in 0.05 M Na_2SO_4 + 2.5×10^{-5} M H_2SO_4 aqueous electrolyte, at E = –0.6 V vs. Ag|AgCl, KCl sat. in H_2O.

The boundaries of the most terraces are close to the straight lines of the atomic rows on the Sb surface along the [1 1 0] direction (Fig. 6.1.2a) [78]. However, there are some areas having considerably curved boundaries and rounded islands of the triangular shape. No random hollows of nanometric dimension are present on $Sb(111)^C$ when compared to Bi(111) [29].

At higher magnifications, some terrace boundaries show considerable dispersion and can deviate from the direction of atomic rows (Fig. 6.1.3). Of course, the behavior of the boundaries depends on their direction and the length and thermal motion is the reason for the more extended boundaries being slightly diffused. However, different behavior of the boundaries can be caused by their various steepnesses on an atomic scale provided by the packing of layers along the [1 1 1] direction [78]. In some places, the dislocation outcrop can be seen and in some surface regions the very small steps with height lower than the lattice period for Sb have been observed, probably caused by the screw dislocations generated during the crystal growth by using the vertical Czochralski method. The data measured in H_2O medium are in a good agreement with the data obtained in UHV STM studies of the $Sb(111)^C$ electrode [30,83] and with previously studied Bi(111) single crystals, where screw dislocation defects were also present, as the same vertical Czochralski method was used for growing of the Bi single crystals [29].

The data in Fig. 6.1.5 show the atomic resolution picture (a) Fourier filtered image (b), the surface profile (c) and typical FFT (Fast Fourier Transform) image (d) for the cleaved $Sb(111)^C$ electrode at E = –0.8 V. According to these data, the quite regular atomic structure can be observed with interatomic distances d = 3.5 ± 0.1 Å. As previously described for Bi(111) electrodes [29], the height fluctuations in the region of (10 × 10) nm^2 on $Sb(111)^C$ surface

analyzed are very small. This regular structure is stable during hours and does not change noticeably under polarization from –0.8 to –0.15 V.

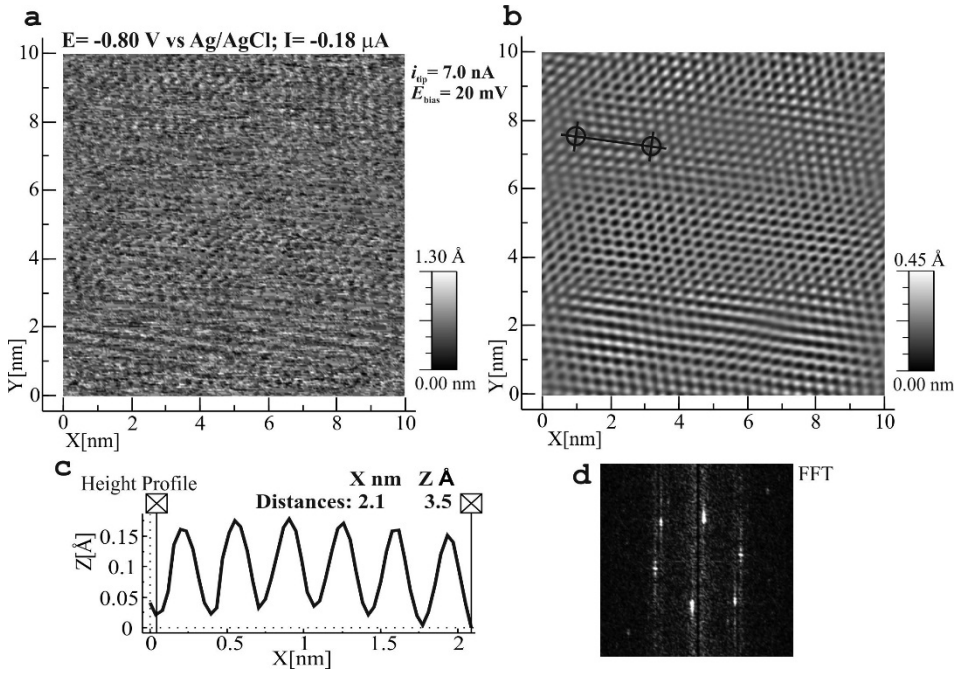

Figure 6.1.5. *in situ* STM image (a), FFT filtered signal (b), height profile (c) and FFT signal probability image (d) for cleaved at the temperature of liquid nitrogen $Sb(111)^{C}$ electrode in 0.5 M Na_2SO_4 + 3.0 × 10^{-4} M H_2SO_4 aqueous electrolyte, at E = –0.8 V vs. Ag|AgCl, KCl sat. in H_2O.

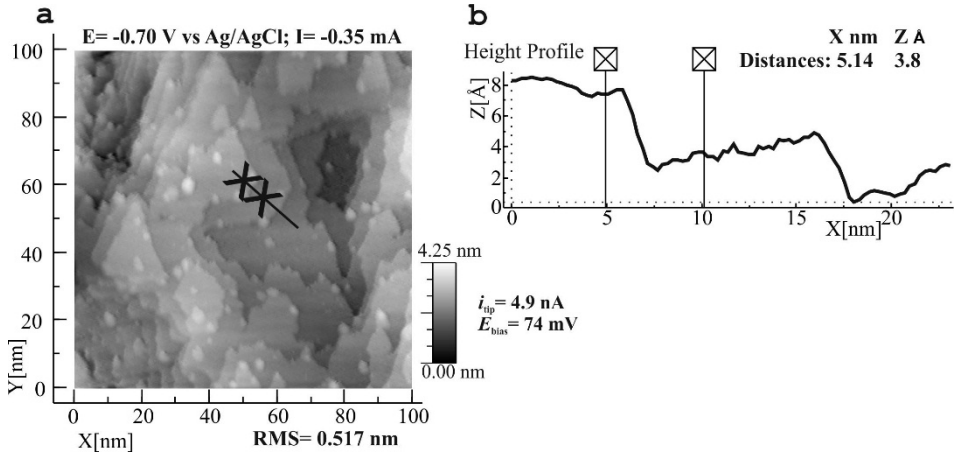

Figure 6.1.6. *in situ* STM image (a) and selected surface profile (b) for electrochemically polished $Sb(111)^{EP}$ electrode in 0.5 M Na_2SO_4 + 3.0 × 10^{-4} M H_2SO_4 aqueous electrolyte at E = –0.7 V vs. Ag|AgCl, KCl sat. in H_2O.

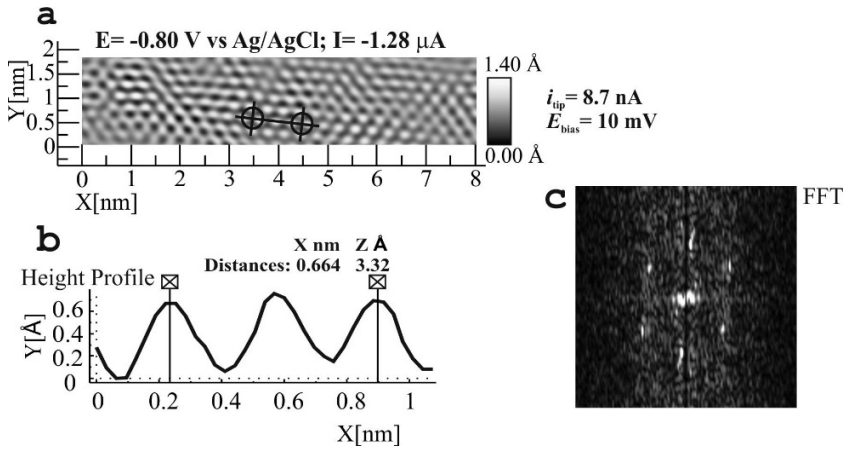

Figure 6.1.7. *in situ* STM image (a), height profile (b) and FFT signal probability image (c) for electrochemically polished Sb(111)^{EP} electrode in 0.5 M Na_2SO_4 + 3.0 × 10^{-4} M H_2SO_4 aqueous electrolyte, at E = –0.8 V vs. Ag|AgCl, KCl sat. in H_2O.

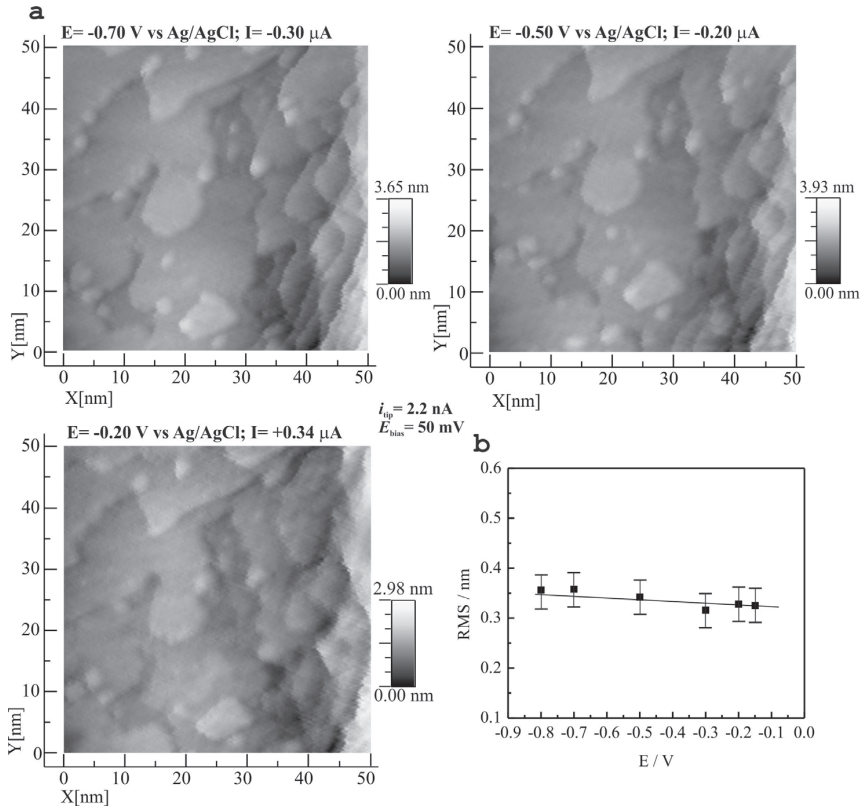

Figure 6.1.8. *in situ* STM images (a), and root mean square roughness (RMS) vs. electrode potential dependence (b) for electrochemically polished Sb(111)^{EP} electrode in 0.5 M Na_2SO_4 + 3.0 × 10^{-4} M H_2SO_4 aqueous electrolyte at various electrode potentials (shown in figure).

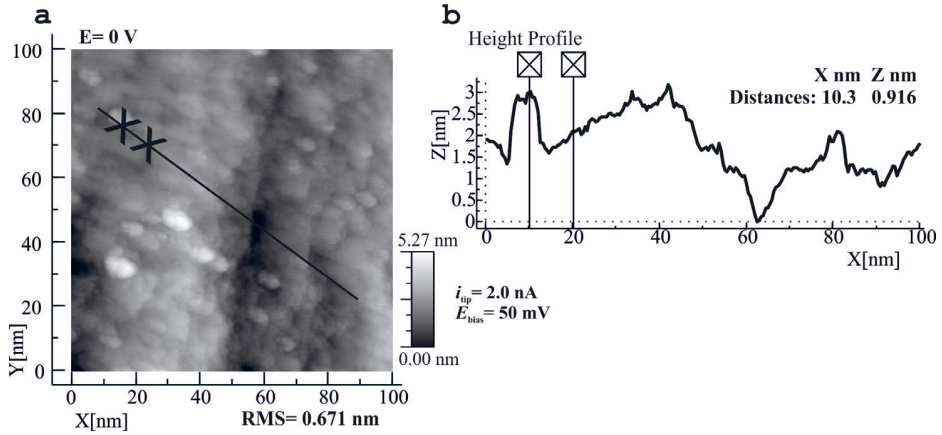

Figure 6.1.9. *in situ* STM image (a) and selected surface profile (b) for electrochemically polished $Sb(111)^{EP}$ plane in 0.5 M Na_2SO_4 + 3.0×10^{-4} M H_2SO_4 aqueous electrolyte, at E = 0 V vs. Ag|AgCl, KCl sat. in H_2O.

According to the data given in Fig. 6.1.6a, the surface of the Sb(111) electrode, electrochemically polished in the saturated KI + HCl aqueous solution at anodic current density j < 1.25 A·cm^2, is quite smooth and only some monoatomic steps and hollows can be observed. The data in the Fig. 6.1.6 show that there are wide areas having atomically smooth structure (ca. 10–20 nm). However, the very small height fluctuations are possible. Fig. 6.1.7 demonstrates the atomic resolution images for the surface of electrochemically polished $Sb(111)^{EP}$. These data are very similar to $Sb(111)^{C}$ and also to Bi(111) studied [29], and thus no noticeable difference in atomic resolution images is observed between electrochemically polished and cleaved single crystal Sb(111) and Bi(111) electrodes.

It is very interesting to mention that the position of the two-dimensional crystal, i.e., the nanometric terraces separated by the steps, is very stable during hours under the cathodic polarization from $-0.8 \leq E \leq -0.15$ V as well as under the various potentials applied during hours (Fig. 6.1.8a). The root mean square roughness (RMS) vs. cathodic polarization dependence data (Fig. 6.1.8b) affirmed this conclusion. Thus, in a good agreement with the cyclic voltammetry and impedance data [84,84,84–90,92,93], there are no quick surface reconstruction processes as it has been established for Au(*hkl*) electrode [59–61].

It is important to note that the surface of $Sb(111)^{C}$ as well as $Sb(111)^{EP}$ electrodes is also stable under cathodic polarization from –0.8 to –0.15 V in more acidic solution (in 0.5 M Na_2SO_4 + 0.003 M H_2SO_4) and there is no influence of E on the surface roughness measured. At less negative potentials, the surface oxidation and dissolution of the surface starts and after holding the $Sb(111)^{C}$ or $Sb(111)^{EP}$ electrodes at E = 0 V during few seconds (Fig. 6.1.9), a very rough (RMS > 0.67 nm) and defect surface structure for Sb(111) has been obtained. This effect is similar for Bi electrodes [29]. Thus, for Sb(111) in more

acidic solutions the potential region from –0.8 to –0.15 V has been investigated and analyzed only.

6.2. (II) Adsorption of thiourea at Bi(111) surface

6.2.1. Analysis of cyclic voltammetry and impedance spectroscopy data

The adsorption process of TU on the electrochemically polished Bi(111)^{EP} plane by using the in situ STM method has been studied [II]. For comparison the cyclic voltammetry and impedance methods were applied and the results were compared with the thermodynamic data obtained for Bi(*hkl*) [152,153], Hg and Pt electrodes [154–156].

Cyclic voltammetry data (Fig. 6.2.1) indicates that there is no linear dependence of TU desorption peak ($E_{peak,des}$) on ν (adsorption step (rate) limited), as well as on $\nu^{-1/2}$ (mass transfer step (rate) limited process) indicating of the mixed adsorption-desorption and mass transfer stages limited TU adsorption process at Bi(111)^{EP} electrode surface. However, the very weak dependence of $E_{peak,des}$ on ν indicates that the desorption step is slow and nearly rate limiting stage for adsorption/desorption of TU at Bi(111) surfaces. Absence of the oxidation peaks at *j*, *E* curves indicate that there is no quick faradic processes within the electrode potentials from –1.2 to –0.6 V (Ag|AgCl KCl sat. in H_2O).

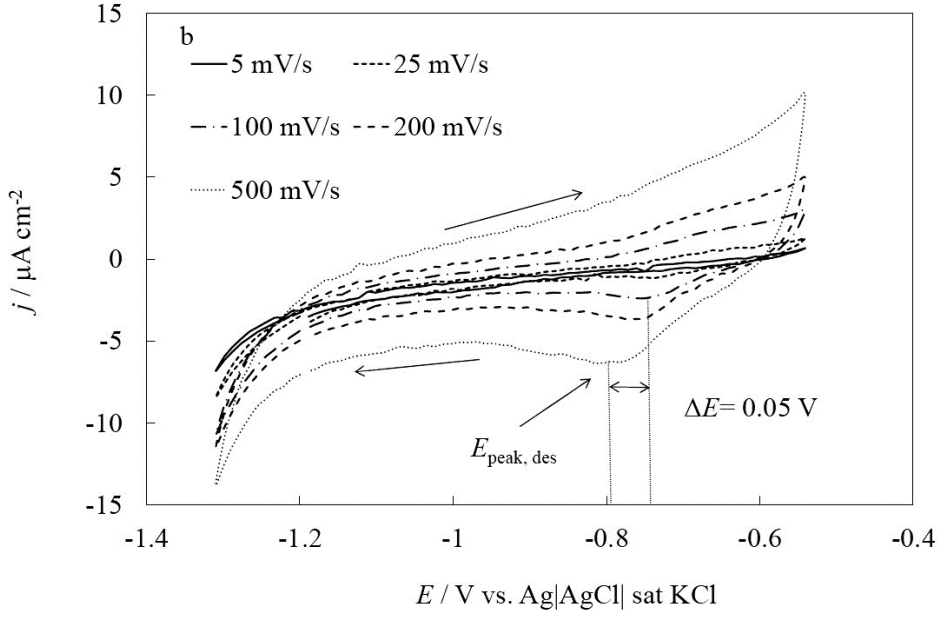

Figure. 6.2.1. Current density (*j*) vs. electrode potential (*E*) curves for Bi(111) electrode in 1 M TU + 0.05 M Na_2SO_4 + 2.5×10^{-5} M H_2SO_4 solutions measured applying different scanning rates, given in figure.

Differential series capacitance (C_s) vs. electrode potential (E) curves obtained at 210 Hz for weakly acidified 0.05 M Na_2SO_4 solution with different additions of TU demonstrated the adsorption of TU (Fig.6.2.2) within the wide electrode potential region in an agreement with CV data (Fig. 6.2.1). It can be seen from Fig. 6.2.2 and inset, that for different TU concentrations from 0.1 mM to 0.1 M, there are increased capacitance values, compared with the base electrolyte curve, which is not typical for the organic molecules adsorption at the metal electrodes [II], [3,115,157]. This unusual dependence of C_s on the TU concentration has been also observed for the mercury and platinum electrodes [154–156]. Parsons et al. [156] explained this effect by the increase of the apparent electrical permittivity of the inner layer region of the electrical double layer (EDL) due to the specific adsorption of TU molecules, having much higher dipole moment than that of the water layer. A capacitance step (hump) appears in the C_s, E curves at E= –0.7 V for 0.1 M TU solution (Fig. 6.2.2), being characteristic of the strongly adsorbed compounds like anions and/or strongly polar organic substances [152,153,156,158–160]. Due to the strong adsorption of anions the hump shifts toward more negative potentials with the increase of TU concentration (at E= –1.2 V for 1.5 M TU solution). The C_s values for more concentrated TU solutions at E= –0.9 V for 1.0 M TU are lower than those for intermediate TU concentrations. The occurrence of the hump results mainly from the changes in the electrostatic interactions between the adsorbed molecules and Bi(111) surface and, thus, it is initiated by changes in the dielectric constant of the inner layer due to the strong, but slow adsorption of TU with the sulfur atom oriented toward the Bi(111) surface [152,153,156].

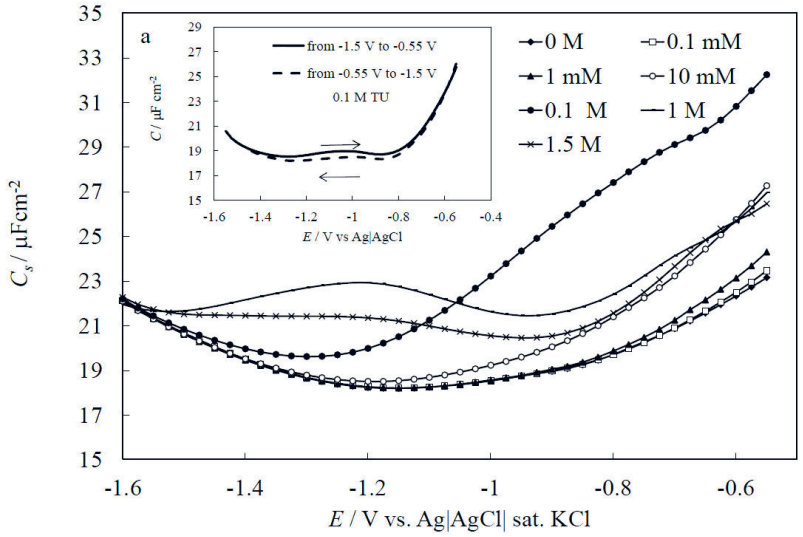

Figure 6.2.2. Differential capacitance (C_s) vs. electrode potential (E) curves for $Bi(111)^{EP}$ electrode in 0.05 M Na_2SO_4 + 2.5 $\times 10^{-5}$ M H_2SO_4 + x M TU solution (f=210 Hz) at different TU concentrations; inset: C_s, E-curves for 0.1 M TU solution for different potential directions.

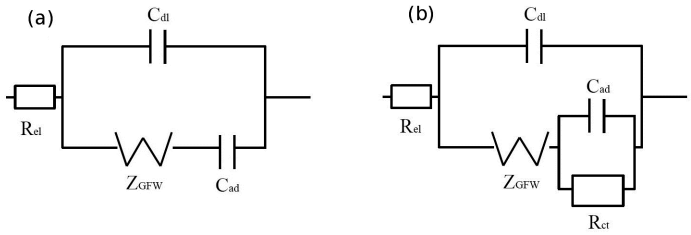

Figure 6.2.3. Equivalent circuits (EC): (a) modified Frumkin-Melik-Gaikazyan EC with generalized finite length Warburg element Z_{GFW}, double layer capacitance C_{dl}, base electrolyte resistance R_{el} and (b) circuit a with extra charge transfer (parallel) resistance, R_{ct}, connected in parallel with adsorption capacitance C_{ad}.

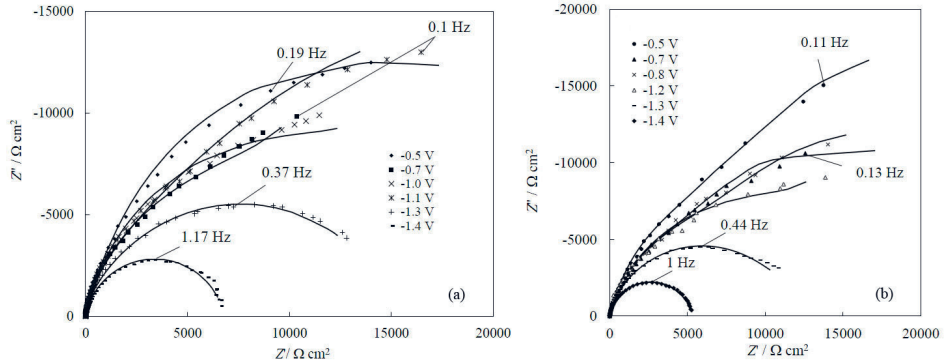

Figure 6.2.4. Z'', Z' – curves (so called Nyquist plots) for Bi(111)^{EP} electrode in 0.05 M Na_2SO_4 + 2.5×10^{-5} M H_2SO_4 electrolyte + 0.01 M TU (a) and 1.5 M TU (b) solution at different electrode potentials, given in figure, (points: experimental data, lines: calculated according to modified Frumkin and Melik-Gaikazyan model, Fig. 6.2.3a).

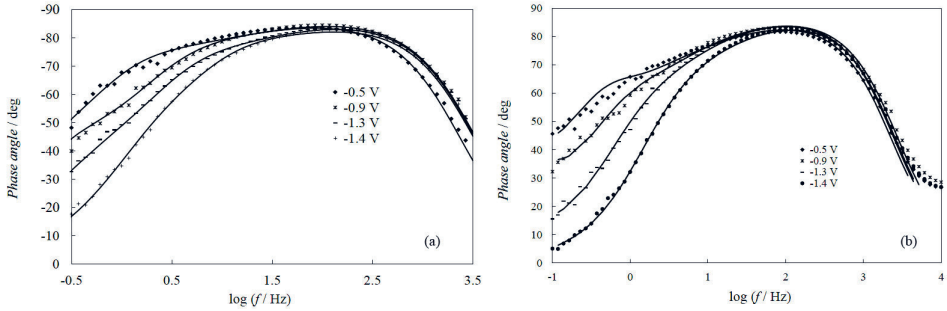

Figure 6.2.5. Phase angle (δ) vs. log f plots for Bi(111)^{EP} electrode | 0.05 M Na_2SO_4 + 2.5×10^{-5} M H_2SO_4 +0.01M TU (a) and + 1.5 M TU (b) solution at different electrode potentials given in figure, (points: experimental data, lines: calculated according to the modified Frumkin and Melik-Gaikazyan circuit, given in Fig. 6.2.3b, with the charge transfer resistance R_{ct} added parallel with adsorption capacitance C_{ad} and generalized diffusion impedance Z_{GWF}).

For intermediate TU concentrations ($c_{TU} \leq 1\times10^{-2}$ M), in the limited region of ac frequencies from 250 to 10 Hz, there is a noticeable dependence of the capacitance on the potential scan direction, i.e., the hysteresis in the C_s, E curves appears (inset in Fig. 6.2.2), indicating the possible strong, so called, specific adsorption (chemisorption) of TU at the Bi(111) surface with the slow partial charge transfer step [81,152,153,157,161,162].

Analysis of the Nyquist- plots (Fig. 6.2.4), and Bode phase angles (δ) vs. log f plots (Fig. 6.2.5), shows that in the region of ac frequency from 500 to 5 Hz, the TU adsorption is limited mainly by the rate of the heterogeneous adsorption step as the δ values are lower than –80° (where $\delta = \arctan(|Z''|/Z'$ and Z'' is the imaginary and Z' is real part of impedance) ($\delta = -90^{o}$ is characteristic for adsorption step limited process and $\delta = -45^{o}$ for semi-infinite diffusion step limited process). At lower ac frequency $f \leq 1$ Hz, there are noticeable differences between the δ values measured at fixed E, indicating that the TU adsorption kinetics depends noticeably on E applied. At higher frequencies ($f >$ 100Hz), the shape of the δ, log f-curves is nearly independent of the electrode potential, if $E \geq -1.2$ V. At $E \leq -1.4$ V, the faradic cathodic hydrogen evolution process prevails at the Bi(111) | TU interface ($\delta \approx 0$, characteristic for faradic charge transfer step) at $E = -1.6$ and at $f < 0.5$ Hz).

According to the experimental data (Fig. 6.2.5), the $|\delta|$ values for the Bi(111) | TU solution interface are maximal at $f \approx 100$ Hz (so-called high frequency (HF) maximal adsorption region). The maximum values of $|\delta|$ are nearly independent of c_{TU} (Fig. 6.2.5). The values of $|\delta|$ higher than 70° at $E > -1.2$ V (Ag|AgCl, KCl sat. in H_2O) indicate that the Bi(111) | 0.05M $Na_2SO_4 + 2.5\times10^{-5}$ M $H_2SO_4 + x$ M TU interface can be simulated as a nearly ideally polarizable system where, however, the deviation toward mixed kinetics (slow adsorption; faradic charge transfer and diffusion steps) is possible at $1 < f < 10$ Hz. At very low frequencies ($f < 0.5$ Hz) and electrode potentials $E > -1.1$V, the $|\delta|$ values are almost 45°, which can be explained by the diffusion-like step limited adsorption process at the Bi(111) electrode [103,107, 110,111,115,157]. It should be noted that at $E \leq -1.4$ V, the region of intensive decrease in $|\delta|$ is shifted toward higher values of f with the increase of negative polarization (Fig. 6.2.5), explained by the quicker faradic cathodic hydrogen evolution process.

Very complicated Nyquist plots have been established for more concentrated TU solutions ($c_{TU} \geq 0.5$ M) at $E = -0.8$ V and $E = -0.7$ V, where the strong blocking adsorption of TU at Bi(111) starts. There are even small steps in Nyquist plots (Fig. 6.2.4b and 6.2.5b), sometimes explained by the so-called anomalous adsorption step limited process, discussed by Compte et al. [163,164] and Bisquert at al. [165,166]. Quite similar deviations from the classical Frumkin and Melik-Gaikazyan model [103] (from the semi-infinite diffusion and adsorption steps limitation toward the generalized finite length diffusion model) has been observed for compounds having very high Gibbs adsorption values (camphor, 2,2'-BP, cyclohexanol) [3,115,118,157]. Thus, the

mixed kinetics (slow adsorption with the partial charge transfer and diffusion-like limited steps) have been established at $E \geq -1.2$ V and at $f < 1.0$ Hz . Within the medium frequency region, ($10 < f < 300$ Hz) the phase angle values lower than −75° (like for uracil adsorption on Bi(*hkl*) [157]), are characteristic for the slow adsorption rate processes with the slight deviation toward the finite-length mass-transfer step.

Thus, according to the analysis of the C_s, E curves (Fig. 6.2.2) and impedance spectra (Figs. 6.2.4, 6.2.5), there is no big hysteresis at higher frequencies ($f > 250$ Hz) for less concentrated TU solutions. Differently from camphor, 2,2'-bipyridine [3] and 4,4'-bipyridine adsorption data [III], the differential capacitance regularly increases at $E > -1.2$ V with the rise of TU concentration in the base electrolyte solution. At c_{TU} higher than 1.0 M, a surface blocking effect by adsorbed TU molecules takes place, visible as a decrease of C_s at fixed $E > -1.1$ V (Fig. 6.2.2a).

6.2.2. Analysis of the *in situ* STM data

The *in situ* STM data, presented in Fig. 6.2.6, show that the surface of the electrochemically polished Bi(111) electrode is very flat and there are only few uplifted triangles with the monoatomic height $z < 0.4$ nm, which is in a good agreement with the crystallographic lattice parameters for Bi(111) plane [3,29,81]. The atomic resolution level surface structure of Bi(111) is very stable within the wide potential region (from −1.0 to −0.3 V vs. Ag|AgCl, KCl sat. in H_2O) in 5×10^{-2} M Na_2SO_4 + 2.5×10^{-5} M H_2SO_4 aqueous solution (Fig. 6.2.6b), as well in time, additionally confirmed by the impedance data [3,29,81, 85,115,157]. The unfiltered experimental data in Fig. 6.2.6b show the good atomic resolution for Bi(111) surface. The few standing out triangles (Fig. 6.2.6a) on Bi(111) surface are formed during the surface preparation process [3,29,81].

Systematic analysis of the *in situ* STM data for TU adsorption (Fig. 6.2.7) shows, that differently from camphor, 2,2'-BP [3] and 4,4'-BP [III] adsorption, the regular homogeneous adsorption layer structure cannot be detected by *in situ* STM method at the Bi(111) | 0.05 M Na_2SO_4 + 2.5×10^{-5} M H_2SO_4 + x M TU solution interface. The surface profiles, given in Fig. 6.2.7b, show that for more concentrated TU solutions $c_{TU} > 1.0$ M, there are only some adsorbed TU molecular agglomerates with the height of $z \geq 6$ Å, adsorbed at the more heat motion screened surface regions, i.e., at the flat Bi(111) surface regions located near the mono- or bilayered uplifted Bi(111) triangles (Fig. 6.2.7a), observed in some places at the atomically flat Bi(111) surface.

For dilute TU solutions $c_{TU} \leq 0.5$M, it was impossible to visualize the adsorbed TU molecular agglomerates at Bi(111) | 0.05 M Na_2SO_4 + 2.5×10^{-5} M H_2SO_4 + x M TU interface. Thus, only for solutions demonstrating the blocking capacitive behavior (c_{TU}>1.0M in Fig. 6.2.2) the adsorption of TU molecules can be visualized *in situ* at Bi(111) surface.

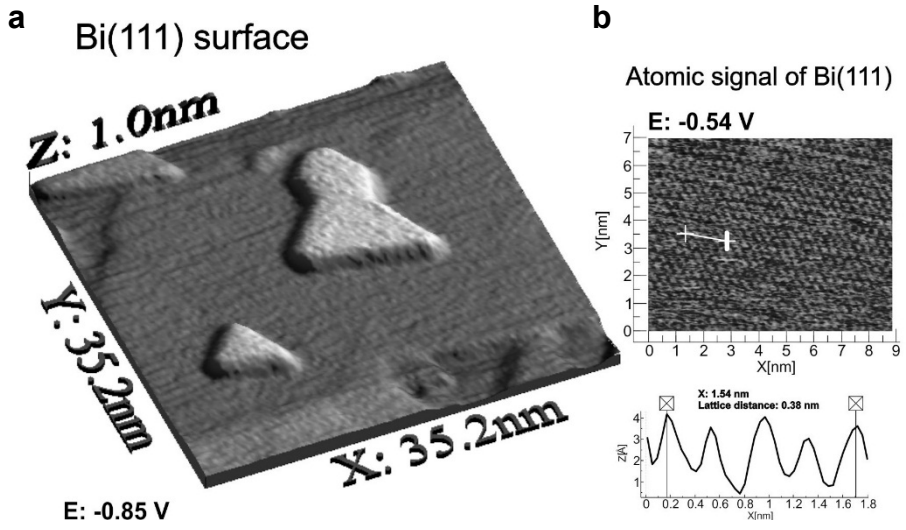

Figure 6.2.6. *in situ* STM images for Bi(111) surface (electrochemically polished) in supporting electrolyte solution (0.05 M Na_2SO_4 + 2.5×10^{-5} M H_2SO_4) (a), unfiltered atomic resolution signal from Bi(111) surface in supporting electrolyte and the selected height profile (b), at E= –0.54V vs. Ag|AgCl, KCl sat. in H_2O.

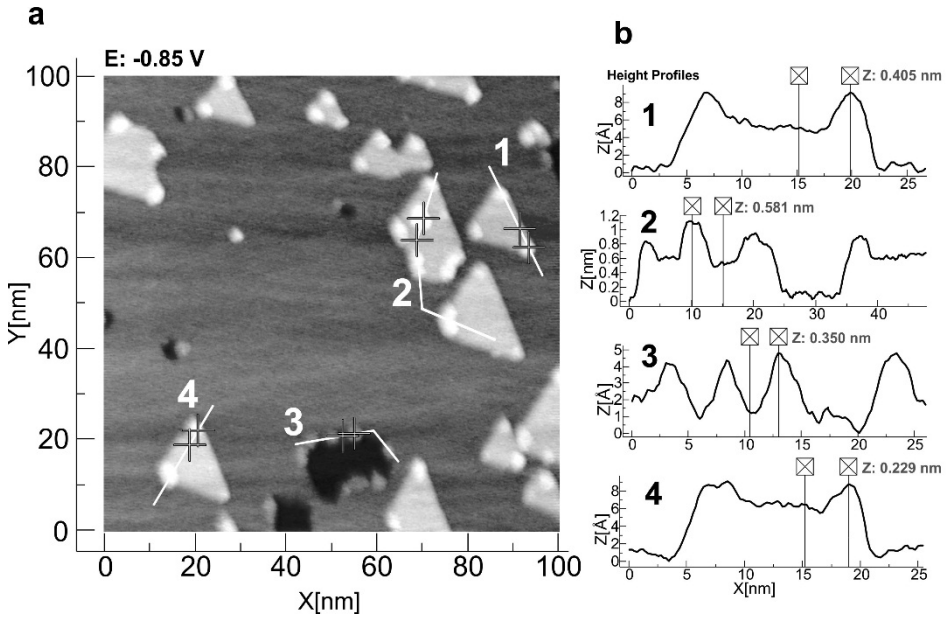

Figure 6.2.7. *in situ* STM image (a) and selected surface profiles of adsorbed thiourea (b) for Bi $(111)^{EP}$ surface in 0.05 M Na_2SO_4 + 2.5×10^{-5} M H_2SO_4 + 1.5 M TU solution, at E= –0.85V vs. Ag|AgCl, KCl sat in H_2O.

In Fig. 6.2.7b some surface profiles are given, demonstrating that the superstructure formed at the monoatomic high Bi triangles varies from 15 to 20 nm wide with the maximal height from 8 to 10 nm. However, the adsorption agglomerates formed at the edge of missing triangles (profile 3 in Fig. 6.2.7b) are less well developed and the medium wideness is only nearly 5 nm. Surprisingly, at the atomically flat surface areas, there are no strongly adsorbed TU molecules that can be visualized using the *in situ* STM method. The low surface concentration (number of TU molecules at 100×100 nm^2 area) and thus, the low Gibbs adsorption (Γ) value, is not surprising as the thermodynamic analysis shows that there is a remarkable repulsion between the adsorbed TU molecules [152,153], and therefore the Γ values are 2–3 times lower than those for camphor or 2,2'-BP molecules ($\Gamma_{max}=8.8\times10^{-10}$ mol·cm^{-2} [3]), having strong attractive interactions between the molecules adsorbed at Bi(111). Thus, only the compounds forming a very compact adsorption layer, initiated by the strong van der Waals attractive interactions, and the formation kinetics of which is mainly limited by the rate of the slow adsorption and partial charge transfer steps (like 2,2'-BP and camphor [3]), can be visualized as a regular 2D layer at the Bi(111) surface, if applying the constant current *in situ* STM method (Fig. 6.2.7).

6.3. (III) Adsorption of 4,4'-bipyridine at Bi(111) surface

6.3.1. Cyclic voltammetry and differential capacity results

It is confirmed that the bismuth single crystal (111) plane is ideally polarizable within the potential region, (E), from −1.6 to −0.55 V (Ag|AgCl, KCl sat. in H_2O) in aqueous 0.5 M Na_2SO_4 + 3.0×10^{-4} M H_2SO_4 solution [115–118,157]. Very flat and regular surface structure is obtained by either electrochemical polishing or cleaving (Fig. 6.3.1) [29].

For solutions with additions of 4,4'-BP from 0.3 to 3 mM, the anodic polarization limit is shifted towards more positive values (E < −0.2 V) due to the blocking adsorption of protonated 4,4'-BP at the Bi(111) plane.

Cyclic voltammetry (CV) data given in Fig. 6.3.2 show that there are two main reduction as well as two main reoxidation processes (or reaction steps) at Bi(111) | 4,4'-BP + Na_2SO_4 + H_2SO_4 interface within the potential region from –1.4 V to –0.6 V. For the 3mM 4,4'-BP solution, the reduction process at more negative potentials (Fig. 6.3.2) is characterized by the reduction peak potential, $E_{red,1}$, shifting toward more negative E values with the rise of potential sweep rate, ν, indicative of the mixed kinetic process within $E_{red,1}$. In the oxidation curve (Fig. 6.3.2a), there is a very small and wide peak at $E_{ox,1}$ = –0.9 V, and $E_{ox,1}$ is practically independent of ν (indicating of adsorption/desorption limited process) [4,10–12,15,33,115–118,157]. At lower 4,4'-BP concentrations, $c_{4,4'\text{-BP}} \leq 0.6$ mM, Fig. 6.3.2b, there is a linear dependence of $E_{red,1}$, (difference between reduction current peak potential, $\Delta E_{red,1}$, is lower than 30mV for one decade of ν) as well

as $E_{ox,1}$ on $\nu^{1/2}$ (Fig. 6.3.2c), indicative of the diffusion limited charge transfer (reduction/reoxidation process) at Bi(111) | 4,4'-BP+H_2SO_4+Na_2SO_4 interface.

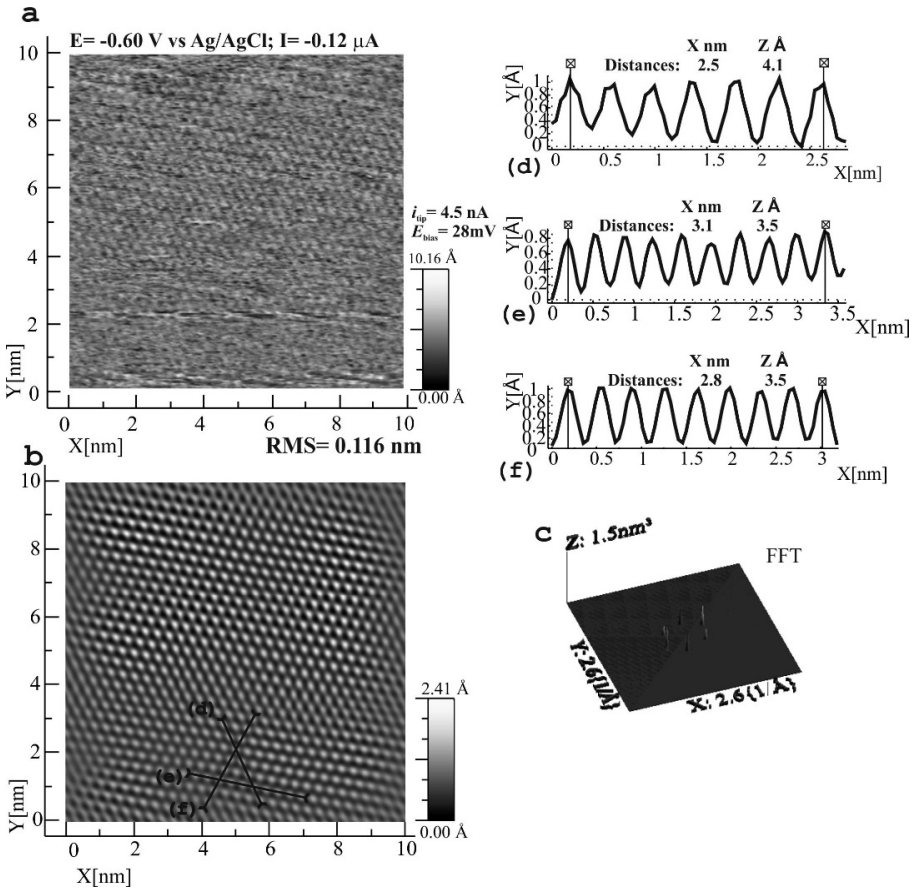

Figure 6.3.1. *in situ* STM images for cleaved Bi(111) electrode in 0.05 M Na_2SO_4 + 2.5×10^{-5} M H_2SO_4 aqueous solution under cathodic polarization (a), FFT filtered image (b), FFT signal probability image (c) and selected height profiles (d, e, f).

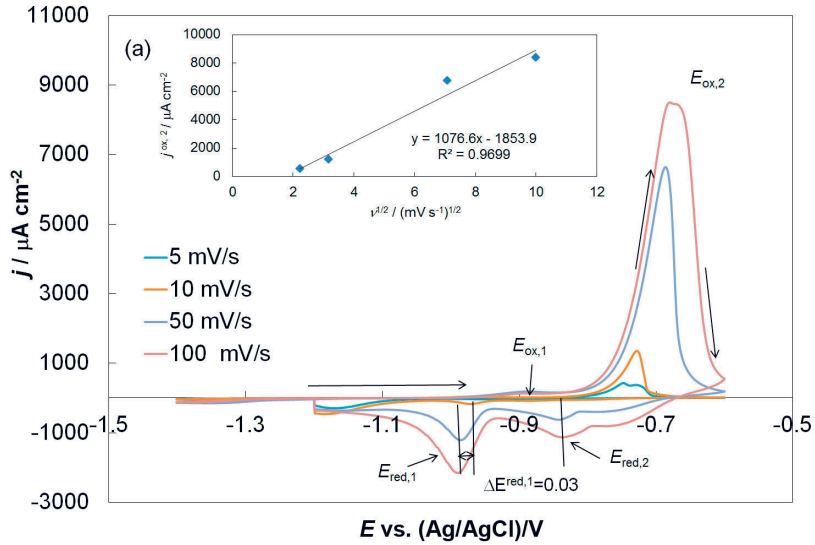

Figure 6.3.2a. Current density (j) vs. potential (E) curves for Bi(111) electrode in 3 mM 4,4'-BP + 0.5 M Na_2SO_4 + 3×10^{-4} M H_2SO_4 solution at different scan rates (ν) (given in figure), inset: $j^{peak,\,2}$ vs. $\nu^{1/2}$ curve.

It is interesting that the slope of the $E_{red,1}$ vs. $\nu^{1/2}$ plot depends on the $c_{4,4'\text{-BP}}$ value, being higher for more concentrated 4,4'-BP solutions (not shown for shortness). Thus, the diffusion coefficient obtained by the slope values slightly depends on the concentration of the organic compound in solution forming the very compact layers at charged interface. Nevertheless, the reduction current controlled process within $E_{red,2}$= –0.85 V seems to be adsorption step limited process, as $E_{red,2}$ is nearly independent of potential scanning rate (Fig. 6.3.2a).

At E > –0.75 V, very high oxidation current densities have been measured (Fig. 6.3.2a) with peak potential $E_{ox,2}$ noticeably shifting toward less negative potentials with the rise of electrode potential scanning rate. The peak potential $E_{ox,2}$ and corresponding current density $j_{ox,2}$ (inset in Fig. 6.3.2a) depend linearly on $\nu^{1/2}$, being characteristic of diffusion limited process.

Data presented in Fig. 6.3.2 indicate that the adsorption/desorption (and oxidation/reduction) are partially irreversible processes if potential cyclation takes place in the wide E region, like –1.4 V < E < –0.6 V.

However, it is interesting, that $E_{red,1}$ and $E_{ox,1}$ are practically independent of number of potential cycle applied. $E_{ox,2}$ shifts toward more negative E values with increase of number of the potential cycles applied indicating to the stronger bonding of intermediates formed at Bi(111) electrode surface at $E \leq$ –1.1 V. Thus, probably blocking adsorption of reaction intermediates takes place if E = –1.4 V has been applied, being the cathodic limit of potential cyclation in this work.

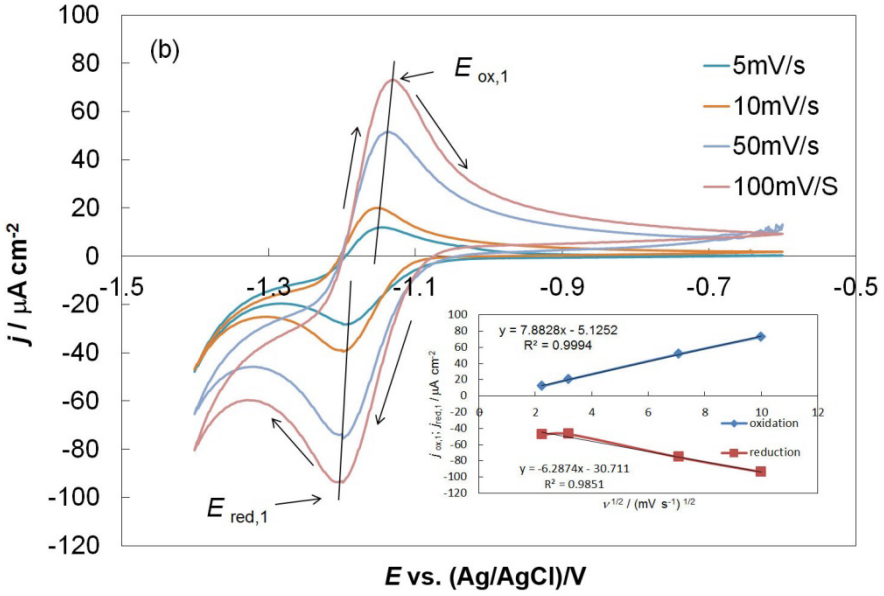

Figure 6.3.2b. *j* vs. *E*-curves for 0.06 mM 4,4'-BP + 0.5 M Na_2SO_4 + 3×10^{-4} M H_2SO_4 solution at different scan rates (given in figure) for Bi(111) electrode.

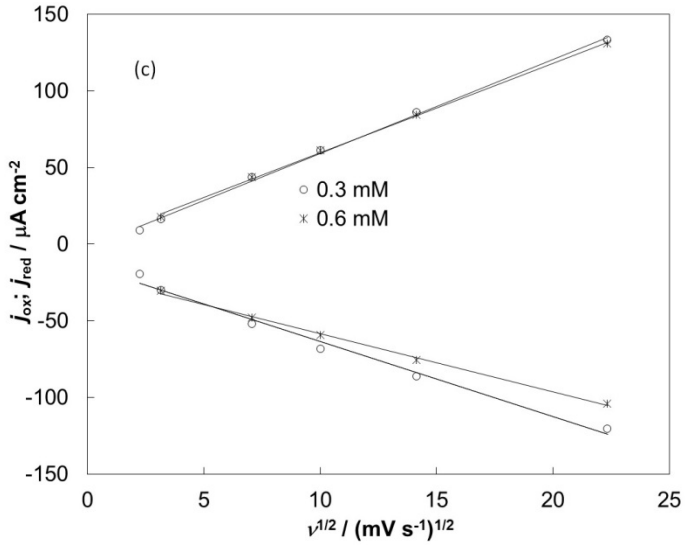

Figure 6.3.2c. E_{ox} and E_{red} potential vs. $\nu^{1/2}$ plots for different 4,4'-BP concentrations (given in figure) for Bi(111) electrode.

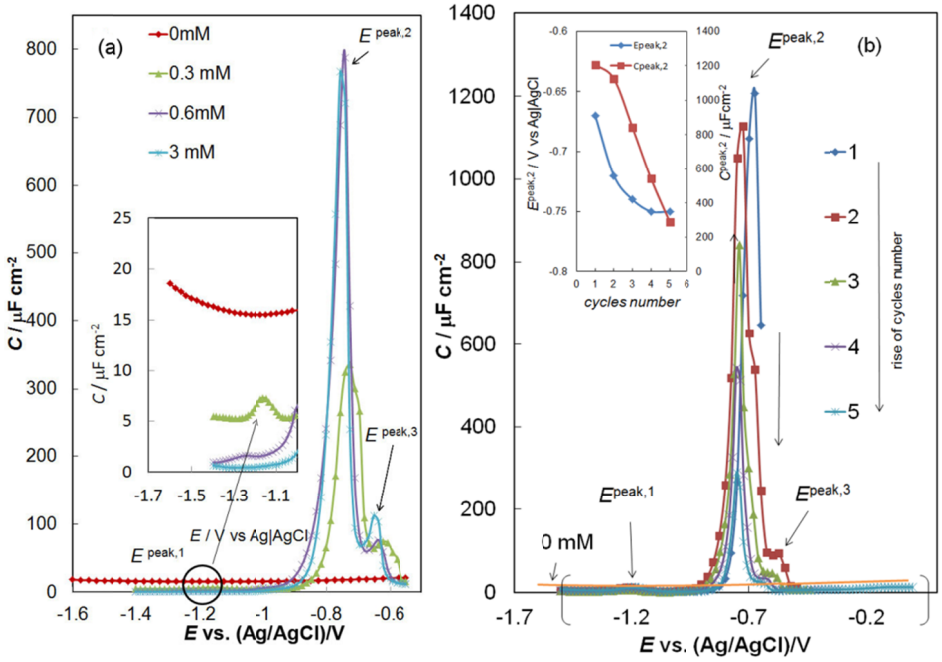

Figure 6.3.3 (a) Differential capacitance (C) vs. electrode potential (E) curves for Bi(111) electrode for x M 4,4'-BP adsorption from base electrolyte solution (0.5 M Na_2SO_4 + 3×10^{-4} M H_2SO_4) at f=210 Hz. Concentration of 4,4'-BP is given in figure. **(b)** C vs. E curves for Bi(111) | 3 mM 4,4'-BP + 0.5 M Na_2SO_4 + 3×10^{-4} M H_2SO_4 solution interface, for 5 successive cycles, measured at f=210 Hz.

Similarly to the CV data discussed, we can see a small cathodic capacitance peak with the peak potential $E^{peak,1}$= –1.2 V (Fig. 6.3.3a) and the second very big capacitance peak $E^{peak,2}$= –0.75 V. In addition to these two peaks, at potentials comparable with zero charge potential, $E_{q=0}$, there is a small third so-called prepeak with the peak potential at $E^{peak,3}$ = –0.65 V (i.e., in the region of $E_{q=0}$). Between these capacitance peaks the capacitance values are lower than that for surface-inactive 0.5 M Na_2SO_4 + 3×10^{-4} M H_2SO_4 solution indicating that the adsorption of 4,4'-BP takes place.

The capacitance C values within the area of first cathodic peak $E^{peak,1}$= –1.2 V for dilute 4,4'-BP solutions are higher than for the more concentrated 4,4'-BP solutions (Fig. 6.3.3a), which is explained by the reorientation of 4,4'-BP molecules with the increase of Gibbs adsorption values with the rise of $c_{4,4'\text{-BP}}$. The reorientation effect is usually more visible for dilute organic compound solution [4,5,15,34]. Potential of the more cathodic capacitance peak $E^{peak,\ 1}$ shifts toward less negative potential values for more concentrated 4,4'-BP solutions (–1.3V < $E^{peak,1}$ < –1.1V). Data in Fig. 6.3.3a show that there is only weakly observable hump in C, E-curve, if more higher concentrations $c_{4,4'\text{-BP}} \geq 0.6$ mM have been studied.

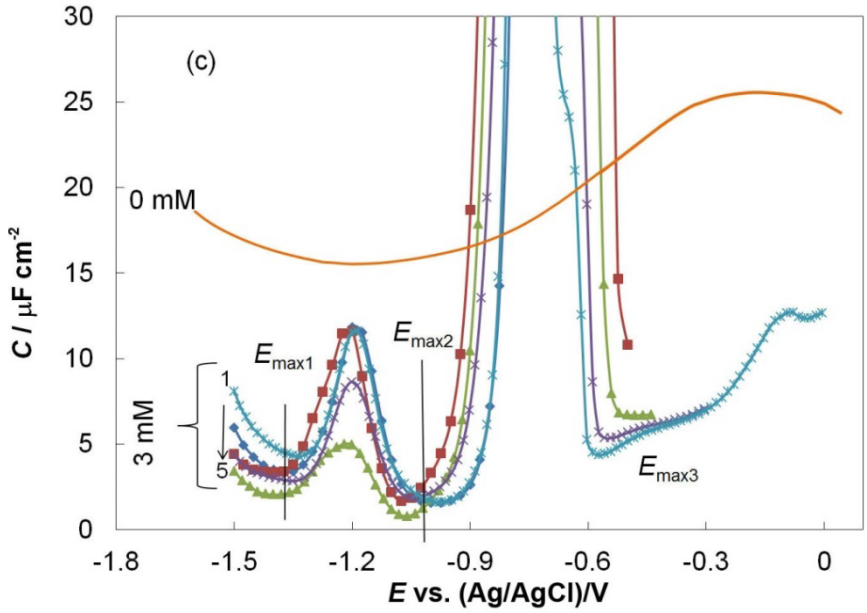

Figure 6.3.3c. Enlargement from figure 6.3.3b: C vs. E curves for Bi(111) | 3 mM 4,4'-BP+ 0.5 M Na_2SO_4 + 3×10^{-4} M H_2SO_4 solution interface, for 5 successive cycles, measured at f=210 Hz.

The limiting differential capacitance C values for negatively charged Bi(111) electrode surface (at $E < -1.2$ V) decrease with the rise of $c_{4,4'\text{-BP}}$ and, thus, the effective thickness of adsorption layer d_{dl} increases with $c_{4,4'\text{-BP}}$, according to the Helmholz equation for the inner part of electrical double layer, approximated by the plate capacitor equation,

$$C=\varepsilon_0\varepsilon_{eff}/d_{dl} \tag{6.2}$$

where ε_0 is the vacuum dielectric constant, ε_{eff} is the macroscopic dielectric constant of the electrolyte and/or adsorption layer (if the adsorption takes place), d_{dl} is the effective thickness of the double layer (or of the adsorption layer) [10–12,115–118,157,167].

After shifting electrode potential toward less negative values at sufficiently high concentrations, $c_{4,4'\text{-BP}} > 0.3$ mM, the formation of two distinctive different differential capacitance peaks in C, E-curves at $E^{peak,2} \leq -0.7$ V and $E^{peak,3} \geq -0.7$ V can be seen (Fig. 6.3.3a). Very high $E^{peak,2}$, visible at $E= -0.75$ V is increasing with the rise of 4,4'-BP concentration in surface-inactive electrolyte, explained by the reversible oxidation (positive scan direction) or reduction (negative potential direction of cyclation) process of 4,4'-BP at the Bi(111) surface, also seen in the j, E-curve in Fig. 6.3.2a.

The remarkable changes in C, E-curves, where capacitance C decreases at $E^{peak,1}$ as well as at $E^{peak,2}$, appears after cycling the electrode potential within the very wide potential region from –1.6 to –0.3 V (Fig. 6.3.3b and c) for several cycles. The inset in Fig. 6.3.3b shows that the capacitance peak at $E^{peak,2}$ shifts toward less positive potentials and the capacitance values decrease noticeably. It is important to note, that in the case of more concentrated 4,4'-BP solutions (3mM) the C, E-curves were measured within potential region $-1.5\ V < E < 0\ V$ (Fig. 6.3.3c). The wide potential range was possible due to the strong adsorption of 4,4'-BP at Bi(111), thus, blocking the anodic dissolution of Bi(111) electrode surface.

From the Fig. 6.3.3c, it could be seen, that 4,4'-BP is forming three specific maximal adsorption areas at $E \leq -1.2$ V ($E_{max,1} \leq -1.2$ V), at $E_{max,2}$ near $E = -1.1$ V and at $E_{max,3} \geq -0.6$ V. In the area of $E_{max,3}$, the C values are decreasing and are much lower than for pure electrolyte solution, indicating the formation of very compact adsorption layer of 4,4'-BP on the Bi(111), which was detectable with the SEIRAS and *in situ* STM method. So, it can be concluded that with the increase of 4,4'-BP concentration, the capacitance within the adsorption-desorption peak $E^{peak,2}$ and $E^{peak,3}$ region for Bi(111) | 4,4'-BP interface increases. Quite low capacitance values $C \leq 10\ \mu F \cdot cm^{-2}$ can be seen in Fig. 6.3.3c at $E < -1.3$ V, within so called first adsorption region with maximal adsorption potential $E_{max,1}$ (Fig. 6.3.3c), corresponding to the very dense 2D organized adsorption layers with the very low ε_{eff} and/or high d_{dl} values. At $E > -1.0$ V, the second capacitance depression area can be seen with potential named as the second potential of maximal adsorption, $E_{max,2}$ (Fig. 6.3.3c). The more negative values of $E_{max,1}$ and $E_{max,2}$ compared with the zero charge potential for the Bi(*hkl*) planes indicate that the limiting adsorption potential shift E_N is slightly negative due to the adsorption of protonated 4,4'-BP at Bi(111) (caused by the replacement of the solvent H_2O monolayer by the adsorbate molecules). However, it should be noted that in the region of $E_{max,2}$, as well as $E_{max,1}$, no *in situ* STM and SEIRAS spectra, demonstrating adsorption of 4,4'-BP, were possible to measure due to the reversibility and pure physical adsorption of 4,4'-BP at Bi(111).

6.3.2. Analysis of the *in situ* STM data

It has been established that in 0.5 M Na_2SO_4 and at electrode potential $E = -0.6$ V (vs. Ag|AgCl, KCl sat. in H_2O) 4,4'-BP forms a stripe pattern on Bi(111) (Fig. 6.3.4) [III].

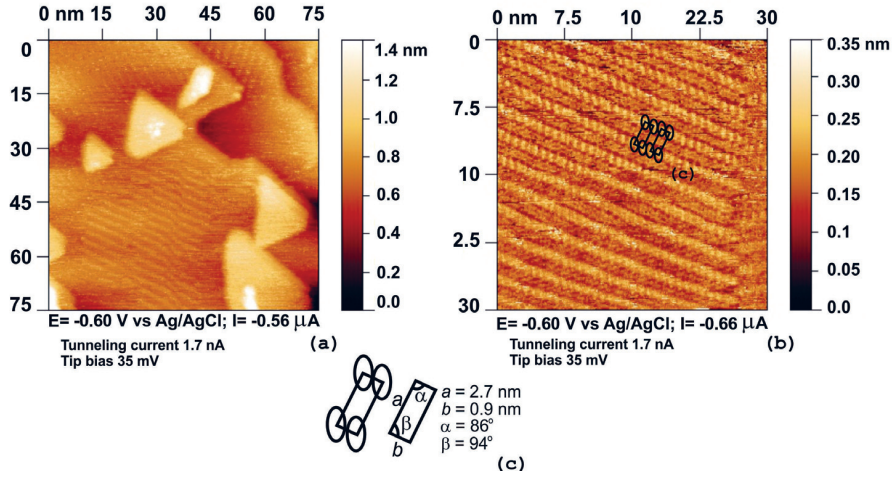

Figure 6.3.4. Unfiltered *in situ* STM images for the 4,4'-BP adsorption on Bi(111) from 0.5 M Na_2SO_4 + 3×10^{-4} M H_2SO_4 aqueous electrolyte (a and b), proposed packing model for 4,4'-BP molecules and calculated unit cell dimensions (c).

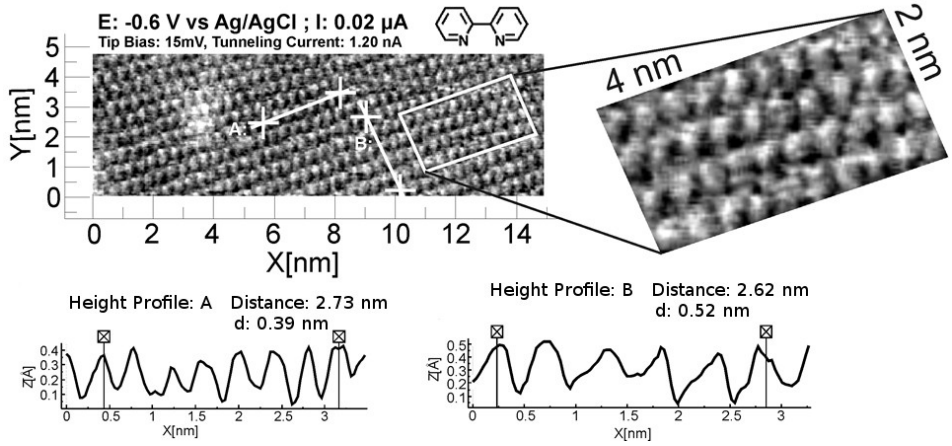

Figure 6.3.5. Unfiltered *in situ* STM images for the 2,2'-BP adsorption on Bi(111) from 0.5 M Na_2SO_4 + 3.0×10^{-3} M H_2SO_4 aqueous electrolyte.

Similar patterns have been observed for the 4,4'-BP adsorption at the Au(*hkl*), Ag(*hkl*) and Cu(*hkl*) electrodes [5,6,33,34,96], where the commensurate structures of the 4,4'-BP molecules are formed by translation and rotation of the molecules relative to the surface [5,34]. It should be noted, that for dilute 4,4'-BP solutions $c_{4,4'\text{-BP}} < 3$ mM, it was impossible to visualize the adsorbed 4,4'-BP molecular patterns at Bi(111) | x Na_2SO_4 + 3×10^{-4} M H_2SO_4 + y M 4,4'-BP interface. Thus, only for solutions demonstrating the strong blocking capacitive behavior the adsorbed of 4,4'-BP molecules can be visualized *in situ* at Bi(111) surface.

In high-resolution *in situ* STM images of the 4,4'-BP adsorption (Fig. 6.3.4) a periodic array of bright features (for 75 × 75 nm and 30 × 30 nm images) is clearly visible at tip bias voltage E_{bias} = 35 mV and at tunneling current 1.7 nA. The characteristic dimensions for the repeating unit cell established are: a = 2.7 nm and b = 0.9 nm (Figs. 6.3.4 (b) and (c)). Taking into account the difference between the values of coordinates a, b, and angles α, β, we proposed that this deformed rectangular unit cell structure of the adsorption layer is probably caused by the coadsorbed 4,4'-bipyridine-sulfate adlayer at the Bi(111) | 4,4'-BP + 0.5 M Na_2SO_4 interface. Wide spaces between the molecule rows have been observed because in the *in situ* STM images only specifically adsorbed 4,4'-BP molecules are visible. We suppose that the wide spaces between the molecular rows are filled by mobile water molecules forming a solvation shell between the Bi(111) surface and sulfate ions, which are electrostatically attracted to the protonated 4,4'-BP molecules.

However, this electrostatic interaction is obviously absent in case of the 2,2'-BP adsorption at Bi(111) [3]. The compact adsorption layer structure is very well detectable by *in situ* STM technique in the region of maximal adsorption for 2,2'-BP from –0.6 to –0.4V versus Ag|AgCl, KCl sat. in H_2O (Fig. 6.3.5). This is mainly caused by the comparatively strong interaction of nitrogen atoms (electron pairs at nitrogen) with Bi surface layer atoms and corresponding high negative Gibbs adsorption energy value ($\Delta\Gamma^0_A$= –29.8 kJmol^{-1}) obtained using Frumkin adsorption isotherm. The adsorption layer structure of 2,2'-BP on Bi(111) surface is stable until to the oxidation and dissolution of Bi(111) at $E \geq$ –0.25V. The main difference observed here is the adsorbed layer structure, where 2,2'-BP are closely packed to each other, there are no empty rows between the stripes of the adsorbed molecules as observed in the case of 4,4'-BP molecules adsorption at Bi(111) surface. This difference is probably caused by the different nitrogen atom position in 2,2'-BP and 4,4'-BP molecules, where lone electron pairs on N atoms at the ends of the molecules have more repulsive action toward neighboring molecule perpendicular to it.

Differently from the data for more concentrated Na_2SO_4 solution (0.5 M), for ten times more dilute Na_2SO_4 solution (0.05 M) the adsorbed 4,4'-BP forms even less compact pattern, but they are still organized into rows, as shown in Fig. 6.3.6. A periodic array of adsorbed species is clearly visible at tip bias voltage E_{bias} = 50 mV and at tunneling current 2.0 nA for the 4,4'-BP adsorption demonstrated in both large and small scale images, given in Fig. 6.3.6 (a) and (b). The characteristic dimensions obtained for the repeating unit cell are: a = 2.6 nm and b = 1.5 nm (Fig. 6.3.6 (c)). The adsorbed species observed by *in situ* STM in less concentrated Na_2SO_4 supporting electrolyte (Fig. 6.3.6 (b)) are separated from each other not only between rows, as it is observed in Fig. 6.3.4 (b), but in both spatial directions.

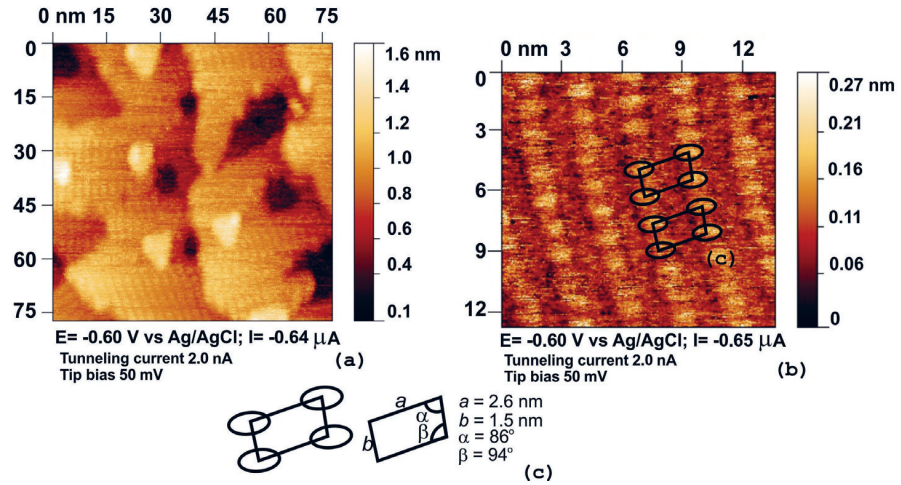

Figure 6.3.6. Unfiltered *in situ* STM images for 4,4'-BP adsorption on Bi(111) from 0.05 M Na_2SO_4 + 3×10^{-4} M H_2SO_4 aqueous electrolyte (a and b), proposed packing model for 4,4'-BP molecules and calculated unit cell dimensions (c).

This effect can be explained by the sulfate coadsorption at Bi(111) at $E > -0.5$V, previously reported for camphor and 2,2'-bipyridine molecules adsorption at Bi(111) [3]. In terms of visible rectangular unit cell and parameters calculated, the structure of the adsorption layers (Fig. 6.3.4 (b) and Fig. 6.3.6 (b)) is clearly influenced by the concentration of the sulfate ions in the supporting electrolyte solution as well as by the repulsions between protonated nitrogen atoms in neighboring 4,4'-BP molecules. Thus, at higher concentration of sulfate anions at the interface, the excess of positive charge on the adsorbed and protonated 4,4'-BP molecules is screened by the counter-charge of the SO_4^{2-} anions. That allows more 4,4'-BP to be adsorbed at Bi(111) surface from more concentrated sodium sulfate electrolyte (Fig. 6.3.4 (b)) than from the less concentrated sodium sulfate electrolyte (Fig. 6.3.6 (b)), where the repulsive forces acting between the protonated 4,4'-BP molecules prevail, therefore, the less compact adsorbed layer is observed.

Formation of the compact adsorbed layer structures at Bi(111), detectable by *in situ* STM method takes place only within the limited region of potentials from –0.7 to –0.5 V. In both electrolyte solutions, the adlayers of 4,4'-BP at Bi(111), visible in the *in situ* STM mode appear only upon a potential excursion towards more positive potentials than $E > -0.7$ V, Fig. 6.3.7. Thus, very close to the zero charge potential ($E_{q=0} = -0.6$ V), where the weak physical adsorption of 4,4'-BP occurs on the atomically flat surface areas of Bi(111) plane (Figs. 6.3.4 and 6.3.6). Compact 4,4'-BP monolayer dissolves when potential is swept from $E = -0.7$ V to more negative values, $E < -0.8$ V. At $E > -0.5$ V, there is no compact adsorption layer visible using the *in situ* STM data in Fig. 6.3.7. No structural changes were observed in the adsorbed layer while cycling the

electrode potential during a long time within $-0.7 < E < -0.5$ V, where the 4,4'-BP adsorption takes place. At $E \leq -0.8$ V and $E > -0.5$ V, the atomic resolution level picture, characteristic of the Bi(111) | inactive supporting $Na_2SO_4 + H_2SO_4$ electrolyte interface was observed [29].

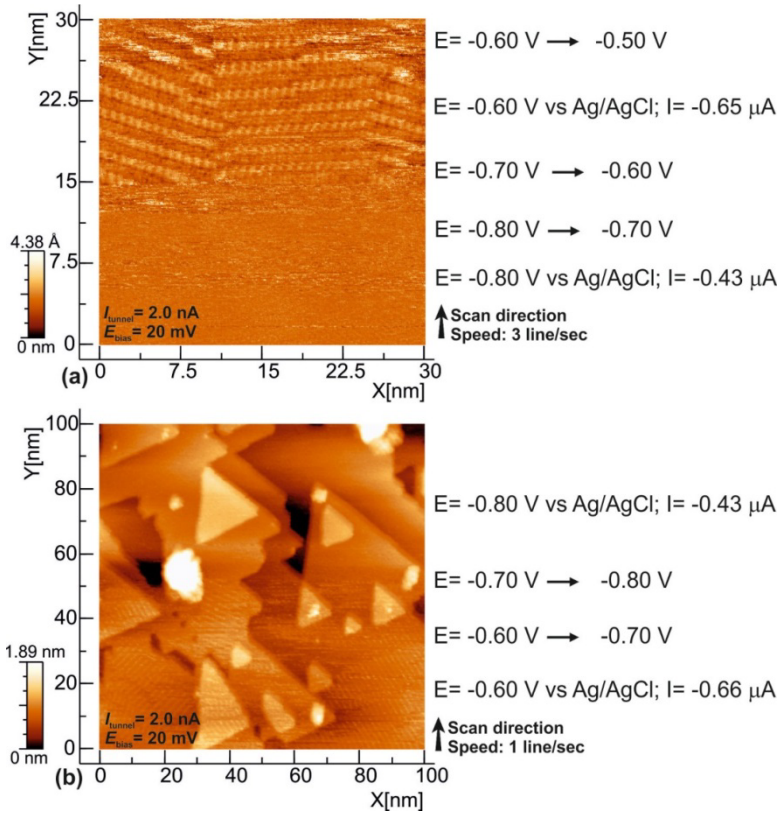

Figure 6.3.7. Unfiltered *in situ* STM images of the creation (a) and the disappearance (b) of the adsorbed 4,4'-BP layer at Bi(111), while changing electrode polarization in 0.5 M Na_2SO_4 + 3.0×10^{-4} M H_2SO_4 aqueous electrolyte.

6.3.3. Analysis of surface enhanced infrared reflection absorption spectroscopy (SEIRAS) data

It was found that the nanocrystalline semimetallic bismuth film has strong infrared enhancement effect [143], where the p-polarized IR peaks have positive direction, indicating the applicability of this measurement method for the interpretation of the composition as well as orientation of adsorbed compounds on bismuth electrode. The data given in Ref. [142] indicate that the chemically deposited Bi film has a preferred (111) orientation, which gives a good correlation with the CV, differential capacitance and *in situ* STM data measured at a single crystal Bi(111) electrode.

The SEIRAS spectra have been measured at different fixed electrode potentials and divided by the spectra measured at the reference electrode potential E= –0.45 V, because at the electrode potentials $E \geq$ –0.45 V (Ag|AgCl KCl sat. in H_2O), the signal, characteristic to the 2D structure of adsorbed 4,4'-BP, disappears. Fig. 6.3.8 demonstrates that the shape of SEIRAS spectra depends on the difference of the electrode potential applied. Thus, the replacement of adsorbed 4,4'-BP organic layer with water and solvated base electrolyte SO_4^{2-} (HSO_4^-) ions takes place. The positive peak at 1027 cm^{-1} for the spectra measured at –0.1 V, probably indicates to the adsorption of small amount of HSO_4^- ions.

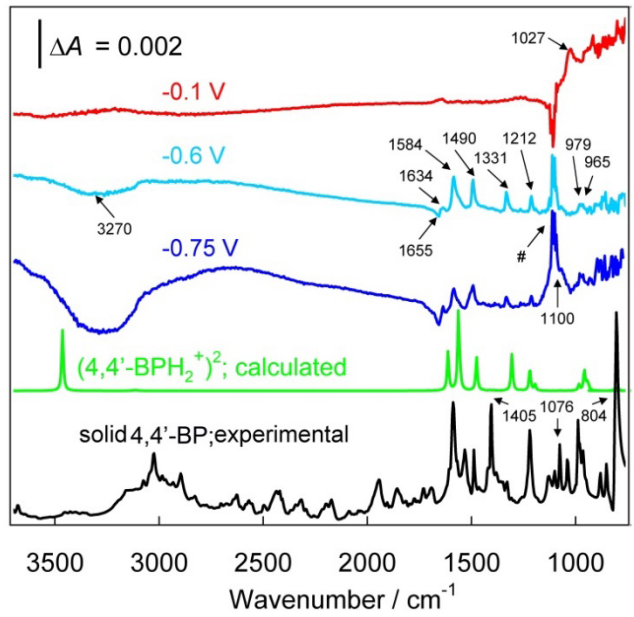

Figure 6.3.8. SEIRAS spectra for Bi film electrode in 3 mM 4,4'-BP + 3×10^{-4} M H_2SO_4 + 0.5 M Na_2SO_4 aqueous solution at different electrode potentials (background spectra was taken at E= –0.45 V). The infrared spectrum of solid 4,4'-BP was measured with ATR technique. The theoretical spectrum of $(4,4BPH_2+)_2$ dimer was calculated using DFT method. # marks the noise caused by the silicon IR absorption band.

Based on the analysis of SEIRAS spectra for 0.5 M Na_2SO_4 + 3×10^{-4} M H_2SO_4+ 3mM 4,4'-BP | Bi(111) interface (Fig. 6.2.8), it can be concluded that the most compact organic layer has been detected at –0.6 V, within the so-called third adsorption region (based on C,E-curves data discussed before), giving positive peaks at 1634, 1584, 1490, 1331, 1212, 979, and 965 cm^{-1}, and negative peaks at 1655 and 3270 cm^{-1}. Negative peaks in the SEIRAS spectra at 1655 and 3270 cm^{-1} correspond to the water desorption from the Bi(111) electrode surface by compactly adsorbed organic compound layer, squeezing out the H_2O molecules [29,115–118,157,167]. The positive peaks at 1634, 1584,

1490, 1331, 1212, 979, and 965 cm^{-1} indicate to the increasing Gibbs adsorption of an organic compound at Bi electrode compared with that at E= –0.45 V.

To analyze the probable composition of the adsorbed organic layer formed, DFT calculations were carried out for the spectra of possible products – measured bands were assigned to certain vibrations of charged or/and neutral bipyridine molecules and various combinations of ions/molecules, respectively, at DFT/B3LYP level of theory. As a result it was found that the calculated spectra for $(4,4'\text{-}BPH_2^+)_2$ (dimer of two radical-cations) has a perfect match with the spectra measured within E from –0.6 V to –0.45 V. The peaks for the calculated compound (multiplied by 0.96, which is a common practice) at 1613, 1563, 1475, 1306, 1219, 983, and 956 cm^{-1} are all within 25 cm^{-1} error region (i.e., only slightly shifted) from the experimental infrared peaks, indicating that the adsorbed organic layer on Bi surface is formed from stacked $4,4'\text{-}BPH_2^+$ radical-cations.

The only missing peak at 3464 cm^{-1} in the calculated spectra compared with experimental spectra at E= –0.6 V indicates the perpendicular orientation of the $4,4'\text{-}BPH_2^+$ radicals with N–H bonds parallel to the surface (only the vibrations perpendicular to the surface should be visible in the spectrum, because the p-polarization (single component) was used). Thus, all the experimentally detected bands are caused, according to DFT calculations, by the vibrations of dipoles oriented perpendicularly to the Bi electrode surface.

The absence of experimental bands at 1405, 1076, and 804 cm^{-1}, present in the ATR (attenuated total reflection) spectrum measured for solid 4,4'-BP (Fig. 6.3.8), indicate to the absence of neutral 4,4'-BP molecules on the Bi surface within electrode potential region from –0.6 to –0.75 V.

The peak visible at 1100 cm^{-1} is initiated by the adsorption of solvated SO_4^{2-} ions, but it is somewhat distorted by the noise. Due to the naturally high intensity of the IR band of sulfate ion, it may be concluded that the medium positive 1100 cm^{-1} peak indicates the presence of noticeable amount of solvated SO_4^{2-} ions, but there is no compact layer of solvate-free SO_4^{2-} or HSO_4^- ions adsorbed between the adsorbed $(4,4'\text{-}BPH_2^+)_n$ clusters forming the rows at Bi surface. Probably most of SO_4^{2-} ions are at least a few nm away from the surface (due to the thick water solvation layer around the ion and fast adsorption-desorption process), which is out of the range of SEIRAS enhancement effect.

The $(4,4'\text{-}BPH_2^+)_n$ adsorption layer at Bi(111) has nearly the same structure within the potential region from –0.6 to –0.75 V (Fig. 6.3.8), but at E < –0.75 V, in some electrode regions this layer probably dissolves, thus, giving a weaker IR-spectrum at E = –0.75 V.

However, it should be noted that it is not possible to measure the SEIRAS infrared spectra at E < –0.9 V correctly due to the slow hydrogen evolution (bubbles formation) reaction.

6.3.4. Theoretical modeling of the Bi(111) | 4,4'-BP interface

Fig. 6.3.9 shows the most favorable positions for three different orientations for adsorbed single 4,4'-BP molecule at the Bi(111) surface: with aromatic rings parallel (A) and perpendicular to the surface plane (B), and with N-atom pointing towards the Bi surface (C). Potential energy curves (ΔE_{int} versus distance from the N-atom in 4,4'-bipyridine to the surface plane) are presented in Fig. 6.3.10 for these three different orientations at the most and the least energetically favorable positions.

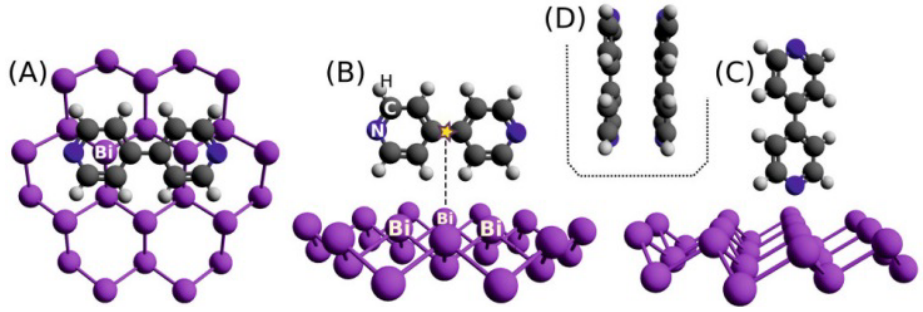

Figure 6.3.9. Models of adsorbed 4,4'-BP molecule orientation at Bi(111) surface (A, B, C), and the 4,4'-BP dimer model (D).

The interaction strength is determined by the magnitude of specific adsorption interaction and dispersive van der Waals (vdW) interactions. In case of the model A (Fig. 6.3.7), 4,4'-BP molecule adhere to the surface via binding of the surface atoms with the π-electronic system of aromatic rings, but in the model B – through the C–H σ-bonds, and in case of model C – through the electron lone pair of nitrogen in the 4,4'-BP molecule [168]. As it can be seen in Fig. 6.3.10, at the vdW-DF2 level of theory, the 4,4'-BP – Bi(111) interaction is the strongest for the orientation if the aromatic rings are parallel to the Bi(111) surface. For the 4,4'-BP orientation pointing N-atom towards the surface, there is a pronounced difference (>10 kJ/mol) in energy at the most and the least preferable positions for 4,4'-BP molecules at the Bi(111) surface. Herewith, the drastic difference between the results calculated using PBE (Perdew, Burke, and Ernzerhof [135]) and vdW-DF2 functionals imply that the van der Waals interactions play the major role being somehow proportional to the contact area of adsorbed molecules.

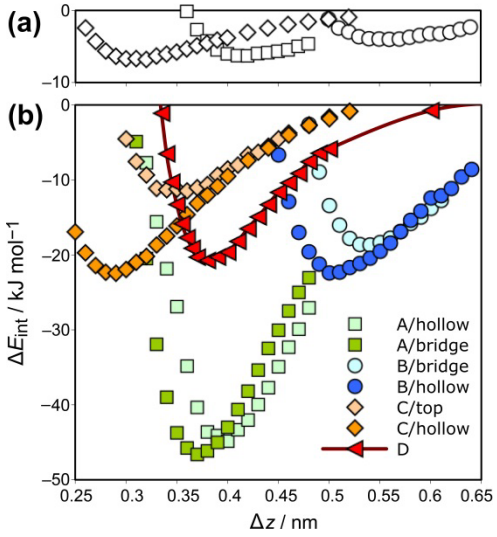

Figure 6.3.10. Potential energy curves for the 4,4'-bipyridine interaction with model Bi(111) surface (A,B,C) at the most (darker marks) and the least (lighter) preferable sites at Bi(111) surface, calculated using PBE (a) and vdW-DF2 (b) functionals. ΔE_{int} is defined by Eq. (5.1) and Δz is the distance between the surface plane and N atom in 4,4'-BP molecule (in case of dimer, between N atoms). The potential energy curves for interaction in 4,4'-BP dimer (D) is shown with Bezier cubic spline curve. The notation corresponds to the models (A, B, C, and D) and the molecule position relative to the bismuth slab (top, bridge, hollow), as defined in caption to Fig. 6.3.9.

Table 1. Interaction energies and distances from the N atom in 4,4'-BP to the surface plane and between N atoms in the dimer.

	vdW-DF2		**M06-L**	
Model	**$-\Delta E_{int}$, kJ/mol**	***d*, nm**	**$-\Delta E_{int}$, kJ/mol**	***d*, nm**
Dimer (Par)	20.8	0.38	12.2	0.36
Dimer (Plane)	4.1	0.67	> 0	
A (Par)	46.6	0.37	49.0	0.36
B (Per)	22.4	0.50	20.3	0.49
C (N)	22.5	0.29	23.3	0.30
A' (Par)	41.3	0.42	42.0	–
B' (Per)	43.1	0.52	35.7	–

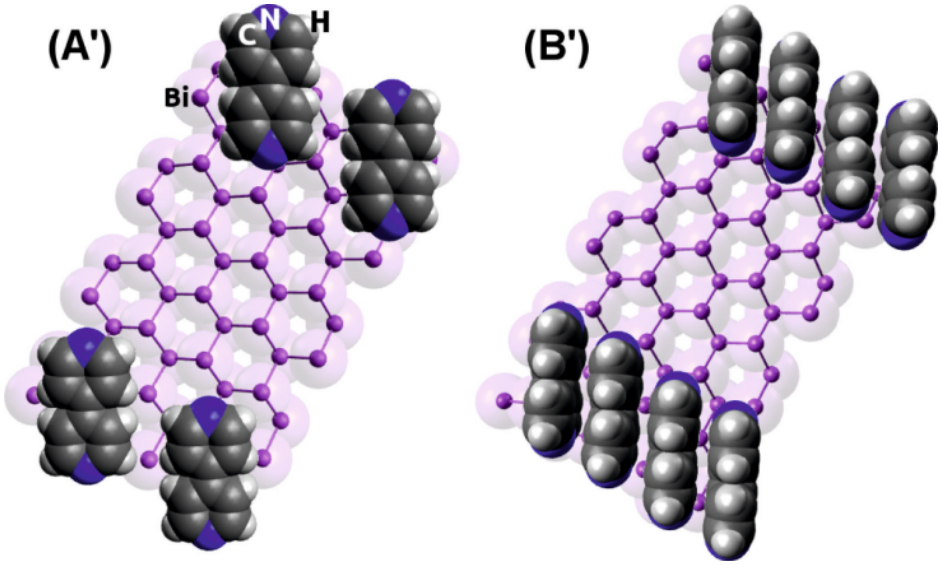

Figure 6.3.11. Models illustrating 4,4'-BP strips at Bi(111). Atoms are shown using vdW-spheres. Model A': 4×6 Bi(111) cell with two adsorbed 4,4'-BP molecules per cell in parallel orientation. Model B': 4×6 Bi(111) cell with four adsorbed 4,4'-BP molecules per cell in perpendicular orientation.

In Table 1 the minimum interaction energy values are summarized and provided ΔE_{int} values are calculated as a perturbation to a single point PBE calculations using M06-L functional. Models A' and B' (Fig. 6.3.11, describing the stripes of the 4,4'-BP molecules, were fully optimized at vdW-DF2 level. For the model A' the M06-L and vdW-DF2 results are consistent, but the M06-L interaction energy value for the model B' (−37.5 kJ/mol) is lower compared to the vdW-DF2 value (−43.1 kJ/mol). This is due to the difference in vdW-DF2 and M06-L results for the 4,4'-BP dimer (−20.8 vs. 12.2 kJ/mol), where M06-L underestimates the long-range attraction magnitude (for detailed approximation see data in Refs. [169,170]).

The total interaction energy for model B' can be split into two components summarizing the intermolecular interactions between 4,4'-BP molecules and interactions of the 4,4'-BP molecule with the Bi(111) surface (ΔE_{int}(B') ≈ ΔE_{int}(B) + ΔE_{int}(D), see data in Table 1). Differently, ΔE_{int}(A') ≈ ΔE_{int}(A), implies an exceedingly weak attraction between the 4,4'-BP molecules lying in one plane parallel to the surface (Table 1).

A significant attraction between 4,4'-BP molecules is possible only when the molecules are oriented with their aromatic rings perpendicular to the Bi(111) surface plane. The additional stabilization through the vdW interaction makes adhesion of the 4,4'-BP molecules to the surface slightly stronger for the model B' than that for the model A'. Herewith, the specific geometry of the corrugated Bi(111) surface (atomic scale) plays a pivotal role for the adsorption of the 4,4'-BP molecules in perpendicular orientation, occupying the specific surface

sites with the distance close to the optimal distance for 4,4'-BP molecules in the dimer.

It is deduced that the π-π-interactions are similarly enriched in case of the 4,4'-BP adsorption at Au(111) and Cu(111) surfaces, where the molecules have the preferable orientations pointing the N-atom towards and perpendicular to the electrode surface, respectively [5,34].

At the Bi(111) surface the adsorption through the lone electron pair of the nitrogen atom is energetically less preferable. Also, at Bi(111), the larger distance between the adsorption sites is more suitable for shifted perpendicular orientation of the molecules (Fig. 6.3.11) rather than through the nitrogen lone electron pair.

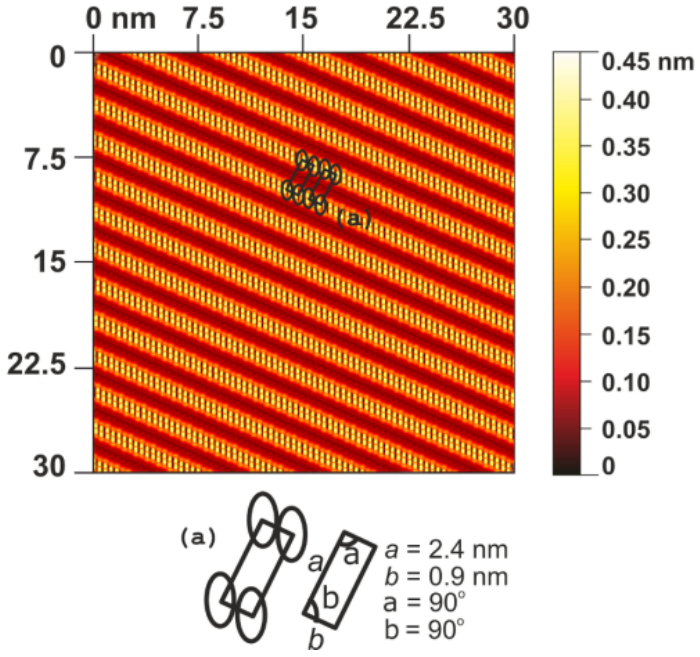

Figure 6.3.12. Theoretical constant current heights of the 2D arrays at Bi(111) surface (4×6 atoms cluster) with the adsorbate forming stripes (model B' assuming protonated 4,4'-BP molecules).

Moreover, according to the experimental data measured applying the surface enhanced infrared adsorption spectroscopy (SEIRAS), the adsorbed 4,4'-BP molecules are protonated in an acidified solution and therefore, the N-electron pairs are bonded with protons. Thus, protons were added to the molecules in the B' model, in order to analyze the charged interface behavior.

The theoretically modeled STM image for this model is presented in Fig. 6.3.12 showing the stripes of protonated 4,4'-BP molecules over the Bi(111) surface. In this model the unit cell parameters reasonably agree with distances (0.91 nm vs. 0.9 nm and 2.4 nm vs. 2.7 nm) measured using *in situ* STM

method (see Figs. 6.3.4 and 6.3.12). The slight difference in length between the rows corresponds to a distance between surface Bi-atoms in the same direction and thus, it is due to the choice of the model unit cell length only. More importantly, the DDEC (Density Derived Electrostatic and Chemical) charge of +0.6 at protonated 4,4'-BPH_2 in model B' finds confirmation in cyclic voltammetry observation of a one-electrode reduction peak. In addition, the calculated spectrum for 4,4-BPH_2^+ dimer is in an agreement with the SEIRAS spectra measured (Fig. 6.3.8).

6.3.5. Discussion of the Bi(111) | 4,4'-BP interface

The very low capacitance values ~1.0 $\mu F \cdot cm^{-2}$ observed in Figs. 6.3.3b and c indicate the formation of the highly dense 2D condensed layer (or very compact adsorption layer) characterized by the very low effective dielectric constant ε_{eff} for adsorption layer for 4,4'-BP at the Bi(111) surface and the systematic decrease of the capacitance values at peak potentials is explained by the adsorption of surface blocking intermediates (irreversible adsorption of reduction/oxidation processes). The recovering of the shape of *C*, *E*-curves is only possible after cleaning (rinsing) the electrode with Milli Q + water outside of the measurement cell. Thus, the quasi-reversible adsorption/electron transfer, i.e., oxidation of 4,4'-BP is in an agreement with SEIRAS data, given in Fig. 6.3.8 and data in Refs. [33,96,168], takes place. Adsorbed 4,4'-BP species are identified as (4,4'-BPH_2^+)$_2$ dimers as shown in *in situ* STM, SEIRAS and computation results. It should be also mentioned that the (4,4'-BPH_2^+)$_2$ molecular complexes in the adsorption layer are very strongly interacted and/or there are very strong Van der Waals interactions (see DFT modelling results), almost like chemical interaction between the adsorbed intermediates.

The existence of 2D-condesed monomolecular 4,4'-BP film at Au(*hkl*), like in this work, was established by Mayer et al. [5,34] and Maestre et al. at Au(*hkl*) only [171–173]. The mentioned authors suggested that the observed phase transitions can be associated with the electrode-potential induced orientation changes of the adsorbed 4,4'-BP at electrode surface.

A good overall agreement between the modeled STM data and *in situ* STM results (Figs. 6.3.4 and 6.3.12) indicates a possible arrangement of the 4,4'-BP molecules at Bi(111). The molecular strips of the protonated and reduced 4,4'-BP molecules oriented with their aromatic rings perpendicular to the Bi(111) surface (model B' in Fig. 6.3.11) are deduced taking in account the electrochemical impedance and SEIRAS data (Fig. 6.3.8). These conclusions apply directly to the patterns observed in acidified 0.5 M Na_2SO_4 aqueous solutions. The positive charge of the protonated 4,4'-BP molecules attracts the counter-charge of sulfate anions. This effect increases with the Na_2SO_4 concentration. Accordingly, more 4,4'-BP molecules are adsorbed at the Bi(111) surface from the more concentrated sodium sulfate electrolyte solution (Fig. 6.3.4), while from the less concentrated sodium sulfate electrolyte (Fig 6.3.6.),

the more expressed repulsive forces between the protonated 4,4'-BP molecules result in formation of the less compact adsorption layer.

Thayer et al. stated that at Bi(001) electrode, the adsorbed pentacene forms thin films, where the pentacene molecules are oriented perpendicularly, differently from the parallel orientation at *d*-metals [174]. In case of copper hexadecafluorophthalocyanine adsorption at Bi(110) and at thin Bi layer deposited onto Ag(111) surfaces, it was demonstrated, that there is a weaker attractive interaction between the adsorbate molecules at the Bi(110) surface. However, in all cases, the good matching between the substrate and adsorbate lattices is the main key factor [20] for self-assembly of the adsorbate particles [175]. In case of the 4,4'-BP adsorption at Cu(111), Diao et al. [6] observed the stripes of molecules with IR-fingerprint, almost identical to the one observed by us in this study at Bi(111). However, at Au(111) surface, 4,4'-BP cations usually takes orientation with N-atom pointed towards the surface and therefore a different IR-spectra have been observed [5,34]. Probably, the intermolecular interactions of 4,4'-BP molecules adsorbed at Cu(111) or Bi(111) are enhanced due to the lattice matching supported by hydrogen bonding with water molecules and electrostatic interactions with counter-ions [176].

We notice here that in our calculated theoretical STM images for all 4,4'-BP molecules are identical, while in experimental STM image, every second molecule is clearly visible, just as at Cu(111) [6]. This is not surprising, as in the DFT calculations, firstly, all molecules are indeed identical and, secondly, they have exactly the same charge as induced at the surface. However, in more realistic conditions, the charge excess provided by 4,4'-BPH_2^+ is screened by the base electrolyte sulfate ions, not presented in the applied theoretical models.

7. SUMMARY

The atomic resolution images were detected on both $Sb(111)^{C}$ and $Sb(111)^{EP}$ electrodes. The *in situ* STM data showed that there were no quick surface reconstruction processes, and the surface structures of $Sb(111)^{C}$ and $Sb(111)^{EP}$ were stable within the potential region investigated similarly to the Bi(111) single crystal electrode, studied previously [29].

Therefore, it can be concluded that $Sb(111)^{C}$ and $Sb(111)^{EP}$ electrodes, in addition to $Bi(111)^{C}$ and $Bi(111)^{EP}$ [3,29,81], as the so-called Hg-like electrodes with the high hydrogen evolution overpotential [30,59,63,83,84,90], applicable in electroanalysis of heavy metal cations, as well as nanocluster activators for polymer electrolyte fuel cells, can be used for future studies of the more complicated two-dimensional adsorption layer formation processes of various organic compounds and ionic liquids.

It is also important to mention that electrochemical polishing, implemented in this work, is giving very similar results as cleaving method applied for preparation of Sb(111) and Bi(111) single crystal planes. Thus, atomically flat regions have been observed for all Sb(111) and Bi(111) electrodes studied. Therefore, the electrochemical polishing is a quite universal surface treatment method and can be implemented to study some fundamental electrical double layer properties of the surface structure and can be applied for general electrochemical adsorption/desorption studies as well.

The noticeable influence of the Bi(111) electrode potential and thiourea (TU) concentration on the adsorption kinetics of TU has been demonstrated. It was found that in the region of maximum adsorption ($E > -0.85$ V) the slow adsorption, the partial charge transfer and diffusion steps are the rate determining stages for TU adsorption at the Bi(111) electrode. For Bi(111) | x M TU + 0.05 M Na_2SO_4 + 2.5×10^{-5} M H_2SO_4 interface, the stable adsorbate adlayer, detectable by using the *in situ* STM method, has been observed only at the weakly negatively and positively charged electrode surface, where the strong specific adsorption with the partial charge transfer from TU to Bi(111) occurs. The *in situ* STM data are in a good agreement with the impedance data, indicating that the weak chemisorption of TU with the partial charge transfer starts only at $E > -0.85$ V; i.e. at moderately negatively charged Bi(111) electrode surface. Therefore, as a first approximation, for dilute TU solutions, the Nyquist plots can be simulated with the modified Frumkin and Melik-Gaikazyan circuit, where the semi-infinite diffusion model (impedance) has been replaced by the general finite length diffusion impedance. For more concentrated TU solutions and at $E \geq -1.3$ V, the more complicated equivalent circuit should be used, where the charge transfer resistance is added in parallel with the adsorption capacitance and generalized finite length mass transfer resistance, indicating that two parallel (adsorption with the partial charge transfer and 'true' faradic charge transfer) limiting processes are occurring at the same time.

The study of 4,4'-bipyridine (4,4'-BP) adsorption from acidified sodium sulfate electrolyte solutions onto the Bi(111) surface revealed the presence of very well-organized nanoscale 4,4'-BP structures. Within the region of maximum adsorption, at least three capacitance pits, indicating existence of these adsorption regions in the differential capacitance versus electrode potential curve, have been observed.

The cyclic voltammograms for 4,4'-BP + base electrolyte at Bi(111) demonstrate that at lower 4,4'-BP concentrations the adsorption processes are nearly reversible. However, the electrochemical processes at higher 4,4'-BP concentrations and at more anodic potentials are quite irreversible, which is probably caused by the reduction of 4,4'-BP in two steps and future formation of compact adsorption stripes from $(4,4'\text{-}BPH_2^+)_n$ ionic complexes at the electrode surface.

It was demonstrated by *in situ* STM data, that at negative potentials the adsorbed 4,4'-BP molecules form parallel stripes at the Bi(111) surface. Density functional theory (DFT) calculations data demonstrated that a single 4,4'-BP molecule prefers adsorption with the aromatic rings parallel to the Bi(111) surface. However, due to the noticeable van der Waals attraction between multiple molecules in the stripes, the protonated 4,4'-BP ions (molecules) are oriented with their aromatic rings perpendicular to the surface plane. A good agreement between the theoretically modelled and the measured STM data, as well as between calculated and measured SEIRAS spectra, and electrochemical CV, impedance and differential capacitance measurements supports the hypothesis of perpendicular alignment of the 4,4'-BP ionic complexes at the Bi(111) electrode surface, forming a monolayer of $(4,4'\text{-}BPH_2^+)_n$, packed into the ordered rows. It is important to note, that the key factor leading to the formation of the nanoscale well-ordered structures on the single crystal Bi(111) surface is the close matching of the optimum distance for intermolecular interactions with the distance between adsorption positions of ionic complexes (molecules). Formation of the ordered interfacial structures, similar to the observed adsorption patterns of 4,4'-BP on top of the Bi(111) surface can be predicted using DFT calculations with proper description of the van der Waals interactions, as demonstrated in this study.

8. REFERENCES

[1] J.E. Green, J. Wook Choi, A. Boukai, Y. Bunimovich, E. Johnston-Halperin, E. DeIonno, et al., A 160-kilobit molecular electronic memory patterned at 1011 bits per square centimetre, Nature. 445 (2007) 414–417.

[2] J.R. Hahn, H.S. Kang, Role of molecular orientation in vibration, hopping, and electronic properties of single pyridine molecules adsorbed on Ag(1 1 0) surface: A combined STM and DFT study, Surf. Sci. 604 (2010) 258–264.

[3] S. Kallip, H. Kasuk, V. Grozovski, P. Möller, E. Lust, Adsorption of camphor and 2,2′-bipyridine on Bi(1 1 1) electrode surface, Electrochimica Acta. 53 (2008) 4035–4045.

[4] T. Dretschkow, D. Lampner, T. Wandlowski, Structural transitions in 2,2'-bi-pyridine adlayers on Au(111) – an in-situ STM study, J. Electroanal. Chem. 458 (1998) 121–138.

[5] D. Mayer, T. Dretschkow, K. Ataka, T. Wandlowski, Structural transitions in 4,4'-bipyridine adlayers on Au(111) – an electrochemical and in-situ STM-study, J. Electroanal. Chem. 524 (2002) 20–35.

[6] Y.-X. Diao, M.-J. Han, L.-J. Wan, K. Itaya, T. Uchida, H. Miyake, et al., Adsorbed Structures of 4,4'-Bipyridine on Cu(111) in Acid Studied by STM and IR, Langmuir. 22 (2006) 3640–3646.

[7] R. Wiesendanger, H.-J. Güntherodt, Scanning tunneling microscopy II, Springer-Verlag, Berlin, 1992.

[8] M. Wilms, P. Broekmann, C. Stuhlmann, K. Wandelt, In-situ STM investigation of adsorbate structures on Cu(111) in sulfuric acid electrolyte, Surf. Sci. 416 (1998) 121–140.

[9] Б.Б. Дамаскин, О.А. Петрий, Введение в электрохимическую кинетику, Москва, 1983.

[10] H. Kasuk, G. Nurk, K. Lust, E. Lust, Adsorption of uracil on bismuth single crystal planes, J. Electroanal. Chem. 580 (2005) 128–134.

[11] E. Lust, J. Erlich, U. Palm, The study of butyl acetate adsorption on bismuth single crystal planes, Sov. Electrochem. 22 (1986) 659.

[12] H. Kasuk, G. Nurk, E. Lust, Adsorption of sodium dodecyl sulfate on the bismuth (1 1 1), (0 0 1) and planes, J. Electroanal. Chem. 613 (2008) 80–96.

[13] T. Wandlowski, Phase Transitions in Two-dimensional Adlayers at Electrode Surfaces: Thermodynamics, Kinetics, and Structural Aspects, in: A.J. Bard, M. Stratmann (Eds.), Encycl. Electrochem., Wiley VCH, Weinheim, 2002.

[14] D.M. Kolb, Reconstruction phenomena at metal-electrolyte interfaces, Prog. Surf. Sci. 51 (1996) 109–173.

[15] T. Dretschkow, T. Wandlowski, An order–disorder–order adlayer transition of 2,2'-bipyridine on Au(111), Electrochimica Acta. 45 (1999) 731–740.

[16] Q. Jin, J.. Rodriguez, C.. Li, Y. Darici, N.. Tao, Self-assembly of aromatic thiols on Au(111), Surf. Sci. 425 (1999) 101–111.

[17] I. Burgess, C.A. Jeffrey, X. Cai, G. Szymanski, Z. Galus, J. Lipkowski, Direct Visualization of the Potential-Controlled Transformation of Hemimicellar Aggregates of Dodecyl Sulfate into a Condensed Monolayer at the Au(111) Electrode Surface, Langmuir. 15 (1999) 2607–2616.

[18] K.G. Baikerikar, S. Sathyanarayana, Adsorption of camphor, camphene, pinene, naphthalene and nonylic acid at the mercury-solution interface, J. Electroanal. Chem. Interfacial Electrochem. 24 (1970) 333–344.
[19] N.A. Paltusova, A. Alumaa, U. Palm, Elektrokhimiya. 16 (1980) 1249.
[20] C. Buess-Herman, C. Franck, L. Gierst, On the influence of molecular structure on the orientation and the occurrence of phase transitions in organic adsorbed layers at the mercury – water interface, J. Electroanal. Chem. 329 (1992) 91–102.
[21] H. Striegler, D. Krznarić, D.. Kolb, Two-dimensional condensation of camphor and its derivatives on Au(111) electrodes, J. Electroanal. Chem. 532 (2002) 227–235.
[22] V. Ivaništšev, R.R. Nazmutdinov, E. Lust, Density functional theory study of the water adsorption at Bi(111) electrode surface, Surf. Sci. 604 (2010) 1919–1927.
[23] V. Ivaništšev, R.R. Nazmutdinov, E. Lust, A comparative DFT study of the adsorption of H2O molecules at Bi, Hg, and Ga surfaces, Surf. Sci. 609 (2013) 91–99.
[24] E. Anderson, V. Grozovski, L. Siinor, C. Siimenson, V. Ivaništšev, K. Lust, et al., Influence of the electrode potential and in situ STM scanning conditions on the phase boundary structure of the single crystal Bi(1 1 1)|1-butyl-4-methyl-pyridinium tetrafluoroborate interface, J. Electroanal. Chem. 709 (2013) 46–56.
[25] L. Siinor, C. Siimenson, V. Ivaništšev, K. Lust, E. Lust, Influence of cation chemical composition and structure on the double layer capacitance for Bi(111) | room temperature ionic liquid interface, J. Electroanal. Chem. 668 (2012) 30–36.
[26] L.-J. Wan, Fabricating and Controlling Molecular Self-Organization at Solid Surfaces: Studies by Scanning Tunneling Microscopy, Acc. Chem. Res. 39 (2006) 334–342.
[27] A. Kühnle, Self-assembly of organic molecules at metal surfaces, Curr. Opin. Colloid Interface Sci. 14 (2009) 157–168.
[28] M. Troyanovskii, V.S. Edelman, Crystallogr. Rep. 44 (1999).
[29] S. Kallip, E. Lust, In situ STM studies of Bi(111) electrodes in aqueous electrolyte solutions, Electrochem. Commun. 7 (2005) 863–867.
[30] S. Kallip, P. Laukkanen, A. Jänes, V. Sammelselg, J. Väyrynen, P. Miidla, et al., Investigation of the surface topography and double layer characteristics of variously pre-treated antimony single crystal electrodes, Surf. Sci. 532–535 (2003) 1121–1126.
[31] H. Noda, T. Minoha, L.-J. Wan, M. Osawa, Adsorption and ordered phase formation of 2,2′-bypyridine on Au(111): a combined surface-enhanced infrared and STM study, J. Electroanal. Chem. 481 (2000) 62–68.
[32] M.J. Esplandiu, M.L. Carot, F.P. Cometto, V.A. Macagno, E.M. Patrito, Electrochemical STM investigation of 1,8-octanedithiol monolayers on Au(1 1 1).: Experimental and theoretical study, Surf. Sci. 600 (2006) 155–172.
[33] F. Cunha, N.J. Tao, X.W. Wang, Q. Jin, B. Duong, J. D'Agnese, Potential-induced phase transitions in 2,2'-bipyridine and 4,4'-bipyridine monolayers on Au(111) studied by in situ scanning tunneling microscopy and atomic force microscopy, Langmuir. 12 (1996) 6410–6418.
[34] T. Wandlowski, K. Ataka, D. Mayer, In Situ Infrared Study of 4,4'-Bipyridine Adsorption on Thin Gold Films, Langmuir. 18 (2002) 4331–4341.
[35] K. Umemura, N. Nishida, M. Hara, H. Sasabe, W. Knoll, Morphology and stability of chemically modified electrode surfaces without -SH and -SS-structures

studied by scanning tunneling microscopy, J. Electroanal. Chem. 438 (1997) 207–211.
[36] L.S. Pinheiro, M.L.A. Temperini, Interaction of 2-mercaptopyrimidine and 4,4′-bipyridine and competition experiments between bipyridines and 1, 10′-phenanthroline for the thiol layer on Au (111) by STM, Appl. Surf. Sci. 171 (2001) 89–100.
[37] T. Dretschkow, T. Wandlowski, Structural studies of 2,2'-bipyridine on Au(100), J. Electroanal. Chem. 467 (1999) 207–216.
[38] J. Gomez, L. Vazquez, A.M. Baro, N. Garcia, C.L. Perdriel, W.E. Triaca, et al., Surface topography of (100)-type electro-faceted platinum from scanning tunnelling microscopy and electrochemistry, (1986).
[39] L. Vazquez, J.M. Rodríguez, J.G. Herrero, A.M. Baro, N. Garcia, J.C. Canullo, et al., Scanning tunneling microscopy of platinum electrode surfaces with different preferred crystallographic orientations, Surf. Sci. 181 (1987) 98–106.
[40] L. Vazquez, A. Bartolome, A.M. Baro, C. Alonso, R.C. Salvarezza, A.J. Arvia, STM-SEM combination study on the electrochemical growth mechanism and structure of gold overlayers: A quantitative approach to electrochemical metal surface roughening, Surf. Sci. 215 (1989) 171–189.
[41] O. Lev, F.-R. Fan, A.J. Bard, The Application of Scanning Tunneling Microscopy to In Situ Studies of Nickel Electrodes under Potential Control, J. Electrochem. Soc. 135 (1988) 783–784.
[42] P. Lustenberger, H. Rohrer, R. Christoph, H. Siegenthaler, Scanning tunneling microscopy at potential controlled electrode surfaces in electrolytic environment, J. Electroanal. Chem. Interfacial Electrochem. 243 (1988) 225–235.
[43] J. Wiechers, T. Twomey, D.M. Kolb, R.J. Behm, An in-situ scanning tunneling microscopy study of au (111) with atomic scale resolution, J. Electroanal. Chem. Interfacial Electrochem. 248 (1988) 451–460.
[44] K. Itaya, E. Tomita, Scanning tunneling microscope for electrochemistry – a new concept for the in situ scanning tunneling microscope in electrolyte solutions, Surf. Sci. 201 (1988) L507–L512.
[45] W. Schmickler, Electronic effects in the electric double layer, Chem. Rev. 96 (1996) 3177–3200.
[46] A. Vaught, T.W. Jing, S.M. Lindsay, Non-exponential tunneling in water near an electrode, Chem. Phys. Lett. 236 (1995) 306–310.
[47] W. Schmickler, D. Henderson, A model for the scanning tunneling microscope operating in an electrolyte solution, J. Electroanal. Chem. Interfacial Electrochem. 290 (1990) 283–291.
[48] C.J. Chen, Introduction to scanning tunneling microscopy, Oxford University Press New York, 1993.
[49] D.M. Eigler, P.S. Weiss, E.K. Schweizer, N.D. Lang, Imaging Xe with a low-temperature scanning tunneling microscope, Phys. Rev. Lett. 66 (1991) 1189–1192.
[50] W. Schmickler, On the possibility of measuring the adsorbate density of states with a scanning tunneling microscope, J. Electroanal. Chem. Interfacial Electrochem. 296 (1990) 283–289.
[51] P. Sautet, Images of adsorbates with the scanning tunneling microscope: Theoretical approaches to the contrast mechanism, Chem. Rev. 97 (1997) 1097–1116.
[52] P. Sautet, Atomic adsorbate identification with the STM: a theoretical approach, Surf. Sci. 374 (1997) 406–417.

[53] A.J. Bard, F.R.F. Fan, J. Kwak, O. Lev, Scanning electrochemical microscopy. Introduction and principles, Anal. Chem. 61 (1989) 132–138.
[54] J. Lipkowski, P.N. Ross, Imaging of surfaces and interfaces, Wiley-VCH Pub, New York, 1999.
[55] T.P. Moffat, in: A.J. Bard, M. Stratmann (Eds.), Encycl. Electrochem., Wiley-VCH, Weinheim, 2002.
[56] M.P. Soriaga, D.A. Harrington, J.L. Stikney, A. Wieckowski, in: R.E. White, J.O. Bockris, B.E. Conway (Eds.), Mod. Asp. Electrochem., Plenum, New York, 1996.
[57] R. Sonnenfeld, J. Schneir, P.K. Hansma, in: R.E. White, J.O. Bockris, B.E. Conway (Eds.), Mod. Asp. Electrochem., Plenum, New York, 1996.
[58] P.W. Atkins, J. De Paula, Physical chemistry., W. H. Freeman and Co., New York, 2010.
[59] A. Hamelin, in: R.E. White, J.O. Bockris, B.E. Conway (Eds.), Mod. Asp. Electrochem., Plenum, New York, 1985.
[60] D.M. Kolb, Berichte Bunsenges. Für Phys. Chem. 92 (1988) 1175.
[61] D.M. Kolb, Structure of electrified interfaces, in: J. Lipkowski, P.N. Ross (Eds.), VCH N. Y., 1993: p. 65.
[62] M.A. Vorotyntsev, in: R.E. White, J.O. Bockris, B.E. Conway (Eds.), Mod. Asp. Electrochem., Plenum, New York, 1986.
[63] S. Trasatti, E. Lust, The Potential of Zero Charge, in: White, R.E., Bockris, J.O'M., Conway, B.E. (Eds.), Mod. Asp. Electrochem., Kluwer Academic / Plenum Publishers, New York, 1999: pp. 1–193.
[64] A. Hamelin, L. Stoicoviciu, Comments on the inner-layer capacity versus charge density curves, J. Electroanal. Chem. Interfacial Electrochem. 271 (1989) 15–26.
[65] A. Hamelin, L. Stoicoviciu, F. Silva, The temperature dependence of the double-layer properties of gold faces in perchloric acid solutions: Part II. The (110) gold face, J. Electroanal. Chem. Interfacial Electrochem. 236 (1987) 283–294.
[66] A. Hamelin, P. Dechy, Comptes Rendus Chim. 276 (1973) 33.
[67] X. Gao, G.J. Edens, A. Hamelin, M.J. Weaver, Real-space formation and dissipation mechanisms of hexagonal reconstruction on Au(100) in aqueous media as explored by potentiodynamic scanning tunneling microscopy, Surf. Sci. 296 (1993) 333–351.
[68] D.M. Kolb, J. Schneider, The study of reconstructed electrode surfaces: Au(100)-(5×20), Surf. Sci. 162 (1985) 764–775.
[69] D.M. Kolb, J. Schneider, Surface reconstruction in electrochemistry: Au(100-(5 × 20), Au(111)-(1 × 23) and Au(110)-(1 × 2), Electrochimica Acta. 31 (1986) 929–936.
[70] G. Valette, A. Hamelin, Structure et propriétés de la couche double électrochimique à l'interphase argent/solutions aqueuses de fluorure de sodium, J. Electroanal. Chem. Interfacial Electrochem. 45 (1973) 301–319.
[71] J. Clavilier, R. Faure, G. Guinet, R. Durand, Preparation of monocrystalline Pt microelectrodes and electrochemical study of the plane surfaces cut in the direction of the {111} and {110} planes, J. Electroanal. Chem. Interfacial Electrochem. 107 (1979) 205–209.
[72] M. Höpfner, W. Obretenov, K. Jüttner, W.J. Lorenz, G. Staikov, V. Bostanov, et al., STM studies of real and quasi-perfect silver single crystal surfaces used in electrochemical experiments, Surf. Sci. 248 (1991) 225–233.

[73] W. Obretenov, M. Höpfner, W.J. Lorenz, E. Budevski, G. Staikov, H. Siegenthaler, Characterization of the surface structure of silver single crystal electrodes by ex situ and in situ STM, Surf. Sci. 271 (1992) 191–200.
[74] N. Batina, A.S. Dakkouri, D.M. Kolb, The surface structure of flame-annealed Au(100) in aqueous solution: An STM study, J. Electroanal. Chem. 370 (1994) 87–94.
[75] J.W. Mathews, Epitaxial Growth, Academic Press, New York, 1975.
[76] G.L. Borges, M.G. Samant, K. Ashley, Grazing Incidence X-Ray and Electrochemical Study of Thin Film Copper(111) on Mica, J. Electrochem. Soc. 139 (1992) 1565–1568.
[77] R. Gómez, M.J. Weaver, Electrochemical infrared studies of monocrystalline iridium surfaces Part I: Electrooxidation of formic acid and methanol, J. Electroanal. Chem. 435 (1997) 205–215.
[78] W.B. Pearson, The Crystal Chemistry and Physics of Metals and Alloys, Wiley-Interscience, 1972.
[79] М.В. Робертс, Ц.С. Маккее, Химия поверхности раздела металл-газ, Изд. Мир, Moscow, 1981.
[80] L.I. Daikhin, A.A. Kornyshev, M. Urbakh, Nonlinear Poisson–Boltzmann theory of a double layer at a rough metal/electrolyte interface: A new look at the capacitance data on solid electrodes, J. Chem. Phys. 108 (1998) 1715–1723.
[81] R. Jäger, S. Kallip, V. Grozovski, K. Lust, E. Lust, Electroreduction of anions on chemically etched and electrochemically polished Bi(1 1 1) electrode, J. Electroanal. Chem. 622 (2008) 79–89.
[82] E. Lust, A. Jänes, V. Sammelselg, P. Miidla, Influence of charge density and electrolyte concentration on the electrical double layer characteristics at rough cadmium electrodes, Electrochimica Acta. 46 (2000) 185–191.
[83] E. Lust, S. Kallip, P. Möller, A. Jänes, V. Sammelselg, P. Miidla, et al., Influence of Surface Charge Density on the Electrochemically Derived Surface Roughness of Bi Electrodes, J. Electrochem. Soc. 150 (2003) E175–E184.
[84] E. Lust, A. Jänes, V. Sammelselg, P. Miidla, K. Lust, Surface roughness of bismuth, antimony and cadmium electrodes, Electrochimica Acta. 44 (1998) 373–383.
[85] E. Lust, A. Jänes, K. Lust, M. Väärtnõu, Electric double layer structure and adsorption of cyclohexanol on single crystal cadmium, antimony and bismuth electrodes, Electrochimica Acta. 42 (1997) 771–783.
[86] E. Lust, A. Jänes, K. Lust, R. Pullerits, Adsorption of organic compounds and hydrophilicity of bismuth, cadmium and antimony electrodes, J. Electroanal. Chem. 431 (1997) 183–201.
[87] E. Lust, A. Jänes, K. Lust, J. Erlich, The structure of the electrical double layer at the faces of bismuth, antimony, or cadmium single crystals in surface-inactive electrolytes, Russ. J. Electrochem. 32 (1996) 552–564.
[88] A. Jänes, E. Lust, Russ. J. Electrochem. 32 (1996) 943–945.
[89] A. Jänes, E. Lust, Russ. J. Electrochem. 31 (1995) 596–599.
[90] E. Lust, K. Lust, A. Jänes, Russ. J. Electrochem. 31 (1995) 807.
[91] E. Lust, A. Jänes, K. Lust, J. Erlich, Russ. J. Electrochem. 32 (1995) 552–564.
[92] E. Lust, A. Jänes, Russ. J. Electrochem. 30 (1994) 321.
[93] E. Lust, A. Jänes, Sov. Electrochem. 28 (1992) 650–653.
[94] B. Xu, N.J. Tao, Measurement of Single-Molecule Resistance by Repeated Formation of Molecular Junctions, Science. 301 (2003) 1221–1223.

[95] P. Qian, H. Nanjo, T. Yokoyama, T.M. Suzuki, K. Akasaka, H. Orhui, Chiral molecular patterns of self-assembled ion pairs composed of (R,S), (S)-16-methyloctadecanoic acid and 4,4′-bipyridine, Chem. Commun. (2000) 2021–2022.
[96] T. Lu, T.M. Cotton, R.L. Birke, J.R. Lombardi, Raman and surface-enhanced Raman spectroscopy of the three redox forms of 4,4'-bipyridine, Langmuir. 5 (1989) 406–414.
[97] K. Zawada, J. Bukowska, Surface-enhanced Raman spectroscopy and electrochemistry of 2,2′-bipyridine adsorbed at copper electrode, Electrochimica Acta. 49 (2004) 469–476.
[98] J. Kruusma, L. Nei, J.L. Hardcastle, R.G. Compton, E. Lust, H. Keis, Sonoelectroanalysis: Anodic Stripping Voltammetric Determination of Cadmium in Whole Human Blood, Electroanalysis. 16 (2004) 399–403.
[99] C.E. Banks, J. Kruusma, M.E. Hyde, A. Salimi, R.G. Compton, Sonoelectroanalysis: investigation of bismuth-film-modified glassy carbon electrodes, Anal. Bioanal. Chem. 379 (2004) 277–282.
[100] J.O. Bockris, A.K.N. Reddy, M. Gamboa-Aldeco, Modern electrochemistry, 2nd ed., Kluwer Academic Publishers, New York, 2002.
[101] D.A. Skoog, F.J. Holler, S.R. Crouch, Principles of instrumental analysis., Thomson Brooks/Cole, Belmont, CA, 2007.
[102] A.J. Bard, L.R. Faulkner, Electrochemical methods: fundamentals and applications, Wiley, New York, 2001.
[103] A.N. Frumkin, V.I. Melik-Gaykazyan, Determination of the kinetics of organic substances by measuring the capacitance and conductivity at the electrode-solution boundary, Dokl-Akad. Nauk USSR. 77 (1951) 885.
[104] V.I. Melik-Gaykazyan, Zh. Fiz. Khim. 26 (1952) 560.
[105] M. Sluyters-Rehbach, J. Sluyters, in: A.J. Bard (Ed.), Electroanal. Chem., Marcel Dekker, New York, 1970.
[106] R.D. Armstrong, W.P. Race, H.R. Thirsk, The kinetics of adsorption of neutral organic compounds at a mercury electrode, J. Electroanal. Chem. Interfacial Electrochem. 16 (1968) 517–529.
[107] K.S. Cole, R.H. Cole, Dispersion and Absorption in Dielectrics I. Alternating Current Characteristics, J. Chem. Phys. 9 (1941) 341–351.
[108] A.N. Frumkin, B.B. Damaskin, in: J.O. Bockris, B.E. Conway (Eds.), Mod. Asp. Electrochem., Plenum, New York, 1964.
[109] B.B. Damaskin, L.N. Nekrassov, O.A. Petrii, B.I. Podlovchenko, E.V. Stenina, N.V. Fedorovich, in: B.B. Damaskin (Ed.), Electrochem. Prop. Org. Compd. Solut., Moscow University Press, Moscow, 1985.
[110] U. Retter, H. Jehring, Untersuchungen der Adsorptionskinetik an der Phasengrenze Quecksilber/Elektrolyt durch analoge Sessung der Doppelschichtadmittanz, J. Electroanal. Chem. Interfacial Electrochem. 46 (1973) 375–380.
[111] W. Lorenz, F. Möckel, Adsorptionsisotherme und Adsorptionskinetik kappillaraktiver organischer Molekeln an der Quecksilberelektrode, Z. Electrochem. 60 (1956) 507–515.
[112] T.J. VanderNoot, Limitations in the analysis of ac impedance data with poorly separated faradaic and diffusional processes, J. Electroanal. Chem. Interfacial Electrochem. 300 (1991) 199–210.
[113] G.A. Tedoradze, R.A. Arakelyan, Dokl. Akad. Nauk SSSR. 156 (1964) 1170.

[114] B.B. Damaskin, O.A. Petrii, V.V. Batrakov, Adsorption of Organic Compounds on Electrodes, Plenum Press, New York, 1971.
[115] G. Nurk, A. Jänes, K. Lust, E. Lust, Adsorption kinetics of 2-methyl-2-butanol on bismuth single crystal planes, J. Electroanal. Chem. 515 (2001) 17–32.
[116] A. Jänes, G. Nurk, K. Lust, J. Ehrlich, E. Lust, Adsorption Kinetics of Normal-Heptanol on the Bismuth Single Crystal Planes, Russ. J. Electrochem. 38 (2002) 8–19.
[117] A. Jänes, E. Lust, Adsorption of D-ribose on bismuth single crystal plane electrodes, Electrochimica Acta. 47 (2001) 967–975.
[118] E. Lust, U. Palm, Adsorption-kinetics of cyclohexanol on the faces of a single-crystal bismuth electrode, Sov. Electrochem. 24 (1988) 227–231.
[119] W. Lorenz, Z. Electrochem. 62 (1958) 192.
[120] A. Zangwill, Physics at Surfaces, Cambridge University Press, 1988.
[121] E.B. Budevski, G.T. Staikov, W.J. Lorenz, Electrochemical Phase Formation and Growth: An Introduction to the Initial Stages of Metal Deposition, John Wiley & Sons, 2008.
[122] T. Vo-Dinh, G. Gauglitz, Handbook of spectroscopy, Wiley-VCH, Weinheim, 2003.
[123] P.R. Griffiths, De Haseth, Fourier transform infrared spectrometry, Wiley, New York, 1986.
[124] B.C. Smith, Fundamentals of Fourier transform infrared spectroscopy, CRC Press, Boca Raton, 1996.
[125] M. Osawa, In-situ Surface-Enhanced Infrared Spectroscopy of the Electrode/ Solution Interface, in: R.C. Alkire, D.M. Kolb, J. Lipkowski, P. Ross (Eds.), Adv. Electrochem. Sci. Eng., Wiley. com, 2006.
[126] A. Rodes, J.. Orts, J.. Pérez, J.. Feliu, A. Aldaz, Sulphate adsorption at chemically deposited silver thin film electrodes: time-dependent behaviour as studied by internal reflection step-scan infrared spectroscopy, Electrochem. Commun. 5 (2003) 56–60.
[127] R.A. Palmer, J.L. Chao, R.M. Dittmar, V.G. Gregoriou, S.E. Plunkett, Investigation of Time-Dependent Phenomena by Use of Step-Scan FT-IR, Appl. Spectrosc. 47 (1993) 1297–1310.
[128] K. Burke, The ABC of DFT, http://dft.uci.edu/doc/g1.pdf, 2007.
[129] A Primer in Density Functional Theory, n.d.
[130] C.J. Cramer, D.G. Truhlar, Density functional theory for transition metals and transition metal chemistry, Phys. Chem. Chem. Phys. PCCP. 11 (2009) 10757–10816.
[131] A.D. Becke, Phys. Rev. A: At., Mol., Opt. Phys. 38 (1988) 3098.
[132] J.P. Perdew, Phys. Rev. B: Condens. Matter Mater. Phys. 33 (1986) 8822.
[133] C. Lee, W. Yang, R.G. Parr, Phys. Rev. B: Condens. Matter Mater. Phys. 37 (1988) 785.
[134] J.P. Perdew, in: P. Ziesche, H. Eschrig (Eds.), Electron. Struct. Solids '91, Akademie Verlag, Berlin, 1991.
[135] J.P. Perdew, K. Burke, M. Enzerhof, Phys. Rev. Lett. 77 (1996) 3865.
[136] C. Adamo, V. Barone, J. Chem. Phys. 108 (1998) 664.
[137] P.J. Stephens, F.J. Devlin, C.F. Chabalowski, M.J. Frisch, Ab initio calculation of vibrational absorption and circular dichroism spectra using density functional force fields, J. Phys. Chem. 98 (1994) 11623–11627.
[138] A.D. Becke, J. Chem. Phys. 98 (1993) 5648.

[139] I. Horcas, R. Fernández, J.M. Gómez-Rodríguez, J. Colchero, J. Gómez-Herrero, A.M. Baro, WSXM: A software for scanning probe microscopy and a tool for nanotechnology, Rev. Sci. Instrum. 78 (2007) 013705–013705–8.
[140] D. Nečas, P. Klapetek, Gwyddion: an open-source software for SPM data analysis, Cent. Eur. J. Phys. 10 (2011) 1–8.
[141] T. Romann, Preparation and surface modification of bismuth thin film, porous, and microelectrodes, Thesis, 2010.
[142] T. Romann, E. Anderson, S. Kallip, H. Mändar, L. Matisen, E. Lust, Electroless deposition of bismuth on Si(111) wafer from hydrogen fluoride solutions, Thin Solid Films. 518 (2010) 3690–3693.
[143] T. Romann, O. Oll, P. Pikma, E. Lust, Abnormal infrared effects on bismuth thin film–EMImBF4 ionic liquid interface, Electrochem. Commun. 23 (2012) 118–121.
[144] M. Frisch, G. Truck, H. Schlegel, G. Scuseria, M. Robb, J. Cheeseman, et al., Gaussian 09, Revision A. 02, 2009, Gaussian, Inc Wallingford CT. (2009).
[145] T. Yanai, D.P. Tew, N.C. Handy, A new hybrid exchange–correlation functional using the Coulomb-attenuating method (CAM-B3LYP), Chem. Phys. Lett. 393 (2004) 51–57.
[146] K. Lee, É.D. Murray, L. Kong, B.I. Lundqvist, D.C. Langreth, Higher-accuracy van der Waals density functional, Phys. Rev. B. 82 (2010) 081101.
[147] J. Enkovaara, C. Rostgaard, J.J. Mortensen, J. Chen, M. Dułak, L. Ferrighi, et al., Electronic structure calculations with GPAW: a real-space implementation of the projector augmented-wave method, J. Phys. Condens. Matter. 22 (2010) 253202.
[148] S.N. Srirama, V. Ivanistsev, P. Jakovits, C. Willmore, Direct migration of scientific computing experiments to the cloud, in: 2013 Int. Conf. High Perform. Comput. Simul. HPCS, 2013: pp. 27–34.
[149] S.R. Bahn, K.W. Jacobsen, An object-oriented scripting interface to a legacy electronic structure code, Comput. Sci. Eng. 4 (2002) 56–66.
[150] T.A. Manz, D.S. Sholl, Improved Atoms-in-Molecule Charge Partitioning Functional for Simultaneously Reproducing the Electrostatic Potential and Chemical States in Periodic and Nonperiodic Materials, J. Chem. Theory Comput. 8 (2012) 2844–2867.
[151] M.D. Hanwell, D.E. Curtis, D.C. Lonie, T. Vandermeersch, E. Zurek, G.R. Hutchison, Avogadro: an advanced semantic chemical editor, visualization, and analysis platform, J. Cheminformatics. 4 (2012) 17.
[152] U. Palm, J. Ehrlich, T. Ehrlich, The Studies of the thiourea adsorption at Bismuth electrode, Sov. Electrochem. 8 (1974) 1180–1184.
[153] U. Palm, M. Pärnoja, Study of the adsorption of thiourea at the crysral faces of the bismuth single crystal electrode, Sov. Electrochem. 18 (1982) 411–415.
[154] A. Nosal-Wiercińska, Z. Fekner, G. Dalmata, The adsorption of thiourea on the mercury from neutral and acidic solutions of perchlorates, J. Electroanal. Chem. 584 (2005) 192–200.
[155] J.-Z. Zheng, B. Ren, D.-Y. Wu, Z.-Q. Tian, Thiourea adsorption on a Pt surface as detected by electrochemical methods and surface-enhanced Raman spectroscopy, J. Electroanal. Chem. 574 (2005) 285–289.
[156] R. Parsons, P.-C. Symons, Adsorption of sulphur-containing species at the mercury/water interphase, Trans Faraday Soc. 64 (1968) 1077–1092.
[157] H. Kasuk, G. Nurk, K. Lust, E. Lust, Adsorption kinetics of uracil on bismuth single crystal planes, J. Electroanal. Chem. 550–551 (2003) 13–31.

[158] J. Bukowska, K. Jackowska, Influence of thiourea on hydrogen evolution at a silver electrode as studied by electrochemical and SERS methods, J. Electroanal. Chem. 367 (1994) 41–48.
[159] L.E. Rybalka, B.B. Damaskin, Adsorption of thiourea at cadmium electrode, Elektrokhimiya. 9 (1973) 89.
[160] N.B. Grigorjev, D.M. Matšavariani, Adsorption of thiourea on lead, Elektrokhimiya. 6 (1970) 1062–1068.
[161] A. Lukomska, J. Sobkowski, Influence of the copper electrode structure on adsorption of thiourea in neutral solution, J. Electroanal. Chem. 592 (2006) 68–76.
[162] R. Parsons, The contribution to the capacity of an electrode from a species adsorbed with partial charge transfer, Can J Chem. 59 (1981) 1898–1902.
[163] A. Compte, Stochastic foundations of fractional dynamics, Phys. Rev. E. 53 (1996) 4191–4193.
[164] A. Compte, R. Metzler, The generalized Cattaneo equation for the description of anomalous transport processes, J. Phys. Math. Gen. 30 (1997) 7277.
[165] J. Bisquert, G. Garcia-Belmonte, P. Bueno, E. Longo, L.O.S. Bulhoes, Impedance of constant phase element (CPE)-blocked diffusion in film electrodes, J. Electroanal. Chem. 452 (1998) 229–234.
[166] J. Bisquert, A. Compte, Theory of the electrochemical impedance of anomalous diffusion, J. Electroanal. Chem. 499 (2001) 112–120.
[167] S. Kallip, H. Kasuk, V. Grozovski, P. Möller, E. Lust, Adsorption of camphor and 2,2′-bipyridine on Bi(111) electrode surface, Electrochimica Acta. 53 (2008) 4035–4045.
[168] A. Nilsson, L. Pettersson, J.K. Nørskov, Chemical bonding at surfaces and interfaces, Elsevier Amsterdam, 2008.
[169] W. Liu, V.G. Ruiz, G.-X. Zhang, B. Santra, X. Ren, M. Scheffler, et al., Structure and energetics of benzene adsorbed on transition-metal surfaces: density-functional theory with van der Waals interactions including collective substrate response, New J. Phys. 15 (2013) 053046.
[170] N. Marom, A. Tkatchenko, M. Rossi, V.V. Gobre, O. Hod, M. Scheffler, et al., Dispersion Interactions with Density-Functional Theory: Benchmarking Semiempirical and Interatomic Pairwise Corrected Density Functionals, J. Chem. Theory Comput. 7 (2011) 3944–3951.
[171] M. Sanchez Maestre, R. Rodriguez-Amaro, E. Munoz, J.J. Ruiz, L. Camacho, Formation of Two-Dimensional Phases of 4,4'-Bipyridine Cation Radical over Mercury in the Presence of Iodide Ions, Langmuir. 10 (1994) 723–729.
[172] M. Sánchez-Maestre, R. Rodríguez-Amaro, E. Muñoz, J.J. Ruiz, L. Camacho, Effects of temperature and anion type on the two-dimensional condensation of the 4,4′-bipyridine cation radical on mercury, J. Electroanal. Chem. 390 (1995) 21–27.
[173] M. Sánchez-Maestre, R. Rodríguez-Amaro, E. Muñoz, J.J. Ruiz, L. Camacho, The cyclic voltammetric behaviour of 4,4′-bipyridine over mercury in an acid medium, Electrochimica Acta. 41 (1996) 819–825.
[174] G.E. Thayer, J.T. Sadowski, F. Meyer zu Heringdorf, T. Sakurai, R.M. Tromp, Role of Surface Electronic Structure in Thin Film Molecular Ordering, Phys. Rev. Lett. 95 (2005) 256106.

[175] K.H.L. Zhang, H. Li, H. Mao, H. Huang, J. Ma, A.T.S. Wee, et al., Control of Two-Dimensional Ordering of F16CuPc on Bi/Ag(111): Effect of Interfacial Interactions, J. Phys. Chem. C. 114 (2010) 11234–11241.
[176] K.J.M. Bishop, C.E. Wilmer, S. Soh, B.A. Grzybowski, Nanoscale Forces and Their Uses in Self-Assembly, Small. 5 (2009) 1600–1630.

9. SUMMARY IN ESTONIAN

Orgaaniliste ühendite adsorptsiooni uurimine monokristalsetel elektroodidel in situ STM meetodiga

Käesoleva töö eesmärgiks oli uurida orgaaniliste ainete adsorptsiooni monokristalsel Bi(111) elektroodil, kasutades kõrglahutusvõimega *in situ* STM meetodit, impedantsspektroskoopiat ja tsüklilist voltamperomeetriat. Lisaks uuriti elektrokeemiliselt poleeritud ning vedela lämmastiku temperatuuril lõhestatud Sb(111) monokristalli pinnastruktuuri vesilahuses. Saadud tulemusi võrreldi Bi monokristalli andmetega [29]. Bi ja Sb elektroodid on rakendatavad nii elektroanalüüsis kui ka nanoklastrina kütuselementides.

Aatomlahutus saavutati nii lõhestatud $Sb(111)^{C}$ kui ka elektrokeemiliselt poleeritud $Sb(111)^{EP}$ monokristalli puhul. *In situ* STM andmetest selgub, et $Sb(111)^{C}$ ega ka $Sb(111)^{EP}$ monokristalse elektroodi pinnal ei toimu kiiret pinna rekonstruktsiooni ning pinnastruktuur on stabiilne uuritud suhteliselt laias potentsiaalivahemikus, mis on võrreldav tulemus Bi(111) monokristallil saadud andmetega [3,29,81].

Leiti, et keerulisemate kahedimensionaalsete kihtide uurimisel, mis tekivad erinevate orgaaniliste ühendite või ioonsete vedelike adsorptsioonil niinimetatud Hg-sarnastel, kõrge vesiniku ülepingega metallidel, saab lisaks $Bi(111)^{C}$ ja $Bi(111)^{EP}$ kasutada ka $Sb(111)^{C}$ ja $Sb(111)^{EP}$ monokristall elektroode [30,59,63,83,84,90].

Leiti atomaarselt siledad alad kõigil uuritud Sb(111) ja Bi(111) elektrokeemiliselt poleeritud pindadel sarnaselt lõhestatud Sb(111) ja Bi(111) pindadega. Seega näidati, et elektrokeemiline poleerimine on üsna universaalne pinna ettevalmistuse meetod, mida saab rakendada pinna töötlemiseks elektrilise kaksikkihi, adsorptsiooni jt elektrokeemia alaste uuringute puhul.

Tiokarbamiidi (TU) adsorptsiooni uurimisel Bi(111) pinnal analüüsiti elektroodi potentsiaali ja TU kontsentratsiooni mõju TU adsorptsiooni kineetikale. Leiti, et maksimaalse adsorptsiooni alas (E> –0,85 V) mõjutab TU adsorptsiooni summaarset kiirust Bi(111) elektroodi pinnale nii aeglase adsorptsiooni, osaline laenguülekande kui ka difusiooni staadiumi kiirus. *In situ* STM uuringud näitasid, et stabiilne adsorbaadi kiht tekib ainult nõrgalt positiivselt ja negatiivselt laetud Bi(111) elektroodi pinnal, kui toimub tugev TU spetsiifiline adsorptsioon. *In situ* STM andmed on heas kooskõlas elektrokeemilisi impedantsi andmetega, mis näitavad, et TU nõrk kemosorptsioon osalise laenguülekandega algab alles E> –0,85 V juures. TU on kasutatav reagent metallide elektrosadestamisel selleks, et saada nanoskaalas siledaid pindu.

TU adsorptsiooni lahjematest lahustest on võimalik modelleerida, kasutades modifitseeritud Frumkini ja Melik-Gaikazyani ekvivalentskeemi, milles klassikalise difusiooni mudel (difusiooni impedants, ehk difusiooniline takistus) on asendatud üldistatud difusioonilise impedantsiga, mis on õige piiratud paksusega adsorbaadikihi korral. Kõrgematel TU kontsentratsioonidel ja elektrood-

potentsiaalidel $E \geq -1{,}3$ V tuleb kasutada veelgi keerulisemaid matemaatilisi mudeleid (s.o ekvivalentskeeme), milles laenguülekande takistus on lisatud paralleelselt adsorptsioonilise mahtuvuse ja üldise massiülekande takistusega lõpliku paksusega adsorptsioonikihis. Kogutud andmed näitavad, et Bi(111) pindkihis toimub kaks paralleelset protsessi – seega samaaegselt toimuvad nii adsorptsioon osalise laenguülekandega kui ka „tõeline" faradi laenguülekande protsess.

Uuriti 4,4'-bipüridiini (4,4'-BP) adsorptsiooni Bi(111) monokristalli pinnal nõrgalt hapestatud naatriumsulfaadi foonelektrolüüdi lahusest. Visualiseeriti nanotasemel korrapäraselt adsorbeerunud 4,4'-BP struktuurid. Impedantsspektroskoopia andmetest leiti, et maksimaalse adsorptsiooni piirkonnas leidub vähemalt kolm mahtuvuse depressiooni piirkonda, st adsorptsiooni ala. Tsüklilise voltamperomeetria andmetest järeldati, et madalatel 4,4'-BP kontsentratsioonidel on adsorptsiooniprotsessid peaaegu pöörduvad. Elektroodiprotsessid kõrgematel 4,4'-BP kontsentratsioonidel on osaliselt pöördumatud, eriti anoodsetel potentsiaalidel, mis on tingitud 4,4'-BP redutseerimisest kahes etapis ning ioonsete komplekside $(4{,}4'\text{-}BPH_2^+)_n$ moodustumisest, mis omakorda moodustavad kompaktse adsorbtsioonilise ioonilise kihi vismut (111) elektroodi pinnal.

In situ STM andmete alusel leiti, et negatiivselt laetud Bi(111) pinnal moodustuvad adsorbeerunud 4,4'-BP molekulidest paralleelsed read. Tihedusfunktsionaali teooria (DFT) arvutused näitasid, et üksikud 4,4'-BP molekulid adsorbeeruvad eelistatult aromaatse tsükli tasandiga paralleelselt Bi(111) pinnaga. Juhul, kui Bi(111) pinnal on mitmeid adsorbeerunud 4,4'-BP molekule, siis tänu märgatavale van der Waalsi toimele molekulidest moodustunud ridade vahel ja molekulide vahelisele toimele ridade sees adsorbeeruvad 4,4'-BP molekulid oma aromaatse tsükli tasandiga risti pinnaga.

Teoreetiliselt modelleeritud ja eksperimentaalselt mõõdetud *in situ* STM andmeid võrreldi infrapuna spektroskoopia andmetega, mis kinnitas hüpoteesi, et 4,4'-BP molekulid adsorbeeruvad Bi(111) elektroodil pinnaga risti.

Adsorbeerunud 4,4'-BP molekulaarioonide kiled võivad olla tulevikus rakendatavad molekulaarmäludes ja välja-efektil põhinevates transistorides. Töö olulise tulemusena järeldati, et nanoskaalas tekivad hästi orienteeritud struktuurid monokristalsetel Bi(111) elektroodidel juhul, kui on hea sobivus molekulide omavahelise toime, pinna interaktsioonide ning adsorptsiooniposit-sioonide kauguse vahel. Antud töös näidati, et hästi orienteeritud struktuuride moodustumist, mis on sarnane 4,4'-BP adsorptsiooni kihi struktuuriga Bi(111) pinnal, on võimalik prognoosida DFT arvutuste abil juhul, kui van der Waalsi interaktsioonid on nõuetekohaselt kirjeldatud.

10. ACKNOWLEDGEMENTS

The present study was performed at the Institute of Chemistry of the University of Tartu and supported by the Estonian Science Foundation (grants 5803, 6696, 6970, 8786), the Estonian Centre of Excellence "High-Technology Materials For Sustainable Development" (Project TLOKT 117T), Estonian target research project SF0180002s08 and graduate school "Functional materials and technologies" receiving funding from the European Social Fund under project 1.2.0401.09-0079 in Estonia projects.

First of all I would like to express my thankfulness to my supervisors Professor Enn Lust and PhD Silvar Kallip for persistent assistance and thorough scientific guidance during these years of collaboration.

I want to give special thanks to PhD Vladislav Ivaništšev for inspiration and help with quantum chemical calculations, to PhD Heili Kasuk for introduction to impedance spectroscopy method and great help for analysis of data, to PhD Tavo Romann for his great help on infrared experiments and to PhD Karmen Lust for her enthusiastic encouragement and useful critiques and advices on my scientific writing.

I would like to thank all my colleagues, Erik Anderson, Piret Pikma, PhD Liis Siinor, PhD Eneli Härk and many others in the Institute of Chemistry for helpful discussions, inspiration and warm and friendly atmosphere during my working days.

I am very thankful to my parents for their support and patience during my studies. I am grateful to my friends in Tartu and Andrei Trufanov in Tallinn for their strong belief for the success of this work.

I express my kindest regards to Lilia, for her encouragement and support during writing of this Thesis, for her love and attention that helped me every day and in the most difficult moments.

CURRICULUM VITAE

Name:	Vitali Grozovski
Born:	May 19, 1983
Citizenship:	Estonian
Address:	University of Tartu, Institute of Chemistry, Ravila 14a, 50411 Tartu, Estonia
Phone:	+372 737 6627
E-mail:	vitali.grozovski@ut.ee

Education:

1990–2002	Mustamäe School of Humanities (Tallinn) – secondary education
2002–2005	University of Tartu – B.Sc. in chemistry
2005–2007	University of Tartu – M.Sc. in physical and electrochemistry (*cum laude*)
2007–present	University of Tartu, Institute of chemistry, PhD student (physical- and electrochemistry)

Professional experience:

09.2005–09.2007	University of Tartu, Institute of Physical Chemistry, chemist position
10.2007–09.2011	University of Alicante, Surface Electrochemistry Group, chemist position
10.2011– present	University of Tartu, Institute of Chemistry, chemist position

Major scientific publications:

1. E. Lust, J. Nerut, E. Härk, S. Kallip, **V. Grozovski**, T. Thomberg, R. Jäger, K. Jääger, K. Lust, K. Tähnas, Electroreduction of Complex Ions at Bismuth and Cadmium Single Crystal Plane Electrodes, Electrochem. Soc. Trans. 1, (17) 9 **(2006)**.
2. G. Nurk, R. Küngas, I. Kivi, H. Kurig, **V. Grozovski**, S. Kallip, E. Lust, Influence of Mesoporosity of the Anode on the Characteristics of Medium-temperature SOFC Single Cells, Electrochem. Soc. Trans. 7, (1) 1609 **(2007)**.
3. E. Lust, I. Kivi, G. Nurk, P. Möller, S. Kallip, **V. Grozovski**, H. Kurig, Influence of Cathode Porosity and Potential on Oxygen Reduction Kinetics at Intermediate Temperature SOFCs Cathodes, Electrochem. Soc. Trans. 7, (1) 1071 **(2007)**.
4. S. Kallip, H. Kasuk, **V. Grozovski**, Enn Lust, Adsorption of camphor at Bi(111) electrode, ECS Trans. 3, 155–168 **(2007)**.

5. T. Romann, **V. Grozovski**, E. Lust, Formation of the bismuth thiolate compound layer on bismuth surface, Electrochemistry Communications, Volume 9, Issue 10, Pages 2507–2513 **(2007)**.
6. R. Jäger, S. Kallip, **V. Grozovski**, K. Lust, E. Lust, Electroreduction of $S_2O_8^{-2}$ anions on chemically etched and electrochemically polished Bi(111) electrode, Journal of Electroanalytical Chemistry, Volume 622, Issue 1, Pages 79–89 **(2008)**.
7. S. Kallip, H. Kasuk, **V. Grozovski**, P. Möller, E. Lust, Adsorption of camphor and 2,2'-bipyridine on Bi(111) electrode surface, Electrochimica Acta, Volume 53, Issue 11, Pages 4035–4045 **(2008)**.
8. **V. Grozosvki**, V. Climent, E. Herrero, J.M. Feliu, Intrinsic Activity and Poisoning Rate for HCOOH Oxidation at Pt(100) and Vicinal Surfaces Containing Monoatomic (111) Steps, Chem. Phys. Chem, 10, 1992 **(2009)**.
9. **V. Grozosvki**, V. Climent, E. Herrero, J.M. Feliu, Intrinsic activity and poisoning rate for HCOOH oxidation on platinum stepped surfaces, Phys. Chem. Chem. Phys., 12, 31 **(2010)**.
10. **V. Grozosvki**, J. Solla-Gullón, V. Climent, E. Herrero, J.M. Feliu, Formic Acid Oxidation on Shape-Controlled Pt Nanoparticles Studied by Pulsed Voltammetry, J. Phys. Chem. C, 114, 32 **(2010)**.
11. **V. Grozovski**, F.J. Vidal-Iglesias, E. Herrero J.M. Feliu, Adsorption of Formate and Its Role as Intermediate in Formic Acid Oxidation on Platinum Electrodes, Chem.Phys.Chem., 12, 1641–644 **(2011)**.
12. **V. Grozovski**, V. Climent, E. Herrero, J.M. Feliu, The role of the surface structure in the oxidation mechanism of methanol, J. Electroanal. Chem., 662 (1), 43–51 **(2011)**.
13. **V. Grozovski**, S. Kallip E. Lust, In situ STM studies of Sb(111) electrodes in aqueous electrolyte solutions, Surf. Sci 613, 108–113 **(2013)**.
14. C. Busó-Rogero, **V. Grozovski**, F.J. Vidal-Iglecias, J. Sollá-Gullón, E. Herrero J.M. Feliu, Surface Structure and Anion Effects in the Oxidation of Ethanol on Platinum Nanoparticles, J. Mater. Chem. A 1, 7068–7076 **(2013)**.
15. V. Del Colle, **V. Grozovski**, E. Herrero, J.M. Feliu, Unusually High Activity of Pt Islands on Rh(111) Electrodes for Ethanol Oxidation, Chem. Cat. Chem. Comm. 5, 1350–1353 **(2013)**.
16. E. Anderson, **V. Grozovski**, L. Siinor, C. Siimenson, V. Ivaništšev, K. Lust, S. Kallip E. Lust, Influence of electrode potential and in situ STM scanning conditions on the phase boundary structure of single crystal Bi(111) | 1-butyl-4-methylpyridinium tetrafluoroborate interface, J. Electroanal. Chem. 709, 46–56 **(2013).**
17. **V. Grozovski**, H. Kasuk, S. Kallip, E. Lust, Adsorption of thiourea on Bi(111) electrode surface, J. of Electroanal. Chem. 712, 103–112 **(2014).**
18. **V. Grozovski**, V. Ivaništšev, H. Kasuk, T. Romann, E. Lust, Balance of the interfacial interactions of 4,4'-bipyridine at Bi(111) surface, Electrochim Act., *accepted* **(2013)**.

ELULOOKIRJELDUS

Nimi:	Vitali Grozovski
Sünniaeg:	19. mai 1983
Kodakondsus:	Eesti
Aadress:	Tartu Ülikool, Keemia Instituut, Ravila 14a, 50411 Tartu, Eesti
Telefon:	+372 737 6627
E-post:	vitali.grozovski@ut.ee

Haridus:

1990–2002	Tallinna Mustamäe Humanitaar Gümnaasium – põhiharidus
2002–2005	Tartu Ülikool – Bakalaureusekraad keemias
2005–2007	Tartu Ülikool – Magistrikraad keemias (*cum laude*)
2007–	Tartu Ülikool, Keemia Instituut, doktorant

Teenistuskäik:

09.2005–09.2007	Tartu Ülikool, Füüsikalise Keemia Instituut, keemik
10.2007–09.2011	Alicante Ülikool, Pinna Elektrokeemia Grupp, keemik
10.2011–	Tartu Ülikool, Keemia Instituut, keemik

Olulisemad publikatsioonid:

1. E. Lust, J. Nerut, E. Härk, S. Kallip, **V. Grozovski**, T. Thomberg, R. Jäger, K. Jääger, K. Lust, K. Tähnas, Electroreduction of Complex Ions at Bismuth and Cadmium Single Crystal Plane Electrodes, Electrochem. Soc. Trans. 1, (17) 9 **(2006)**.
2. G. Nurk, R. Küngas, I. Kivi, H. Kurig, **V. Grozovski**, S. Kallip, E. Lust, Influence of Mesoporosity of the Anode on the Characteristics of Medium-temperature SOFC Single Cells, Electrochem. Soc. Trans. 7, (1) 1609 **(2007)**.
3. E. Lust, I. Kivi, G. Nurk, P. Möller, S. Kallip, **V. Grozovski**, H. Kurig, Influence of Cathode Porosity and Potential on Oxygen Reduction Kinetics at Intermediate Temperature SOFCs Cathodes, Electrochem. Soc. Trans. 7, (1) 1071 **(2007)**.
4. S. Kallip, H. Kasuk, **V. Grozovski**, Enn Lust, Adsorption of camphor at Bi(111) electrode, ECS Trans. 3, 155–168 **(2007)**.
5. T. Romann, **V. Grozovski**, E. Lust, Formation of the bismuth thiolate compound layer on bismuth surface, Electrochemistry Communications, Volume 9, Issue 10, Pages 2507–2513 **(2007)**.
6. R. Jäger, S. Kallip, **V. Grozovski**, K. Lust, E. Lust, Electroreduction of $S_2O_8^{-2}$ anions on chemically etched and electrochemically polished Bi(111)

electrode, Journal of Electroanalytical Chemistry, Volume 622, Issue 1, Pages 79–89 **(2008)**.
7. S. Kallip, H. Kasuk, **V. Grozovski**, P. Möller, E. Lust, Adsorption of camphor and 2,2'-bipyridine on Bi(111) electrode surface, Electrochimica Acta, Volume 53, Issue 11, Pages 4035–4045 **(2008)**.
8. **V. Grozosvki**, V. Climent, E. Herrero, J.M. Feliu, Intrinsic Activity and Poisoning Rate for HCOOH Oxidation at Pt(100) and Vicinal Surfaces Containing Monoatomic (111) Steps, Chem. Phys. Chem, 10, 1992 **(2009)**.
9. **V. Grozosvki**, V. Climent, E. Herrero, J.M. Feliu, Intrinsic activity and poisoning rate for HCOOH oxidation on platinum stepped surfaces, Phys. Chem. Chem. Phys., 12, 31 **(2010)**.
10. **V. Grozosvki**, J. Solla-Gullón, V. Climent, E. Herrero, J.M. Feliu, Formic Acid Oxidation on Shape-Controlled Pt Nanoparticles Studied by Pulsed Voltammetry, J. Phys. Chem. C, 114, 32 **(2010)**.
11. **V. Grozovski**, F.J. Vidal-Iglesias, E. Herrero J.M. Feliu, Adsorption of Formate and Its Role as Intermediate in Formic Acid Oxidation on Platinum Electrodes, Chem.Phys.Chem., 12, 1641–644 **(2011)**.
12. **V. Grozovski**, V. Climent, E. Herrero, J.M. Feliu, The role of the surface structure in the oxidation mechanism of methanol, J. Electroanal. Chem., 662 (1), 43–51 **(2011)**.
13. **V. Grozovski**, S. Kallip E. Lust, In situ STM studies of Sb(111) electrodes in aqueous electrolyte solutions, Surf. Sci 613, 108–113 **(2013)**.
14. C. Busó-Rogero, **V. Grozovski**, F.J. Vidal-Iglecias, J. Sollá-Gullón, E. Herrero J.M. Feliu, Surface Structure and Anion Effects in the Oxidation of Ethanol on Platinum Nanoparticles, J. Mater. Chem. A 1, 7068–7076 **(2013)**.
15. V. Del Colle, **V. Grozovski**, E. Herrero, J.M. Feliu, Unusually High Activity of Pt Islands on Rh(111) Electrodes for Ethanol Oxidation, Chem. Cat. Chem. Comm. 5, 1350–1353 **(2013)**.
16. E. Anderson, **V. Grozovski**, L. Siinor, C. Siimenson, V. Ivaništšev, K. Lust, S. Kallip E. Lust, Influence of electrode potential and in situ STM scanning conditions on the phase boundary structure of single crystal Bi(111) | 1-butyl-4-methylpyridinium tetrafluoroborate interface, J. Electroanal. Chem. 709, 46–56 **(2013).**
17. **V. Grozovski**, H. Kasuk, S. Kallip, E. Lust, Adsorption of thiourea on Bi(111) electrode surface, J. of Electroanal. Chem. 712, 103–112 **(2014).**
18. **V. Grozovski**, V. Ivaništšev, H. Kasuk, T. Romann, E. Lust, Balance of the interfacial interactions of 4,4'-bipyridine at Bi(111) surface, Electrochim Act., *accepted* **(2013).**

DISSERTATIONES CHIMICAE UNIVERSITATIS TARTUENSIS

1. **Toomas Tamm.** Quantum-chemical simulation of solvent effects. Tartu, 1993, 110 p.
2. **Peeter Burk.** Theoretical study of gas-phase acid-base equilibria. Tartu, 1994, 96 p.
3. **Victor Lobanov.** Quantitative structure-property relationships in large descriptor spaces. Tartu, 1995, 135 p.
4. **Vahur Mäemets.** The ^{17}O and ^{1}H nuclear magnetic resonance study of H_2O in individual solvents and its charged clusters in aqueous solutions of electrolytes. Tartu, 1997, 140 p.
5. **Andrus Metsala.** Microcanonical rate constant in nonequilibrium distribution of vibrational energy and in restricted intramolecular vibrational energy redistribution on the basis of slater's theory of unimolecular reactions. Tartu, 1997, 150 p.
6. **Uko Maran.** Quantum-mechanical study of potential energy surfaces in different environments. Tartu, 1997, 137 p.
7. **Alar Jänes.** Adsorption of organic compounds on antimony, bismuth and cadmium electrodes. Tartu, 1998, 219 p.
8. **Kaido Tammeveski.** Oxygen electroreduction on thin platinum films and the electrochemical detection of superoxide anion. Tartu, 1998, 139 p.
9. **Ivo Leito.** Studies of Brønsted acid-base equilibria in water and non-aqueous media. Tartu, 1998, 101 p.
10. **Jaan Leis.** Conformational dynamics and equilibria in amides. Tartu, 1998, 131 p.
11. **Toonika Rinken.** The modelling of amperometric biosensors based on oxidoreductases. Tartu, 2000, 108 p.
12. **Dmitri Panov.** Partially solvated Grignard reagents. Tartu, 2000, 64 p.
13. **Kaja Orupõld.** Treatment and analysis of phenolic wastewater with microorganisms. Tartu, 2000, 123 p.
14. **Jüri Ivask.** Ion Chromatographic determination of major anions and cations in polar ice core. Tartu, 2000, 85 p.
15. **Lauri Vares.** Stereoselective Synthesis of Tetrahydrofuran and Tetrahydropyran Derivatives by Use of Asymmetric Horner-Wadsworth-Emmons and Ring Closure Reactions. Tartu, 2000, 184 p.
16. **Martin Lepiku.** Kinetic aspects of dopamine D_2 receptor interactions with specific ligands. Tartu, 2000, 81 p.
17. **Katrin Sak.** Some aspects of ligand specificity of P2Y receptors. Tartu, 2000, 106 p.
18. **Vello Pällin.** The role of solvation in the formation of iotsitch complexes. Tartu, 2001, 95 p.

19. **Katrin Kollist.** Interactions between polycyclic aromatic compounds and humic substances. Tartu, 2001, 93 p.
20. **Ivar Koppel.** Quantum chemical study of acidity of strong and superstrong Brønsted acids. Tartu, 2001, 104 p.
21. **Viljar Pihl.** The study of the substituent and solvent effects on the acidity of OH and CH acids. Tartu, 2001, 132 p.
22. **Natalia Palm.** Specification of the minimum, sufficient and significant set of descriptors for general description of solvent effects. Tartu, 2001, 134 p.
23. **Sulev Sild.** QSPR/QSAR approaches for complex molecular systems. Tartu, 2001, 134 p.
24. **Ruslan Petrukhin.** Industrial applications of the quantitative structure-property relationships. Tartu, 2001, 162 p.
25. **Boris V. Rogovoy.** Synthesis of (benzotriazolyl)carboximidamides and their application in relations with *N*- and *S*-nucleophyles. Tartu, 2002, 84 p.
26. **Koit Herodes.** Solvent effects on UV-vis absorption spectra of some solvatochromic substances in binary solvent mixtures: the preferential solvation model. Tartu, 2002, 102 p.
27. **Anti Perkson.** Synthesis and characterisation of nanostructured carbon. Tartu, 2002, 152 p.
28. **Ivari Kaljurand.** Self-consistent acidity scales of neutral and cationic Brønsted acids in acetonitrile and tetrahydrofuran. Tartu, 2003, 108 p.
29. **Karmen Lust.** Adsorption of anions on bismuth single crystal electrodes. Tartu, 2003, 128 p.
30. **Mare Piirsalu.** Substituent, temperature and solvent effects on the alkaline hydrolysis of substituted phenyl and alkyl esters of benzoic acid. Tartu, 2003, 156 p.
31. **Meeri Sassian.** Reactions of partially solvated Grignard reagents. Tartu, 2003, 78 p.
32. **Tarmo Tamm.** Quantum chemical modelling of polypyrrole. Tartu, 2003. 100 p.
33. **Erik Teinemaa.** The environmental fate of the particulate matter and organic pollutants from an oil shale power plant. Tartu, 2003. 102 p.
34. **Jaana Tammiku-Taul.** Quantum chemical study of the properties of Grignard reagents. Tartu, 2003. 120 p.
35. **Andre Lomaka.** Biomedical applications of predictive computational chemistry. Tartu, 2003. 132 p.
36. **Kostyantyn Kirichenko.** Benzotriazole – Mediated Carbon–Carbon Bond Formation. Tartu, 2003. 132 p.
37. **Gunnar Nurk.** Adsorption kinetics of some organic compounds on bismuth single crystal electrodes. Tartu, 2003, 170 p.
38. **Mati Arulepp.** Electrochemical characteristics of porous carbon materials and electrical double layer capacitors. Tartu, 2003, 196 p.

39. **Dan Cornel Fara.** QSPR modeling of complexation and distribution of organic compounds. Tartu, 2004, 126 p.
40. **Riina Mahlapuu.** Signalling of galanin and amyloid precursor protein through adenylate cyclase. Tartu, 2004, 124 p.
41. **Mihkel Kerikmäe.** Some luminescent materials for dosimetric applications and physical research. Tartu, 2004, 143 p.
42. **Jaanus Kruusma.** Determination of some important trace metal ions in human blood. Tartu, 2004, 115 p.
43. **Urmas Johanson.** Investigations of the electrochemical properties of polypyrrole modified electrodes. Tartu, 2004, 91 p.
44. **Kaido Sillar.** Computational study of the acid sites in zeolite ZSM-5. Tartu, 2004, 80 p.
45. **Aldo Oras.** Kinetic aspects of dATPαS interaction with $P2Y_1$ receptor. Tartu, 2004, 75 p.
46. **Erik Mölder.** Measurement of the oxygen mass transfer through the air-water interface. Tartu, 2005, 73 p.
47. **Thomas Thomberg.** The kinetics of electroreduction of peroxodisulfate anion on cadmium (0001) single crystal electrode. Tartu, 2005, 95 p.
48. **Olavi Loog.** Aspects of condensations of carbonyl compounds and their imine analogues. Tartu, 2005, 83 p.
49. **Siim Salmar.** Effect of ultrasound on ester hydrolysis in aqueous ethanol. Tartu, 2006, 73 p.
50. **Ain Uustare.** Modulation of signal transduction of heptahelical receptors by other receptors and G proteins. Tartu, 2006, 121 p.
51. **Sergei Yurchenko.** Determination of some carcinogenic contaminants in food. Tartu, 2006, 143 p.
52. **Kaido Tämm.** QSPR modeling of some properties of organic compounds. Tartu, 2006, 67 p.
53. **Olga Tšubrik.** New methods in the synthesis of multisubstituted hydrazines. Tartu. 2006, 183 p.
54. **Lilli Sooväli.** Spectrophotometric measurements and their uncertainty in chemical analysis and dissociation constant measurements. Tartu, 2006, 125 p.
55. **Eve Koort.** Uncertainty estimation of potentiometrically measured ph and pK_a values. Tartu, 2006, 139 p.
56. **Sergei Kopanchuk.** Regulation of ligand binding to melanocortin receptor subtypes. Tartu, 2006, 119 p.
57. **Silvar Kallip.** Surface structure of some bismuth and antimony single crystal electrodes. Tartu, 2006, 107 p.
58. **Kristjan Saal.** Surface silanization and its application in biomolecule coupling. Tartu, 2006, 77 p.
59. **Tanel Tätte.** High viscosity $Sn(OBu)_4$ oligomeric concentrates and their applications in technology. Tartu, 2006, 91 p.

60. **Dimitar Atanasov Dobchev**. Robust QSAR methods for the prediction of properties from molecular structure. Tartu, 2006, 118 p.
61. **Hannes Hagu**. Impact of ultrasound on hydrophobic interactions in solutions. Tartu, 2007, 81 p.
62. **Rutha Jäger.** Electroreduction of peroxodisulfate anion on bismuth electrodes. Tartu, 2007, 142 p.
63. **Kaido Viht.** Immobilizable bisubstrate-analogue inhibitors of basophilic protein kinases: development and application in biosensors. Tartu, 2007, 88 p.
64. **Eva-Ingrid Rõõm.** Acid-base equilibria in nonpolar media. Tartu, 2007, 156 p.
65. **Sven Tamp.** DFT study of the cesium cation containing complexes relevant to the cesium cation binding by the humic acids. Tartu, 2007, 102 p.
66. **Jaak Nerut.** Electroreduction of hexacyanoferrate(III) anion on Cadmium (0001) single crystal electrode. Tartu, 2007, 180 p.
67. **Lauri Jalukse.** Measurement uncertainty estimation in amperometric dissolved oxygen concentration measurement. Tartu, 2007, 112 p.
68. **Aime Lust.** Charge state of dopants and ordered clusters formation in CaF_2:Mn and CaF_2:Eu luminophors. Tartu, 2007, 100 p.
69. **Iiris Kahn**. Quantitative Structure-Activity Relationships of environmentally relevant properties. Tartu, 2007, 98 p.
70. **Mari Reinik.** Nitrates, nitrites, N-nitrosamines and polycyclic aromatic hydrocarbons in food: analytical methods, occurrence and dietary intake. Tartu, 2007, 172 p.
71. **Heili Kasuk.** Thermodynamic parameters and adsorption kinetics of organic compounds forming the compact adsorption layer at Bi single crystal electrodes. Tartu, 2007, 212 p.
72. **Erki Enkvist.** Synthesis of adenosine-peptide conjugates for biological applications. Tartu, 2007, 114 p.
73. **Svetoslav Hristov Slavov**. Biomedical applications of the QSAR approach. Tartu, 2007, 146 p.
74. **Eneli Härk.** Electroreduction of complex cations on electrochemically polished Bi(*hkl*) single crystal electrodes. Tartu, 2008, 158 p.
75. **Priit Möller.** Electrochemical characteristics of some cathodes for medium temperature solid oxide fuel cells, synthesized by solid state reaction technique. Tartu, 2008, 90 p.
76. **Signe Viggor.** Impact of biochemical parameters of genetically different pseudomonads at the degradation of phenolic compounds. Tartu, 2008, 122 p.
77. **Ave Sarapuu.** Electrochemical reduction of oxygen on quinone-modified carbon electrodes and on thin films of platinum and gold. Tartu, 2008, 134 p.
78. **Agnes Kütt.** Studies of acid-base equilibria in non-aqueous media. Tartu, 2008, 198 p.

79. **Rouvim Kadis.** Evaluation of measurement uncertainty in analytical chemistry: related concepts and some points of misinterpretation. Tartu, 2008, 118 p.
80. **Valter Reedo.** Elaboration of IVB group metal oxide structures and their possible applications. Tartu, 2008, 98 p.
81. **Aleksei Kuznetsov.** Allosteric effects in reactions catalyzed by the cAMP-dependent protein kinase catalytic subunit. Tartu, 2009, 133 p.
82. **Aleksei Bredihhin.** Use of mono- and polyanions in the synthesis of multisubstituted hydrazine derivatives. Tartu, 2009, 105 p.
83. **Anu Ploom.** Quantitative structure-reactivity analysis in organosilicon chemistry. Tartu, 2009, 99 p.
84. **Argo Vonk.** Determination of adenosine A_{2A}- and dopamine D_1 receptor-specific modulation of adenylate cyclase activity in rat striatum. Tartu, 2009, 129 p.
85. **Indrek Kivi.** Synthesis and electrochemical characterization of porous cathode materials for intermediate temperature solid oxide fuel cells. Tartu, 2009, 177 p.
86. **Jaanus Eskusson.** Synthesis and characterisation of diamond-like carbon thin films prepared by pulsed laser deposition method. Tartu, 2009, 117 p.
87. **Marko Lätt.** Carbide derived microporous carbon and electrical double layer capacitors. Tartu, 2009, 107 p.
88. **Vladimir Stepanov.** Slow conformational changes in dopamine transporter interaction with its ligands. Tartu, 2009, 103 p.
89. **Aleksander Trummal.** Computational Study of Structural and Solvent Effects on Acidities of Some Brønsted Acids. Tartu, 2009, 103 p.
90. **Eerold Vellemäe.** Applications of mischmetal in organic synthesis. Tartu, 2009, 93 p.
91. **Sven Parkel.** Ligand binding to 5-HT_{1A} receptors and its regulation by Mg^{2+} and Mn^{2+}. Tartu, 2010, 99 p.
92. **Signe Vahur.** Expanding the possibilities of ATR-FT-IR spectroscopy in determination of inorganic pigments. Tartu, 2010, 184 p.
93. **Tavo Romann**. Preparation and surface modification of bismuth thin film, porous, and microelectrodes. Tartu, 2010, 155 p.
94. **Nadežda Aleksejeva.** Electrocatalytic reduction of oxygen on carbon nanotube-based nanocomposite materials. Tartu, 2010, 147 p.
95. **Marko Kullapere.** Electrochemical properties of glassy carbon, nickel and gold electrodes modified with aryl groups. Tartu, 2010, 233 p.
96. **Liis Siinor.** Adsorption kinetics of ions at Bi single crystal planes from aqueous electrolyte solutions and room-temperature ionic liquids. Tartu, 2010, 101 p.
97. **Angela Vaasa.** Development of fluorescence-based kinetic and binding assays for characterization of protein kinases and their inhibitors. Tartu 2010, 101 p.

98. **Indrek Tulp.** Multivariate analysis of chemical and biological properties. Tartu 2010, 105 p.
99. **Aare Selberg.** Evaluation of environmental quality in Northern Estonia by the analysis of leachate. Tartu 2010, 117 p.
100. **Darja Lavõgina.** Development of protein kinase inhibitors based on adenosine analogue-oligoarginine conjugates. Tartu 2010, 248 p.
101. **Laura Herm.** Biochemistry of dopamine D_2 receptors and its association with motivated behaviour. Tartu 2010, 156 p.
102. **Terje Raudsepp.** Influence of dopant anions on the electrochemical properties of polypyrrole films. Tartu 2010, 112 p.
103. **Margus Marandi.** Electroformation of Polypyrrole Films: *In-situ* AFM and STM Study. Tartu 2011, 116 p.
104. **Kairi Kivirand.** Diamine oxidase-based biosensors: construction and working principles. Tartu, 2011, 140 p.
105. **Anneli Kruve.** Matrix effects in liquid-chromatography electrospray mass-spectrometry. Tartu, 2011, 156 p.
106. **Gary Urb.** Assessment of environmental impact of oil shale fly ash from PF and CFB combustion. Tartu, 2011, 108 p.
107. **Nikita Oskolkov.** A novel strategy for peptide-mediated cellular delivery and induction of endosomal escape. Tartu, 2011, 106 p.
108. **Dana Martin.** The QSPR/QSAR approach for the prediction of properties of fullerene derivatives. Tartu, 2011, 98 p.
109. **Säde Viirlaid.** Novel glutathione analogues and their antioxidant activity. Tartu, 2011, 106 p.
110. **Ülis Sõukand.** Simultaneous adsorption of Cd^{2+}, Ni^{2+}, and Pb^{2+} on peat. Tartu, 2011, 124 p.
111. **Lauri Lipping.** The acidity of strong and superstrong Brønsted acids, an outreach for the "limits of growth": a quantum chemical study. Tartu, 2011, 124 p.
112. **Heisi Kurig.** Electrical double-layer capacitors based on ionic liquids as electrolytes. Tartu, 2011, 146 p.
113. **Marje Kasari.** Bisubstrate luminescent probes, optical sensors and affinity adsorbents for measurement of active protein kinases in biological samples. Tartu, 2012, 126 p.
114. **Kalev Takkis.** Virtual screening of chemical databases for bioactive molecules. Tartu, 2012, 122 p.
115. **Ksenija Kisseljova**. Synthesis of aza-β^3-amino acid containing peptides and kinetic study of their phosphorylation by protein kinase A. Tartu, 2012, 104 p.
116. **Riin Rebane.** Advanced method development strategy for derivatization LC/ESI/MS. Tartu, 2012, 184 p.

117. **Vladislav Ivaništšev.** Double layer structure and adsorption kinetics of ions at metal electrodes in room temperature ionic liquids. Tartu, 2012, 128 p.
118. **Irja Helm.** High accuracy gravimetric Winkler method for determination of dissolved oxygen. Tartu, 2012, 139 p.
119. **Karin Kipper.** Fluoroalcohols as Components of LC-ESI-MS Eluents: Usage and Applications. Tartu, 2012, 164 p.
120. **Arno Ratas.** Energy storage and transfer in dosimetric luminescent materials. Tartu, 2012, 163 p.
121. **Reet Reinart-Okugbeni**. Assay systems for characterisation of subtype-selective binding and functional activity of ligands on dopamine receptors. Tartu, 2012, 159 p.
122. **Lauri Sikk.** Computational study of the Sonogashira cross-coupling reaction. Tartu, 2012, 81 p.
123. **Karita Raudkivi.** Neurochemical studies on inter-individual differences in affect-related behaviour of the laboratory rat. Tartu, 2012, 161 p.
124. **Indrek Saar.** Design of GalR2 subtype specific ligands: their role in depression-like behavior and feeding regulation. Tartu, 2013, 126 p.
125. **Ann Laheäär.** Electrochemical characterization of alkali metal salt based non-aqueous electrolytes for supercapacitors. Tartu, 2013, 127 p.
126. **Kerli Tõnurist.** Influence of electrospun separator materials properties on electrochemical performance of electrical double-layer capacitors. Tartu, 2013, 147 p.
127. **Kaija Põhako-Esko.** Novel organic and inorganic ionogels: preparation and characterization. Tartu, 2013, 124 p.
128. **Ivar Kruusenberg.** Electroreduction of oxygen on carbon nanomaterial-based catalysts. Tartu, 2013, 191 p.
129. **Sander Piiskop.** Kinetic effects of ultrasound in aqueous acetonitrile solutions. Tartu, 2013, 95 p.
130. **Ilona Faustova**. Regulatory role of L-type pyruvate kinase N-terminal domain. Tartu, 2013, 109 p.
131. **Kadi Tamm.** Synthesis and characterization of the micro-mesoporous anode materials and testing of the medium temperature solid oxide fuel cell single cells. Tartu, 2013, 138 p.
132. **Iva Bozhidarova Stoyanova-Slavova.** Validation of QSAR/QSPR for regulatory purposes. Tartu, 2013, 109 p.